HIGH PRECISION GASEOUS PIXEL DETECTORS

MARIA TSAGRI

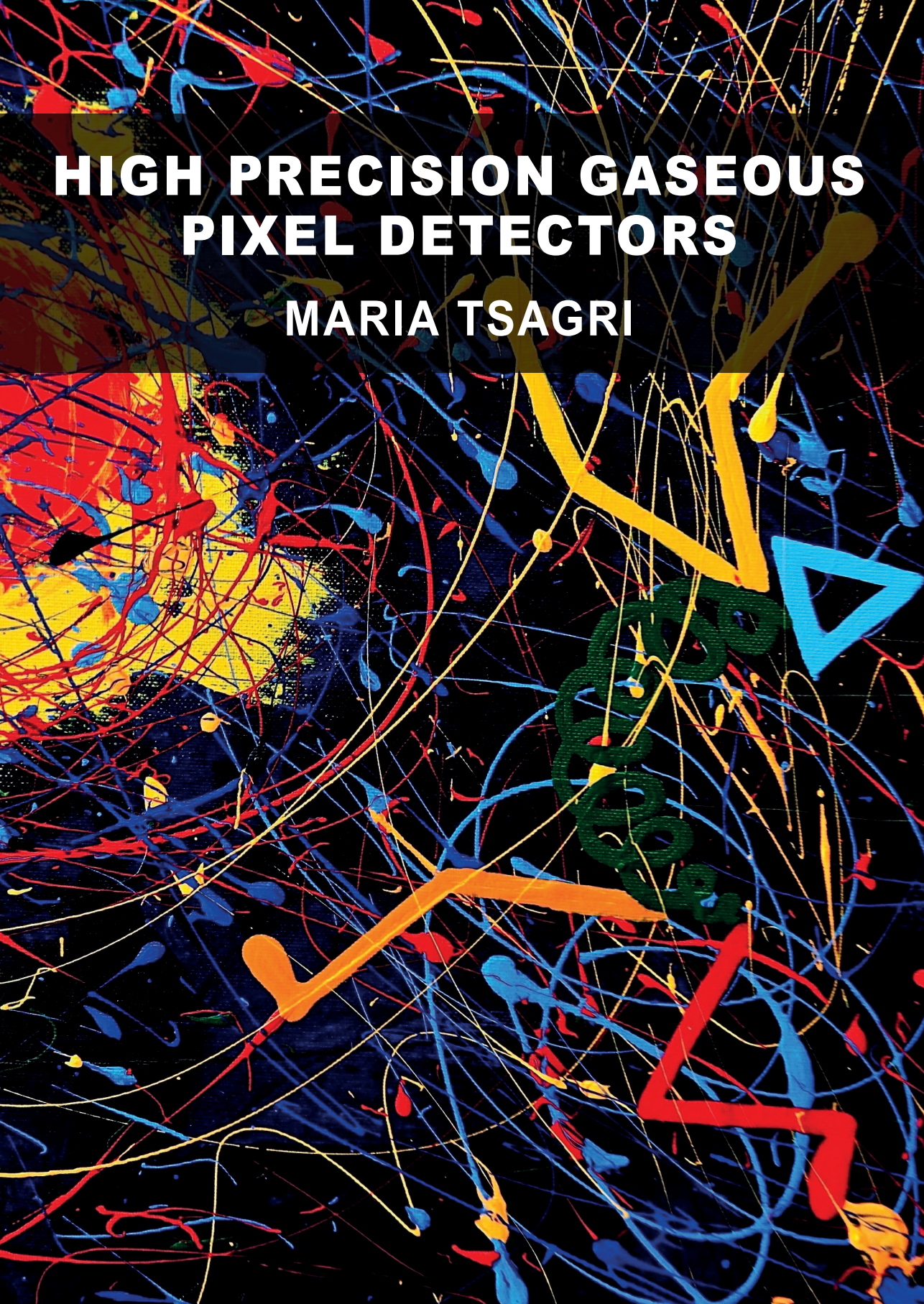

High Precision Gaseous Pixel Detectors

Maria Tsagri

Printed by: ProefschriftMaken || www.proefschriftmaken.nl

Typeset by LaTeX.

High Precision Gaseous Pixel Detectors

ACADEMISCH PROEFSCHRIFT

ter verkrijging van de graad van doctor
aan de Universiteit van Amsterdam
op gezag van de Rector Magnificus
prof. dr. ir. K.I.J. Maex
ten overstaan van een door het College van Promoties ingestelde
commissie, in het openbaar te verdedigen in de Agnietenkapel
op dinsdag 15 mei 2018, te 12:00 uur

door

Maria Tsagri

geboren te Athene, Griekenland

Promotiecommissie:

Promotores:	Prof. dr. S.C.M. Bentvelsen	Universiteit van Amsterdam
	Prof. dr. ir. E.N. Koffeman	Universiteit van Amsterdam
Copromotor:	Dr. N.P. Hessey	TRIUMF Canada
Overige Leden:	Prof. dr. S.J. de Jong	Radboud Universiteit Nijmegen
	Prof. dr. P.M. Kooijman	Universiteit van Amsterdam
	Prof. dr. ir. P.J. de Jong	Universiteit van Amsterdam
	Prof. dr. F.L. Linde	Universiteit van Amsterdam
	Prof. dr. ir. H. van der Graaf	TU Delft
	Prof. dr. A. Pellegrino	Rijksuniversiteit Groningen

Faculteit der Natuurwetenschappen, Wiskunde en Informatica

NWO
Netherlands Organisation
for Scientific Research

This work was supported by the Marie Curie Particle Detector (MC-PAD) Initial Training Network (ITN) which is part of the European Union's Research and Innovation funding program FP7, CERN and the Foundation for Fundamental Research on Matter (FOM), which is part of the Netherlands Organisation for Scientific Research (NWO). It was carried out at the CERN in Switzerland and the National Institute for Subatomic Physics (Nikhef) in the Netherlands.

CONTENTS

CHAPTER 1

INTRODUCTION

Outlook of this thesis

The scope of this thesis is the study and development of gaseous detectors such as the Gossip detector as well as their applications in High Energy Physics (HEP). The thesis is structured as follows:

Chapter 1 provides an overview of the well known Standard Model and an outlook to the physics beyond the Standard Model. In addition, it presents current highlights of the Large Hadron Collider as well as future updates including an introduction to the future International Linear Collider concept.

Chapter 2 introduces the operation principles of gaseous detectors focusing on the production and transport process of ion-electron couples. In addition, we present simulation studies performed for various gas mixtures used in micro pattern gaseous detectors.

Chapter 3 presents a detailed simulation analysis of the energy loss inside a thin gaseous detector. The analysis performed in this Chapter helped to improve the accuracy of simulation tools widely used in HEP experiments.

Chapter 4 introduces simulation of the neutron in the Geant4 tool. It shows the results of an extensive analysis on neutron cross-sections where it was found that the update of the tool was necessary. Results of the updated tool are also presented here.

Chapter 5 shows experimental measurements of the electron transmission taken with a Micromegas.

Chapter 6 introduces the Gossip detector and describes its principle of operation as well as its technical specifications. We also present experimental measurements that aim to

support the development and amelioration of the detector.

1.1 The Standard Model

The Standard Model (SM) is a quantum field theory which collectively describes the electromagnetic, weak and strong interactions between quarks and leptons. It is based on the fundamental notion of gauge symmetries, i.e. symmetries which hold at every space-time point. The gauge symmetry of the SM Lagrangian corresponds to the group $SU(3) \times SU(2)_L \times U(1)_Y$, where L denotes the fact that the symmetry applies to left-handed fields and Y denotes the weak hypercharge. The three symmetries are related to transformations that change the color, weak isospin and weak hypercharge of the fundamental fields and also imply the conservation of the corresponding quantities.

The SM Lagrangian also exhibits a global Poincaré symmetry, associated to the conservation of energy, momentum and angular momentum as well as a series of global symmetries, such as the ones associated to the conservation of lepton and baryon number, which arise from the requirement of renormalizability. The strong sector of the SM corresponds to the $SU(3)$ symmetry, which governs the color interactions between quarks and antiquarks. The color degree of freedom was first introduced to allow for the existence of resonances with anti-symmetric wave functions, comprised of three quarks of identical flavor and spin, such as the Δ^{++}. The $SU(3)$ symmetry predicts the existence of 8 massless gluons, which carry color and anticolor and mediate the color interactions between quarks and antiquarks. Since this is an exact symmetry of the Lagrangian it would imply the presence of degenerate colored multiplets. These are however not observed, due to the phenomenon of color confinement, the precise details of which are a subject of ongoing research in heavy ion experiments.

The electroweak sector of the SM corresponds to the $SU(2)_L \times U(1)_Y$ group and is also associated to a phase transition which spontaneously breaks the symmetry group to $U(1)_Q$, which is the symmetry group of electromagnetism. According to the mechanism of spontaneous symmetry breaking, which was introduced by Higgs, Brout, Englert, Guralnik, Hagen and Kibble [1] - [5], at high energies the Lagrangian is invariant under the full $SU(2)_L \times U(1)_Y$ symmetry which predicts the existence of 4 massless gauge bosons, and a scalar field, the Higgs field, which plays the role of the order parameter.

The last ingredient of the SM is its particle content. The fermion fields (quarks and leptons) are introduced by hand and correspond to multiplets that transform under different representations of the SM gauge group. While the SM has been very successful in describing the observed phenomena in high energy physics experiments, we know that the model is not complete. The SM as it stands today only describes the regular matter that makes up only 4% of the Universe whereas we already know that dark matter exists accounting for about 26% of the matter in the Universe. The rest $\sim$70%, the so-called "dark energy", is known to us only through the way it contributes to the accelerated expansion of the Universe. Moreover, the theory cannot explain the smallness of the Higgs mass (which should be driven to very high scales by quantum corrections), nor

does it provide candidates for the explanation of dark matter and dark energy. The strong CP problem in the strong sector is another celebrated example, whose solution in terms of the Peccei-Quinn axion could provide a candidate for the explanation of dark matter [8].

These unanswered questions constitute the driving forces behind the design of the LHC as well as of other non-collider experiments at CERN and worldwide.

1.2 The Large Hadron Collider

The Large Hadron Collider (LHC) is a synchrotron-type accelerator designed to accelerate protons up to a center of mass energy $\sqrt{s} = 14$ TeV and lead ions up to a center of mass energy $\sqrt{s} = 2.76$ TeV per nucleon pair. It consists of two concentric rings 26.7 km in circumference which contain accelerating radiofrequency (RF) cavities as well as magnets which bend and focus the proton beams. The rings intersect at four points where the four main LHC experiments are installed: ATLAS, CMS, ALICE and LHCb.

Each beam contains a maximum of 2808 proton bunches, each of which contains up to $1.15 \cdot 10^{11}$ protons. The beams collide with a rate of 40 MHz with a designed instantaneous luminosity of 10^{34} cm^{-2}s^{-1}. During the 2016 operation of the LHC the peak instantaneous luminosity has surpassed the design luminosity by 37%.

From the beginning of 2010 the LHC beam energy has increased from 2.36 TeV (2010) to 7 TeV (2011), 8 TeV (2012) and finally to 13 TeV (2015) after the first long shutdown for consolidation work. The gradual increase in the collision energy is required in order to train the superconducting magnets to withstand the high current but was also used for physics measurements, such as measuring the energy dependence of the underlying event, which is a critical aspect in Monte Carlo simulations.

The proton acceleration sequence proceeds in many steps, starting from the extraction of protons from hydrogen gas and their acceleration up to 50 MeV by a linear accelerator. A sequence of circular synchrotrons follows, increasing the proton energy gradually to 1.4 GeV (Proton Booster), 26 GeV (Proton Synchrotron) and 450 GeV (Super Proton Synchrotron). The final step is the insertion of the bunched 450 GeV beams into the LHC, which takes about 20 minutes to accelerate the beams to the final collision energies. The beams are circulated for a period which can range from a few hours to up to one day and are then dumped on a 8m-long graphite block.

1.2.1 The LHC experiments and highlights of their physics program

The LHC houses four large experiments: ATLAS, CMS, ALICE and LHCb, together with more specialized experiments: TOTEM, MoEDAL and LHCf.

ATLAS and CMS are general-purpose detectors designed to detect a wide range of physics signals. Both experiments were optimized for the detection of the Higgs boson, which is the main focus of their physics program. Both detectors feature an almost 4π coverage in solid angle, with large enough calorimeters that can fully contain the

very energetic decay products that arise from the decay of heavy resonances that are predicted in theories beyond the SM (BSM) and also to fully reconstruct the missing energy.

The ALICE experiment is designed to shed light into the non-perturbative aspects of QCD, particularly the formation of quark-gluon plasma (QGP). The ALICE detector uses data from lead-lead and proton-lead collisions. LHCb is a dedicated heavy flavor physics experiment, designed to study new physics in CP violation and rare decays of c and b-hadrons. Unlike ATLAS and CMS the LHCb detector is highly asymmetric, covering only the forward region.

LHCf is a detector installed close to ATLAS, which used zero degree calorimeters to detect particles produced in the very forward direction ($\eta > 8.4$), with the aim of collecting data to be used in the calibration of Monte Carlo models used in the study of very high energy cosmic ray experiments. TOTEM is a detector located close to CMS and its aim is to measure the diffractive, elastic and total proton-proton cross-section. Finally the MoEDAL experiment, which is located inside the LHCb experiment, is designed to search for highly ionizing particles, in particular for magnetic monopoles.
The main highlights of the physics program of the LHC experiments are discussed below.

Higgs
After the discovery of a Higgs-like boson by the ATLAS and CMS experiments [6, 7], the attention has turned to the measurement of its properties. ATLAS and CMS have measured the couplings of the Higgs boson to the electroweak gauge bosons and the Yukawa coupling to the SM fermions in the WW, ZZ, $\gamma\gamma$, bb, $\tau\tau$ and $\mu\mu$ final states [9]. The Higgs spin and parity have also been measured in the ZZ, WW and $\gamma\gamma$ channels excluding the non-SM hypotheses [10]. The Higgs mass has been determined with a precision of $\tilde{0}.2\%$, combining the ATLAS and CMS mass measurements in the $\gamma\gamma$ and $h \to 4l$ decay modes.

QCD
With an uncertainty of $\sim$5%, the strong coupling constant remains an important source of systematic precisely measured fundamental constant in the SM. Perturbation theory in α_s is source of the dominant systematic uncertainties in many theoretical predictions used in the LHC, such as the top-pair production cross-section, the $h \to b\bar{b}$ decay and others. While α_s was well constrained by previous experiments at low and intermediate momentum transfers, the LHC allowed to measure α_s up to around 2 TeV [11]. On top of indirectly improving the precision of theoretical predictions, these measurements were also of direct use in establishing constraints on new colored resonances that would modify the running of α_s [11].

SUSY Exclusion limits
ATLAS and CMS have performed both general and model-dependent searches for the production of supersymmetric particles pushing the exclusion limits for squark and gluino masses to more than 1 TeV in several models [13]. Both ATLAS and CMS results challenge future direct searches with underground dark matter experiments.

Other exotic searches
Exclusion limits have been set by ATLAS and CMS on the production of BSM resonances, such as W', Z', black holes, heavy scalars, as well as 4^{th} generation quarks, leptoquarks, dark matter, short range forces, etc. [14].

SM
Several processes within the SM have been measured with unparalleled precision, like the top-pair cross-section (6 % uncertainty), the inclusive Z, W and jet cross-section etc. ATLAS and CMS have also performed the most precise measurements of the W mass (0.03 % precision) and the top quark mass ($\sim$1 % precision) [16].

Non-perturbative QCD
Jet quenching and collective phenomena: The heavy ion CERN experiment ALICE has observed the phenomenon of jet quenching, i.e., the energy loss of a jet due to its interaction with a medium like quark-gluon plasma, in both Pb-Pb and p-Pb collisions [17]. A surprise was that the measurements of the elliptic flow of charged particles indicated the presence of collective phenomena, stronger than what was predicted by the hydrodynamical calculations. Related to the charmonium suppression, ALICE has observed a suppression of the formation of J/ψ, which is predicted to be a signature of the formation of quark gluon plasma.

Flavor physics
$B_s^0 \to \mu^+ \mu^-$, $B^0 \to K^{*0}$ ($\to K^+ \pi^-$) $\mu^+ \mu^-$ and Tetraquarks, pentaquarks: The other CERN experiment, LHCb, has observed a 4 σ deviation in the decay of B_s to 2 muons and an anomaly of the angular distribution in the decay of K^{*0} to $K^+ \pi^- \mu\mu$ corresponding to 3.7 σ [18]. These could provide hints for the presence of BSM resonances in the loop diagrams that describe the decays. LHCb has confirmed the existence of several resonances identified with tetraquark states and has discovered the first pentaquark states [19].

Simulation of high energy physics experiments is essential in predicting the spectral shape of the expected signals from SM or new physics processes as well as the expected backgrounds arising from the particle collisions. It provides important input in defining the detector design for any future measurements. Moreover, a precise and reliable simulation is also necessary in interpreting experimental results and allowing to pin down a weak signal from a very large number of events as is the case with LHC. Only with a complete simulation can one consistently predict and estimate the plethora of various processes, being either physical in origin or caused by the background processes. The increasing power of simulation is enormous and becomes of fundamental importance in a wide range of applications for HEP experiments.

1.2.2 Future upgrades of the LHC and new accelerators

One of the LHC objectives is to reach a higher beam energy and higher luminosity. Increasing the accelerator energy allows the creation of more massive particles, while enhancing the production rate of known particles such as the Higgs boson. After the end of Run 2, the beam energy is expected to reach the design energy of 14 TeV (Figure 1.1) with a luminosity reaching around 2 times the design value. After 2024 the so-called High Luminosity LHC (HL-LHC) is expected to come in operation with an energy of 14 TeV and a luminosity 5 to 7 times bigger than the design LHC luminosity. This will allow to collect up to 3000 fb^{-1} of data up to 2037. The increased amount of data will allow to measure the Higgs couplings, as well as other processes, with a much higher precision thereby allowing us to access rare processes that could provide evidence for physics beyond the SM.

It is worth mentioning that in the meantime, CERN has begun investigating another ambitious project, called LHeC, which studies the possibility of converting the LHC into an electron-hadron collider. A possibility for increasing the energy of the LHC is also being studied. The so-called High Energy LHC (HE-LHC) aims to increase the c.o.m. energy to around 33 TeV, which would require superconducting magnets with a field reaching up to 20 Tesla. In addition more wide-scale projects, involving the construction of a new accelerator tunnel are also under study. The so-called Future Circular Collider (FCC) study is investigating the possibility of building a new accelerator tunnel with a circumference of up to 100 km. This could house a proton-proton collider reaching energies up to 100 TeV or it could be converted into an electron-positron or electron-hadron machine. These future upgrades are expected to immensely increase the discovery potential for new physics in the multi-TeV range.

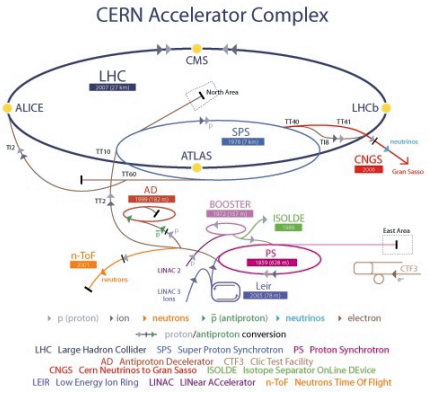

Figure 1.1: *CERN's accelerator structure is a succession of particle accelerators that can reach increasingly high energies. The Large Hadron Collider (dark blue) is a 27 km high technology structure which includes 1,695 magnet cryostats and 10,170 electrical junctions carrying current to the dipole and quadrupole magnets [20].*

1.3 The International Linear Collider concept

The envisaged International Linear Collider (ILC) concept is a worldwide program of particle physics investigations, using multiple approaches. Most probably, ILC will be the main focus in future scientific opportunities and it is expected to provide a deeper insight in the electroweak symmetry breaking mechanism and other new phenomena in the TeV energy range.

The ILC will consist of a series of superconducting accelerating niobium cavities operating at about 2 K, which will accelerate electron and proton beams (in bunches of only 5 nm) up to an energy of ∼500 GeV each. The ILC, shown in (figure 1.2), consists of two linear accelerators placed in front of each other in a straight line, which allows to eliminate the phenomenon of synchrotron radiation produced by the LHC circular geometry. The two beams, consisting of about 10^{10} electrons and positrons collide at the center of the machine, annihilating into new particles via the exchange of intermediate resonances. While at the LHC the proton-proton collisions produce multiple partons and corresponding jets making thus the Higgs identification a difficult task, at the ILC the energy resulting from the annihilation will be e.g., in the form of a Higgs boson accompanied by only few other particles, providing thus a much cleaner environment than the LHC. This is the main advantage of an e^+ e^- machine compared to a hadron collider such as the LHC.

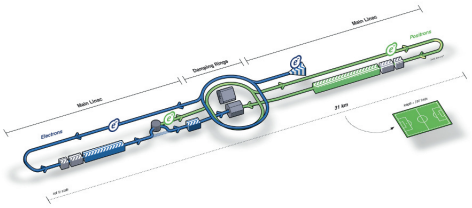

Figure 1.2: *The concept of a linear accelerator. Figure taken from [25].*

The ILC physics program includes investigating the electroweak symmetry breaking mechanism through precision measurements of processes involving the production of Higgs bosons. All major Higgs decay modes can be measured individually, even ones with a very low branching ratio, such as $h \to c\bar{c}$ or $h \to gg$, which is very difficult in hadron colliders. Many of the Higgs couplings can be measured with a precision of less than 1%, thereby allowing to probe small deviations from the SM, which could indicate the presence of new physics.

Another one of the main physics goals is a detailed study of the production of a top quark-antiquark pair. A scan around the top production threshold at 350 GeV will provide a precise and model-independent determination of the top quark mass, the top width, its Yukawa coupling to the Higgs as well as of the strong coupling constant. These could also provide insights into the presence of new physics which couples strongly to

heavy particles.

Direct searches for new physics are also possible and are complementary to those carried out in hadron colliders, since the lepton machines can probe corners of phase space which are not accessible in hadron colliders. For instance dark matter models which predict a small mass difference between the stable neutral dark matter particles and their charged partners lead to signals which contain decay chains where many soft particles are being produced. These are too soft to pass the high trigger thresholds that are used in a hadron collider environment but they could easily be detected in the cleaner environment offered by a lepton-lepton machine.

The ILC should access new physics through high resolution detectors. The next generation HEP experiments will require high detector performance as we will see later on this work.

CHAPTER 2

GASEOUS DETECTORS

Outlook

The first gaseous detector was introduced in 1908 by H.Geiger under the form of cylindrical single-wire counters [28]. Since then, gaseous detector evolution accelerated and today, gaseous detectors are able to detect all kinds of radiation with energy above 4 eV. Their operation is based on the avalanche detection, triggered by the primary ionization and developed in the so-called amplification region. The developed electric signal is collected on patterned electrodes that provide a 2D position measurement. A third coordinate can be derived from the time measurement when a drift region with a low electric field is present.

G.Charpak et al. [30] introduced the Multiwire Proportional Chamber (MWPC) in 1968. The MWPC consists by one anode and two cathode wires. The distance between the anode and cathode wires between 1 and 2 mm. The MWPC's principle of operations is based on the amplification process, during which an avalanche is created near the anode wire. This avalanche induces a negative signal on the anode whereas the cathode sees an induced positive signal. Additionally, the time projection chamber (TPC) developed by D.Nygren [31] is another type of detector that uses a mix of electric and magnetic fields and finds important physics applications.

During this work we have chosen and analyzed several gas mixtures. We have analyzed properties of different gas concentrations always based on the desired detector performance. This work was part of the Gossip detector preparation for beam tests. Section 2.1 explains the principle of operation of the gaseous detectors as well as the processes in the drift volume. In Section 2.2 we outline the state of the art detector concepts. Section 2.3 goes through various gas mixtures and their drift properties and finally, in Section 2.4 we present some candidate argon-based gas mixtures for gaseous detectors.

2.1 Principle of operation

The operation principle of gaseous detectors is the detection of the electron–ion pairs formed when a (fast, charged) particle passes through a gas medium. This particle interacts with many atomic electrons. This could either move these electrons to a higher shell within the absorber atom (excitation) or completely free the electron from the atom (ionization). By applying an electric field, the electron–ion pairs can be separated: they drift in opposite directions, towards the anode and cathode, respectively. A current starts to flow between the anode and cathode, although to create a detectable signal in most cases the electrons are first multiplied by a (local) strong electric field to achieve an electron avalanche.

2.1.1 Energy loss

Ionization by photon absorption

Photons with energy lower than 1 GeV release electrons via two different channels which are; the photoelectric effect and the Compton scattering. The main difference between these two channels is the fact that during the photoelectric effect the photon is fully absorbed whereas during the Compton phenomenon the photon scatters and loses portions of its energy.

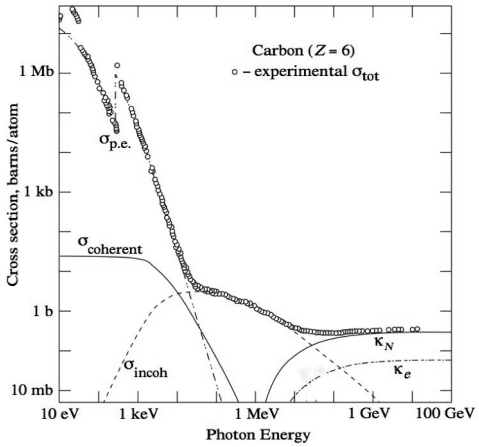

Figure 2.1: *Total photon cross-sections of carbon (gas compound commonly used as quencher) for different processes related to the photon energy [46]. $\sigma_{p.e}$ is the atomic photoelectric effect, $\sigma_{coherent}$ is the Rayleigh scattering and σ_{incoh} is the Compton scattering. The κ_N and κ_e are the cross-sections for the pair production.*

In addition, during the photoelectric effect and if the electron energy is higher than the binding energy of the weakest bound electrons (about 10 eV), ionization happens.

Photons with energy higher than 1.022 MeV pair production (creation of an electron–positron pair) may take place and more electrons may be released [36]. Figure 2.1 shows the total cross-section for different processes as it related to the photon energy.

Ionization by charged particles

Relativistic, charged particles lose their energy through ionization and/or atomic excitations ($\beta\gamma$<1000 in Figure 2.2). The mean energy loss per unit length of material traversed, <dE/dx>, is well modeled by the Bethe formula:

$$- < dE/dx >= Kz^2 \frac{Z}{A} \frac{1}{\beta^2} \left[\frac{1}{2} ln \frac{2m_e c^2 T_{max}}{I^2} \beta^2 \gamma^2 - \beta^2 - \frac{\delta(\beta\gamma)}{2} \right] \tag{2.1}$$

where K=$4\pi N_A r_e{}^2 m_e c^2$ and the classical electron radius $r_e = \frac{e^2}{4\pi\epsilon_0 m_e c^2}$.

The T_{max} is defined as:

$$T_{max} = \frac{2m_e c^2 \beta^2 \gamma^2}{1 + \frac{2\gamma m_e}{M} + (\frac{m_e}{M})^2} \tag{2.2}$$

and for low energies:

$$T_{max} = 2m_e c^2 \beta^2 \gamma^2 \tag{2.3}$$

where β=v/c represents the particle's velocity, e its charge, m_e the electron rest mass and $\gamma = (1\text{-}\beta^2)^{-1/2}$ the relativistic factor.

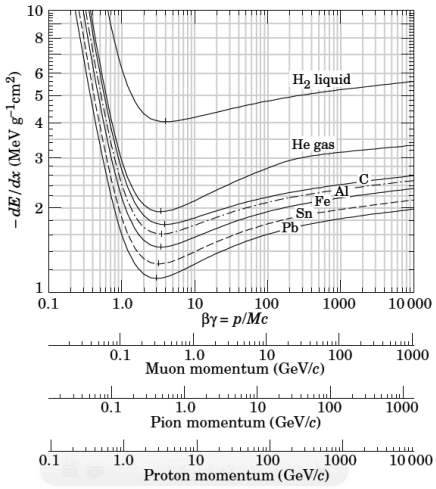

Figure 2.2: *The mean energy loss of charged particles drifting in liquid hydrogen, gas helium, carbon, aluminum, iron, tin, and lead. Figure taken from [38].*

Figure 2.2 illustrates the charged particle mean energy loss [MeV cm^2 per g] and as it behaves in a wide energy range. The region of the so-called MIPs appears at a kinetic energy greater or equal to few times the particle's rest mass. This figure refers to positive muons, pions and protons and provides a good approximation for other charged particles too. According to the relation 2.1, the energy loss initially decreases with $1/\beta^2$ and goes through a minimum at $\beta\gamma \sim 3.2$. At high velocities, the maximum energy transfer increases further and the energy loss per unit length rises - known as the relativistic rise region.

2.1.2 Drift properties

Inside the drift volume of a detector and under an applied electric field electrons drift towards the anode and the ions (positively charged) move towards the cathode which is at a negative voltage. In wire chambers, the electric filed is strong and electrons which approach the wire enter the amplification area in which the charge is amplified. The bi-dimensional spatial resolution is determined by both the granularity of the amplification grid or mesh and the segmentation of the readout electrodes beneath the mesh (wires, pads, or a pixel chip) [36].

Micro-Pattern Gaseous Detectors (MPGD) are widely used in High Energy Physics experiments. The amplification grid of a MPGD is adopted to the fine granularity of pixel chips with cell sizes down to 50×50 μm^2 [36]. Figure 2.4 shows the path of a transversing charged particle and the anode (chip) which measures the projection of the ionized trace which indicates how much time it takes for the electrons to hit the anode. Drift velocity is the particle's average velocity under the application of an electric field. The higher the drift velocity the better the detector's performance.

In the absence of electric field, the detector's ambient temperature defines the particle's kinetic energy: $\frac{3}{2}$k$_b$T where k$_b$ is Boltzmann's constant and T the temperature (K). This means:

$$\frac{3}{2}k_bT = \frac{1}{2}mu^2 \Rightarrow u = \sqrt{\frac{3k_bT}{m}} \tag{2.4}$$

For room temperatures the thermal energy is about 0.04 eV with an average velocity of about 11 cm/μs. For the same temperature the velocity of noble gas atoms is about 10^{-2} cm/μs.

An applied electric field will give to the electrons a net (constant) velocity, u$_d$, which results from the balance between the electron energy gained by acceleration and the electron energy lost through collisions. The equation of motion of electrons in this case, according to Langevin [47] and [48] is:

$$m\frac{d\vec{u}_e}{dt} = e\vec{E} + e(\vec{u_e} \times \vec{B}) - K\vec{u_e} \tag{2.5}$$

where u$_e$ is the electron drift velocity, K is the energy lost by collisions inside the gas volume and K=m/τ with τ being the average time between two collisions. If we consider

a constant drift velocity ($d\vec{u}_e/dt=0$) the Equation 2.5 becomes:

$$\vec{u}_d = \frac{e}{m}\tau|\vec{E}|\frac{1}{1+\omega^2\tau^2}(\hat{E}+\omega\tau(\hat{E}\times\hat{B})+\omega^2\tau^2(\hat{E}\cdot\hat{B})\hat{B}) \tag{2.6}$$

where $\hat{E}=\frac{\vec{E}}{|\vec{E}|}$, $\hat{B}=\frac{\vec{B}}{|\vec{B}|}$ and $\omega=\frac{e}{m}$B is the cyclotron frequency. In case there is no magnetic field the u_d becomes:

$$\vec{u}_d = \frac{e}{m}\tau\vec{E} = \mu_e\vec{E} \tag{2.7}$$

where μ_e is the electron mobility. Equation 2.7 is valid for thermal electrons.

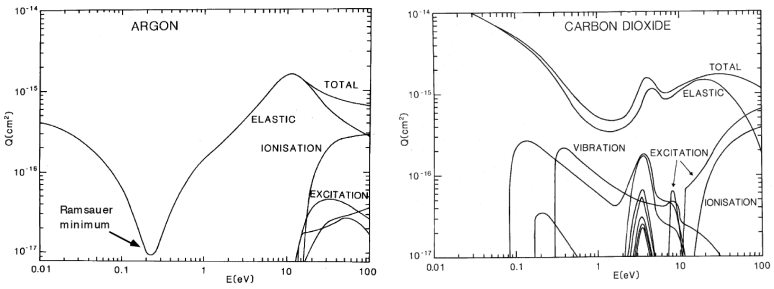

(a) Argon (b) Carbon dioxide

Figure 2.3: *Electron collision cross-sections for (a) Ar and (b) Carbon dioxide. Figure taken from [43].*

The above figure 2.3 shows the Ramsauer minimum for noble gases (this thesis studies extensively noble gases and noble gases components). It is worth mentioning here that the heavier the noble gas the higher the energy in which we observe the Ramsauer minimum (e.g. no minimum for Helium while for Xenon the minimum appears at around 0.65 eV). Thermal (eV) electrons drift through a gas volume and loose their energy via elastic collisions with the gas atoms. Given that the thermal de Broglie wavelength of a thermal electron is similar in size with these atoms, the cross-section shows a "drop" that corresponds to the electron's collisions. The average energy loss between two particles with masses m_1 and m_2 that undergo an elastic collision is given by the following formula:

$$f = \frac{2m_1m_2}{(m_1+m_2)^2} \tag{2.8}$$

Equation 2.8, demonstrates that electrons loose small amount of their energy since the difference between the electron and the atom mass is large. This allows electrons to gain energy from the drift field. Such an increase of the electron energy leads to the excitation or ionization of the gas atoms (e.g. ionization potential for argon: 15.7 eV) [36].

By modifying the gas composition (adding a quencher) once can adjust the electron velocity in low electric fields. In particular, by adding a quencher, i.e. CO_2, CH_4,

etc., in the main detector gas, we manage to increase the drift velocity of the electron without increasing the electric field. As an example, for electron energies up to ∼1 eV, the cross-sections for CO_2 are larger (by an order of magnitude) than the cross-sections for argon while CO_2 cross-sections fall with energy up to ∼2 eV and argon cross-sections show the Ramsauer minimum, at 0.23 eV (Figure 2.3) [36].

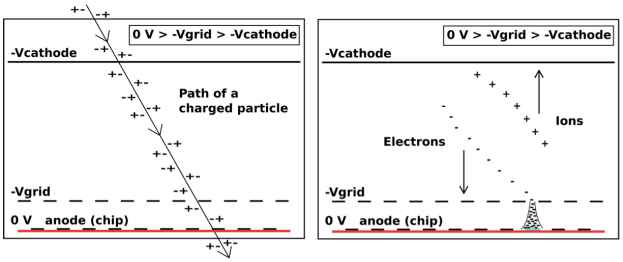

Figure 2.4: *Operation principle of a GridPix gaseous detector. Left: transversing charged particle creates electron-ion pairs. Right: the applied electric field separates the pairs and drifts the electrons towards the anode (negative signal) and ions towards the cathode (positive signal). The electron amplification results in an avalanche when the electron enters the amplification region and a pixel hit can be observed [36].*

As we will see later on this chapter, there are two types of diffusion; the transverse and the longitudinal diffusion. The transverse diffusion limits the spatial resolution while the longitudinal diffusion defines the resolution in the direction along the path of the charged particle. Given the short drift distance between the anode and the cathode, longitudinal diffusion is less important than the transverse diffusion. The electrons that enter the amplification region and cause the electron amplification pass through the holes in the grid (Figure 2.4). The electrons hit the pixel and create the signal induced on the electrode. The electron's signal together with the ion's which move to the opposite direction (towards the cathode) gives the measured signal. An overview of all these parameters is given in Section 2.3.

2.1.3 Amplification

One fundamental aspect in all gas detectors is the avalanche or multiplication. Multiplication is needed for the production of an electrical signal of sufficient amplitude. In theory, a strong electric field makes all gases able to generate electron avalanches. However, depending on the mode of operation and the intended use of the detector, specific demands such as high gain, drift properties and short recovery times limit the choice of gas.

The amplification of electrons occurs when sufficient voltage is applied over a small range where the electrons arrive. Ions increase modestly their average kinetic energy between collisions with surrounding neutral atoms due to their heavy mass. Free electrons are lighter and are therefore accelerated by the electric field. When electrons gain

kinetic energy above the ionization energy of neutral atoms an additional electron–ion pair can be created due to the transfer of the electrons' kinetic energy in a collision. Both electrons will then be accelerated in the electric field until their next collision. This process is called electron amplification. The time development of an avalanche in a wire detector is depicted in Figure 2.5. For micro pattern detectors studied in this thesis the geometry is slightly different but the process is similar.

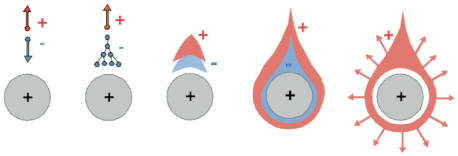

Figure 2.5: *The time development of an avalanche in a detector. An electron–ion pair is separated by an electric field. The electrons gain kinetic energy in the electric field and ionize other atoms. The electron and ion clouds drift apart towards the anode (wire) and the cathode [59].*

The total charge on a detector (actually induced on the electrode) generated by the passing particle is:

$$Q = n_0 e G \tag{2.9}$$

where Q is the charge (eV), n_0 the number of primary electrons, e the electron charge (eV) and G is the gas amplification factor, or gain of the avalanche. The number of electrons created in the avalanche after a certain drift path is:

$$dn_e = n_0 \alpha ds \tag{2.10}$$

where n_e is the total amount of electrons in the avalanche, α the Townsend coefficient (Section 2.3) and ds the distance over which the electron amplification occurs. The Townsend coefficient is connected to the electric field, the gas density, the excitation and ionization cross-sections and energy transfer mechanisms. The Townsend coefficient must be determined from data since there is no analytical expression for it. By intergrating Equation 2.10 we derive the total number of electrons that were created over the drifting distance ds:

$$n_e = n_0 e^{\alpha ds} \tag{2.11}$$

The gain can be expressed as a function of this coefficient solving Equations 2.9 and 2.10:

$$G = \frac{n_e}{n_0} = e^{\alpha ds} \tag{2.12}$$

which shows that for a given uniform electric field E the ratio of the total number of electrons over the number of electrons before the amplification defines the amplification factor G known as gas gain.

2.2 Micro Pattern Gaseous Detectors

2.2.1 GEMs

The Gas Electron Multiplier (GEM) (Figure 2.6 (a)) is a gaseous grid detector which consists of two metal layers separated by a thin insulator which is depicted with a hole matrix [41]. It was invented in 1996 by Sauli [27]. GEM's gas volume consists of three parts: a low field region (produced primary charge), a high field region (inside the grid holes) and a transfer region [41]. A GEM and its electric field configuration is shown in Figure 2.6 (b).

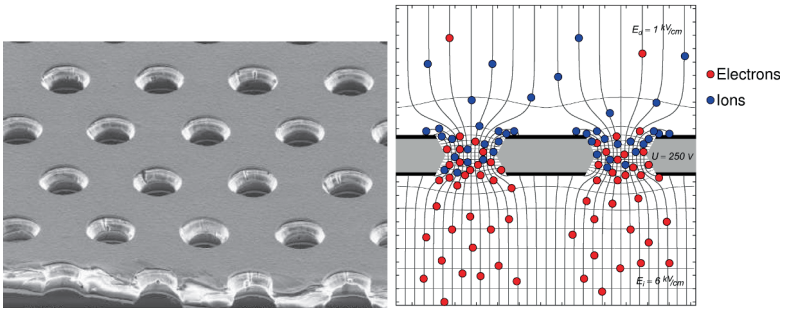

(a) (b)

Figure 2.6: *Photograph of a GEM (a) and its electric field configuration (b). Pictures taken from [42].*

2.2.2 Micromegas

Micromegas (MICROMEsh GAseous Structure) has been developed from principles of the conventional wire chamber. It was invented in 1995 by I. Giomataris et al. [69]. The gas volume is split into two characteristic layers (by a thin micro-mesh which is at a negative potential and sustained at a fixed distance from the anode), the drift and the amplification region [51]. In the region above the mesh, the conversion or ionization region, the electron-ion pairs are produced by the conversion of x-rays (photoelectric effect) or by the ionization along a charged particle's track. The released electrons are drifting towards the micro-mesh (and then into the amplification region) by a moderate drift electric field. The thickness of this region ranges from few mm to few meters in the case of a large TPC.

The liberated electrons drift towards the mesh, which they pass with a high efficiency thanks to the funnel shape of the field lines. In the following amplification region, a high electric field causes an avalanche which leads to a large number of electrons producing thus an electric signal at the anode. The geometry of the amplification region is important for achieving high efficiency.

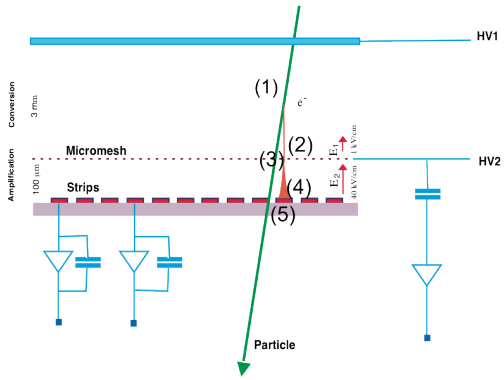

Figure 2.7: *Working principle of a Micromegas detector. A passing charged particle (green arrow) is drifted through the gas volume which has two main areas separated by a micro-mesh ("Micromesh" on this diagram) [70].*

2.2.3 Gossip

The combination of a Micromegas and a readout chip is dubbed InGrid [111]. The mesh is built in a post-processing step similar to the production of bulk-Micromegas and consists of 50μm high insulating pillars (SU-8) and a 0.8μm thick aluminum plane with holes that are aligned with the pixels of the CMOS chip. The gas amplification avalanche of a single primary electron is mainly collected on a single pixel or spread over a few neighboring pixels. The smaller signal spread results in larger signals per pixel and thus, smaller gas gains are necessary. Tests showed, however, that CMOS chips are vulnerable to discharges triggered by high charge densities.

Gossip (Gas On Slimmed Silicon Pixels) is a pixel detector based on InGrid but with a drift region of only a mm. The drift field separates the electron-ion pairs: the pixels are grounded and the grid is set to a negative potential. Under an applied electric field and with drift time of only 16 ns, each electron will create an avalanche between the CMOS chip surface and the InGrid. By applying a potential difference of 400 V in the 50 μ gap a gas multiplication, known as gain, equal to 1000 can be reached [52].

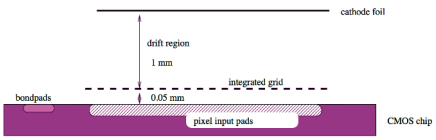

Figure 2.8: *Schematic view of the Gossip detector.*

The basic Gossip principle is shown in Figure 2.8. Gossip is under study for the ATLAS

upgrade. When the drift time measurements can be used to obtain a vector-like measurement of a track it is interesting to use the detector for the level 1 trigger. For use in ATLAS, detectors need to cope with high interaction rates and fast readout (40 MHz bunch crossing rate). In addition the detectors should run continuously for several years without significant performance loss due to radiation damage and/or aging.

2.3 Selecting a gas mixture

In noble gas, avalanche multiplication can occur at relatively moderate electric fields. By adding more components in the gas mixture we manage to increase the threshold voltage. However, noble gases do not allow detector operation at high gas gain. During the avalanche, the excited atoms de-excite, emitting photons at energies that could cause new avalanches in the gas medium. Such avalanches could put the detector into a discharge operation. The same effect could also happen by the ions that move in the opposite direction (towards the cathode). The solution to this problem came with the addition of a quencher. A quenching gas is a gas which absorbs energetic photons (often this is an organic gas like isobutane (iC_4H_{10}).

The most efficient organic compounds for absorbing energetic photons are found between hydrocarbons and alcohols. Small amounts of quencher(s) in a gas mixture can change completely the operational characteristics of a detector. For example, gains greater than 10^6 could be obtained before a discharge happens. Known gas mixtures are the 90% Ar+10% CH_4 (P10) for proportional counters and 75% Ar + 24.5% iC_4H_{10} + 0.5% Freon for (proportional) multi wire chambers (MWPCs).

For chambers with long drift times there are other requirements which apply. For example, such chambers require really good drift properties with special attention to the drift velocity. For a chamber who is intended to obtain a good spatial resolution, the drift velocity should be low in order to diminish the effect of timing errors on the position resolution. On the other hand, for a high counting operations, the drift velocity of the charged particle should be as high as it takes in order avoid losses due to the dead time. Gases like dimethylether (DME) or CO_2 could be used when long drift time is required.

Also, gas purity is important. Even a minor contamination may deteriorate chamber operation. For example, it might change the drift velocity of the electrons or one may loose electrons due to attachment. Finally there are practical considerations that limit the choice of gases that can be used for the ideal mix. To avoid premature aging some compounds need to be eliminated but this topic is outside the scope of this thesis. Inflammable, toxic and radioactive components should be avoided in the gas mixture and are most of the times simply forbidden. The development of a flame depends on the nature of a gas component, its temperature, its pressure, and mostly on its concentration. In practice, by controlling the amount of a component in the gas mixture we can get a non-inflammable mixture (e.g. CO_2 with low concentration of oxygen).

2.3.1 Electron drift velocity

Figure 2.9 shows the simulated electron drift velocity for two different gas mixtures at T=300°K and 1 atm. The simulation was made with the Garfield and Magboltz programs. For this work, the important component where we focus is the one parallel to the electric field (orange color). This component is related to the Lorentz angle and diffusion. (More gas mixtures are shown in the Appendix).

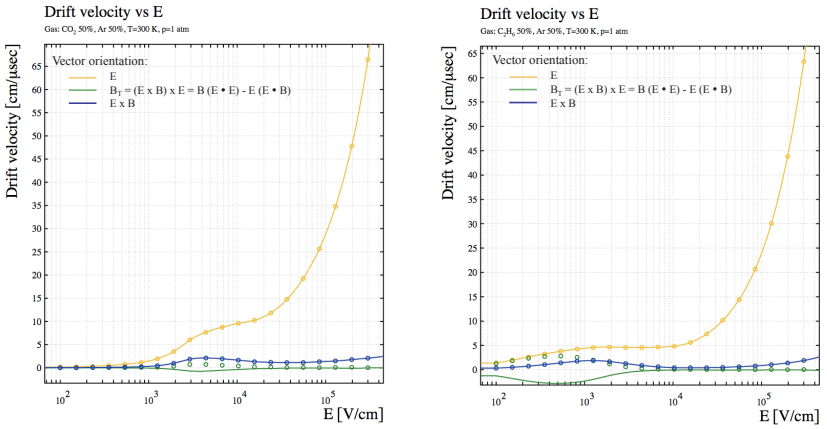

(a) Ar:CO_2 (50:50) (b) Ar:C_2H_6 (50:50)

Figure 2.9: *Electron drift velocity under an applied electric field for the following gas mixtures: (a) Ar:CO_2 and (b) Ar:C_2H_6. Different colors represent different components of the drift velocity. Orange: component parallel with the electric field (0°), green: component parallel with the orthogonal part of the magnetic field (45°) and blue: component parallel with ExB (90°). Magboltz simulation.*

2.3.2 Electron and ion diffusion

The presence of a quencher helps in order to limit the sidewalks of the electrons or in other words the transverse diffusion. In addition, a small electron diffusion implies larger electron drift velocity. Figure 2.10 shows the electron longitudinal and transverse diffusion in relation to the applied electric field for two different gas mixtures: (a) Ar:CO_2 and (b) Ar:C_2H_6. In Figures 6.31 and 6.32 electron diffusion is shown for various gas mixtures. (More gas mixtures are shown in the Appendix).

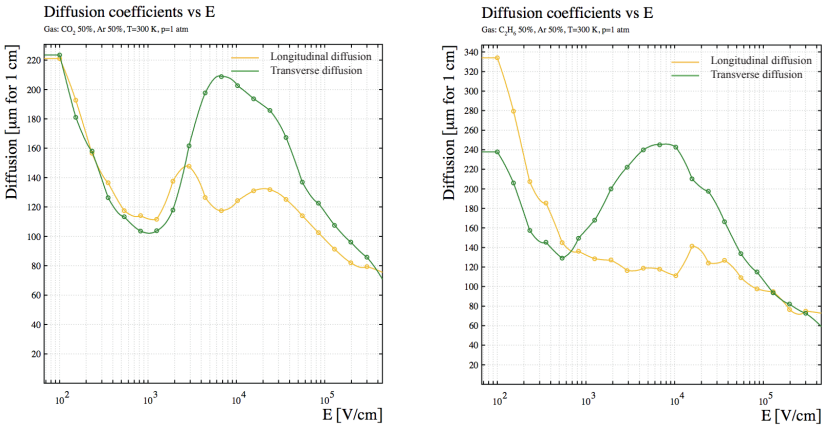

(a) Ar:CO_2 (50:50) (b) Ar:C_2H_6 (50:50)

Figure 2.10: *Magboltz simulation of the longitudinal (yellow) and transverse (green) diffusion under an applied electric field for (a) Ar:CO_2 and (b) Ar:C_2H_6. Transverse diffusion (green) is the diffusion perpendicular to the drift direction and longitudinal diffusion (orange) is the diffusion in the drift direction.*

2.3.3 The Lorentz angle

Particle detectors are usually operated inside a magnetic field. The moving particles are forced to change moving directions due to the magnetic field. The angle by which the particles are deflected is called Lorentz angle. The Lorentz angle can be used e.g. to enhance charge sharing. If the goal is to minimize the Lorentz angle, the drift velocity (ν) should be low, but the electric field (E) should be high (in case the electric and magnetic fields are orthogonal).

$$tan\theta = \mu B, \ where \ \mu = \frac{\nu}{E} \tag{2.13}$$

In Figure 2.11 we show the Lorentz angle between drift velocity and electric field for several gas mixtures. The curves correspond to a 90° angle between electric and magnetic field. (More gas mixtures are shown in the Appendix).

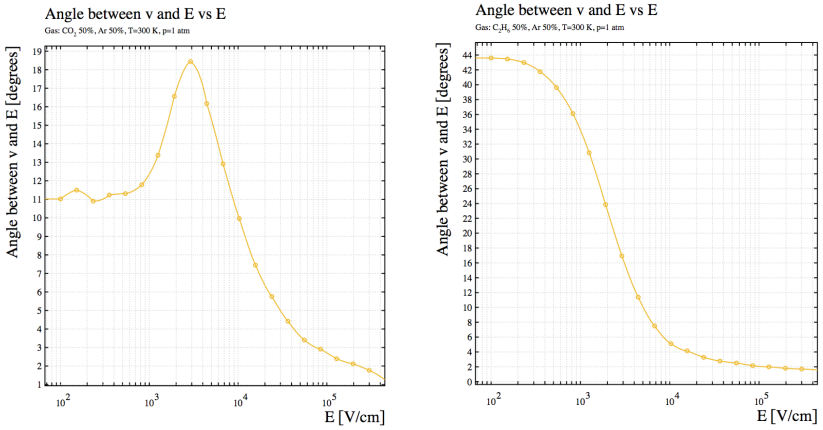

(a) Ar:CO_2 (50:50) (b) Ar:C_2H_6 (50:50)

Figure 2.11: *Magboltz simulation of the Lorentz angle for the E×B component as a function of the electric field for (a) Ar:CO_2 and (b) Ar:C_2H_6.*

2.3.4 The Townsend and attachment coefficients

The Townsend coefficient α, represents the number of ionizing collisions for an e^- per cm of path length in the direction of the applied electric field. One of the most desirable goals is high gain since the resolution improves with it. For this reason, we are looking for gas mixtures with high α, and preferably a low threshold for the avalanche at low field values. A gas mixture with large α (preferably at low electric fields due to the avalanches) can give a high gas gain.

The attachment coefficient η represents the probability that a drifting electron will experience electron attachment. It is very important for both particle's position and its identification. Losses of avalanche electrons due to attachment are important for the signal calculation and therefore we need a gas mixture with low attachment coefficient. The following plots show the behavior of the Townsend (orange) and attachment (green) coefficients under an applied electric field for two different sets of gas mixtures (dissociation coefficient not shown here). (More gas mixtures are shown in the Appendix).

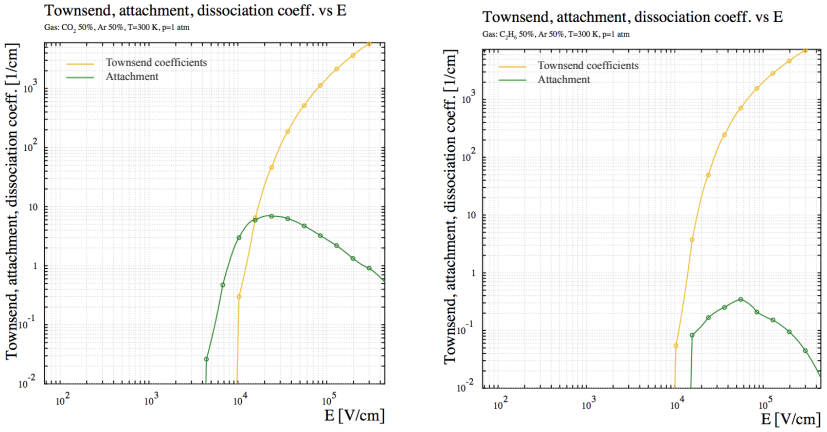

(a) $Ar:CO_2$ (50:50) (b) $Ar:C_2H_6$ (50:50)

Figure 2.12: *Magboltz simulation of the Townsend and attachment coefficients as a function of the electric field for (a) $Ar:CO_2$ and (b) $Ar:C_2H_6$. Townsend (orange) and attachment (green) coefficients.*

2.4 Gossip gas

The ideal gas mixture does not exist. The desired detector performance, the purpose and the detector geometry dictate the choice of the gas mixture. Gossip as a candidate detector is studied for the ATLAS inner tracker, and hence it will have to operate in a 2 T magnetic field. The following simulation results were produced for a Gossip detector of 50 μm avalanche gap and for a gas gain equal to e^8 ($\approx$ 3000).

$$Gain = e^{a \cdot gap} \tag{2.14}$$

Given the equation 2.14 for a gas gain $\sim$3000, we can calculate the Townsend coefficient α. For the case of Ar/CO_2, $\alpha \approx 1600$/cm. Knowing the value of α we can find the electric field for the amplification volume by using the Figure 2.12 (E_{amp} $\approx$100 kV/cm). Afterwards, from Figures 2.9 and 2.10 we can calculate the electric field in the drift volume and therefore the Lorentz angle (Figure 2.11). In this work we present simulation results from two points of view; (a) the minimum transverse diffusion and (b) the maximum drift velocity. The tables 2.1 and 2.2 summarize the most important drift properties for various argon-based gas mixtures and indicate the most proper gas mixture for the Gossip detector.

Table 2.1: *Drift properties as they were calculated for gas gain equal to 3000. These results are based on the minimum transverse diffusion.*

Gas mixture	E_{amp} [kV/cm]	E [V/cm]	Drift v [cm/μs]	$\boldsymbol{\sigma_T}$ [$\boldsymbol{\mu}$m]	σ_L [μm]	Lorentz angle [deg]
Ar:CO_2 [50:50]	105.6	1032	v_E: 1.52 v_{BT}: 0.08 $v_{E\times B}$: 0.33	**102**	123	(v_E,v_{BT}): 3.02 (v_E,$v_{E\times B}$): 12.1
Ar:C_2H_6 [50:50]	86.4	545	v_E: 3.81 v_{BT}: 2.82 $v_{E\times B}$: 1.42	**123**	119	(v_E,v_{BT}): 36.4 (v_E,$v_{E\times B}$): 20.5
Ar:CH_4 [50:50]	96.8	545	v_E: 6.62 v_{BT}: 5.96 $v_{E\times B}$: 1.73	**145**	133	(v_E,v_{BT}): 41.9 (v_E,$v_{E\times B}$): 14.6
Ar:CH_4 [90:10]	82.8	223	v_E: 3.89 v_{BT}: 3.64 $v_{E\times B}$: 0.72	**225**	222	(v_E,v_{BT}): 43.1 (v_E,$v_{E\times B}$): 10.5
Ar:CF_4 [50:50]	90.4	1059	v_E: 8.61 v_{BT}: 6.45 $v_{E\times B}$: 3.78	**54.8**	54.4	(v_E,v_{BT}): 38.6 (v_E,$v_{E\times B}$): 22.2
Ar:CF_4 [80:20]	83.4	767	v_E: 8.11 v_{BT}: 7.21 $v_{E\times B}$: 2.54	**74.7**	95.9	(v_E,v_{BT}): 41.7 (v_E,$v_{E\times B}$): 17.3
Ar:CF_4 [90:10]	81.3	637	v_E: 8.04 v_{BT}: 7.36 $v_{E\times B}$: 2.11	**94.9**	149	(v_E,v_{BT}): 42.5 (v_E,$v_{E\times B}$): 14.7
Ar:DME [90:10]	78.1	285	v_E: 0.83 v_{BT}: 0.22 $v_{E\times B}$: 0.33	**173**	171	(v_E,v_{BT}): 15.3 (v_E,$v_{E\times B}$): 22.7
Ar:DME [50:50]	87.2	1442	v_E: 1.13 v_{BT}: 0.02 $v_{E\times B}$: 0.14	**83.6**	96.3	(v_E,v_{BT}): 1.01 (v_E,$v_{E\times B}$): 6.91
Ar:CF_4:CO_2 [60:10:30]	98.1	1238	v_E: 2.85 v_{BT}: 0.37 $v_{E\times B}$: 0.94	**103**	117	(v_E,v_{BT}): 7.59 (v_E,$v_{E\times B}$): 18.3
Ar:CO_2:iC_4H_{10} [80:10:10]	81.3	395	v_E: 1.67 v_{BT}: 0.71 $v_{E\times B}$: 0.81	**159**	148	(v_E,v_{BT}): 22.9 (v_E,$v_{E\times B}$): 25.9
Xe:CF_4:CO_2 [50:30:20]	89.7	1765	v_E: 3.28 v_{BT}: 0.29 $v_{E\times B}$: 0.91	**82.1**	75.4	(v_E,v_{BT}): 5.09 (v_E,$v_{E\times B}$): 15.3

Table 2.2: *Drift properties based on maximum drift velocity.*

Gas mixture	E_{amp} [kV/cm]	E [V/cm]	**Drift v [cm/μs]**	σ_T [μm]	σ_L [μm]	Lorentz angle [deg]
Ar:CO_2 [50:50]	105.6	5000 (no max)	**8.01**	203	123	(v_E,v_{BT}): 4.88 (v_E,$v_{E\times B}$): 14.6
Ar:C_2H_6 [50:50]	86.4	1744	**4.67**	192	127	(v_E,v_{BT}): 36.4 (v_E,$v_{E\times B}$): 20.5
Ar:CH_4 [50:50]	96.8	690	**6.75**	151	161	(v_E,v_{BT}): 40.3 (v_E,$v_{E\times B}$): 16.6
Ar:CH_4 [90:10]	81.3	800	**8.27**	101	108	(v_E,v_{BT}): 41.1 (v_E,$v_{E\times B}$): 16.9
Ar:CF_4 [50:50]	90.4	3174	**11.5**	98.5	55.5	(v_E,v_{BT}): 19.4 (v_E,$v_{E\times B}$): 25.3
Ar:CF_4 [80:20]	83.4	1507	**9.45**	109	83.7	(v_E,v_{BT}): 35.4 (v_E,$v_{E\times B}$): 23.1
Ar:CF_4 [90:10]	81.3	800	**8.27**	101	108	(v_E,v_{BT}): 41.1 (v_E,$v_{E\times B}$): 16.9
Ar:DME [90:10]	78.1	1529	**3.64**	299	162	(v_E,v_{BT}): 12.8 (v_E,$v_{E\times B}$): 20.3
Ar:DME [50:50]	87.2	5000 (no max)	**4.94**	157	96.3	(v_E,v_{BT}): 1.66 (v_E,$v_{E\times B}$): 8.61
Ar:CF_4:CO_2 [60:10:30]	98.1	5000 (no max)	**8.08**	213	117	(v_E,v_{BT}): 5.54 (v_E,$v_{E\times B}$): 15.1
Ar:CO_2:iC_4H_{10} [80:10:10]	81.3	5000 (no max)	**5.36**	262	148	(v_E,v_{BT}): 3.36 (v_E,$v_{E\times B}$): 11.3
Xe:CF_4:CO_2 [50:30:20]	89.7	4905 (no max)	**7.98**	151	76	(v_E,v_{BT}): 5.81 (v_E,$v_{E\times B}$): 15.7

From the tables 2.1 and 2.2 it is obvious that the number of candidate gas mixtures and gas concentrations that one can create and test can be pretty large. However, in practice, parameters such as inflammability, cost, aging, neutron capture and toxicity restrict the use of many gas mixtures.

None of the gas mixtures presented in this work stands out as an exclusive candidate for use in the Gossip detector. Among the various reasons for this are the operational stability (sparks), the high drift velocity and the low diffusion. Nevertheless, the argon and CO_2 mixture satisfies most of these prerequisites. Moreover, argon-based mixtures provide more accurate particle identification and better spatial resolution compared to the other gas mixtures becoming thus a good candidate for Gossip.

Of equal importance, as we will see later in this work, is the choice of the detector geometry such as the hole size and pitch on the InGrid as well as the thicknesses of the drift and amplification gaps. As a result of our study, the choice of the ingredients in a gas mixture for the Gossip detector narrows down to argon and CO_2.

CHAPTER 3

SIMULATION OF ENERGY LOSS IN THIN GASEOUS DETECTORS

Outlook

While detector granularity decreases, the need for simulations of small energy transfers becomes increasingly important: A 1 keV uncertainty is negligible in simulating the energy loss of an 1 TeV particle, it is large when it transverses a μTPC (50 μm).

The aim of the simulation work presented in this Chapter is to investigate the performance of the detector response when it consists of relatively thin layers of gas as its actual active part, i.e., the conversion volume, where the primary ionization charges make their appearance. The Geant4 code is a widely used and successful software package for photons in the sub-keV range or neutrons below ∼10 MeV are not yet described satisfactorily by Geant4. The goal is to rather confirm the energy deposition for MIPs and other charged particles being ubiquitous in particular in LHC experiments. Surprisingly, the results provided here show some unexpected distributions of energy loss by highly relativistic electrons (and muons). The follow-up of such a result is explained in this Chapter.

In this Chapter we look into the energy loss of minimum ionizing particles in thin gas layers with several available software tools such as Geant4, Fluka and Heed. This analysis reveals a "shoulder" effect on the distribution of the energy loss for both Geant4 and Fluka tools. Such an effect leads to wrong simulation results for many different LHC experiments. Both Geant4 and Fluka teams focussed intensively for several months even if it did not turned out to be some new physics. As a result of this work, the Geant tool (our main focus) has been improved. In Section 3.2 we review the behavior of charged particles interacting with matter in a wide energy range. Section 3.3 provides an introduction to the software packages used during this work with focus on the Geant4 EM physics. The Section 3.4 shows some simulation results of the Geant4 for a variety of commonly used gaseous constituents and introduces a strange behavior on the energy loss. Section 3.5 presents the potential impact of different parameters aiming to identify the source of this behavior. Finally, Section 3.6 introduces the improved Geant4 EM

physics models.

3.1 Geant4 simulation

The most probable energy loss of an electron in the Geant4 code can be smaller than the energy deposited in the detector and this is because of the electron multiple scattering and the delta ray produced during the process. In some cases, the primary electron can even be completely absorbed in the detector. Both simulation of multiple scattering and of energy loss computation can be very tricky [53]. Geant4 Standard EM physics do not take into account atomic processes and do not treat low energy δ-electrons. As a result, low energy physics packages have been developed and we present them in this work.

Figure 3.1 shows the simulation of 100 electrons with energy 25 GeV. The geometry is a 15 mm thin layer of argon gas. The Figure shows 100 superimposed events.

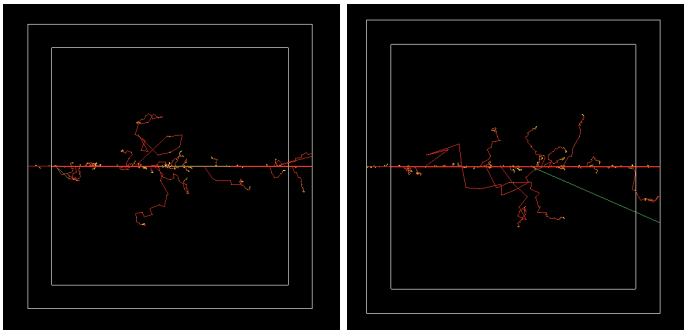

Figure 3.1: *Two similar random examples of Geant4 simulation of 100 electrons showing each time the different paths and energy depositions inside a 15 mm thin argon gas chamber. Negative charge particles are shown with red while neutral particles with green.*

3.2 Fluctuations in energy loss

In Section 3.5 we have calculated the mean energy loss of charged particles. The energy loss in a thin layer is the sum of a finite number of transfers and therefore is susceptible to statistical fluctuations. This energy loss distribution ($f_L(\epsilon,\delta x)$) of a charged particle with mass m that traverses a distance of δx is reasonably well modeled by the Landau distribution $\phi(\lambda)$ [57] and can be written as:

$$f_L(\epsilon, \delta x) = \frac{1}{\xi}\phi(\lambda) \tag{3.1}$$

where ξ is the mean energy loss as given by the first term of the Bethe-Block formula and:

$$\phi(\lambda) = \frac{1}{2\pi i} \int_{r-i\infty}^{r+i\infty} e^{\,u \ln(u) + \lambda u}\, du \tag{3.2}$$

where r is an arbitrary positive real constant and the variable λ is:

$$\lambda = \frac{\epsilon - \bar{\epsilon}}{\xi} - \gamma' - \beta^2 - \ln \frac{\xi}{T_{max}} \tag{3.3}$$

where

$$\begin{aligned} \gamma' &= 0.422784 \cdots = 1 - \gamma \\ \gamma &= 0.577215 \ldots \text{(Euler's constant)} \\ \bar{\epsilon} &= \text{average energy loss} \\ \epsilon &= \text{actual energy loss} \end{aligned}$$

Note that the very long tail of the Landau distribution (Figure 3.2) corresponds to low-probability events with large energy losses. The energy deposited in a thin layer does not exactly correspond to the energy lost by the traversing charged particle, since the energetic δ-rays (responsible for the Landau tail) can escape from the thin layer [54]. Therefore, the fluctuations in the energy deposited are less significant in thick layers. The tail of the ideal Landau distribution extends to infinite energies (unrealistic), while in practice the measured range is of course limited [55].

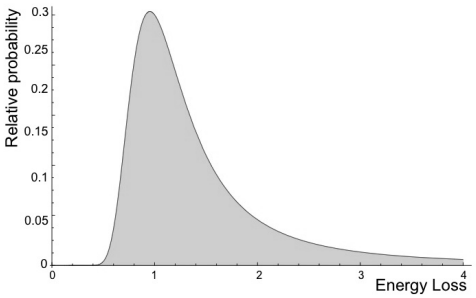

Figure 3.2: *The energy loss of a charge particle traversing a thin absorber follows a Landau distribution. The mean energy loss is asymmetric towards higher energies due to high-energetic δ-rays. Theoretically, the Landau tail extends to infinite energies, while in practice the measured range is limited.*

The Landau distribution describes the energy loss in thin absorbers. The mean energy loss is small compared to the largest energy which can be transferred in any single collision. Yet, for the Landau approximation to be valid, the layer must be sufficiently

thick for ξ to be large compared with the ionization potential I of the material that is traversed. In our example, we use argon gas (1 atm at room temperature) which has an ionization potential of 15.7 eV and the Landau approximation is accordingly expected to fail only for d $<$ 10 – 100 μm, which is much smaller than the used thickness of a chamber.

A practical problem associated with the Landau distribution and its continuation to the infinity is that a mathematical calculation does not allow to derive a mean. Having an undefined mean leads to large and unphysical fluctuations when generating Monte Carlo events and occasionally energy losses will exceed even the kinematic limit. As mentioned in reference [54], the Landau theory has two restrictions:

1. Energy loss is small when compared to the maximum energy loss in one collision and
2. Energy loss should be larger than the binding energy of the electrons. In fact, for gaseous detectors (e.g. argon gas), energy loses are similar to the binding energies of the inner argon electrons (about 3 keV). Moreover, Geant4 makes use of the parametrized model by L. Urbán accounting thus atomic energy levels [60].

3.3 Software packages

The main goal of a successful Monte Carlo simulation in the LHC environment is to provide an accurate response of all the detector parts given the large amounts of particles which transverse the various parts of the detector [68]. In this work, we describe developments made in the electromagnetic physic models between the Geant4 releases 9.3 (December 2009) [44] and 9.4 (December 2010) [45].

3.3.1 Geant4

The EM physics processes in Geant4 include numerous models for the simulation of EM interactions of charged particles, photons and optical photons with the detector materials. By combining different models and processes the simulation can cover from eV to TeV energies [68]. The EM processes have no actual limitation in the energy range. Physics tables with cross-sections, energy losses and energy ranges cover the range from 0.1 keV to 100 TeV. EM processes and models are separated in two categories;

1. the Geant4 EM Standard working group is developing and maintaining the Standard EM physics which includes precise cross-sections above 1 keV and a 1 keV minimum production limit for secondary particles [97] and
2. the Geant4 EM Low energy group supports low energy processes and models with applications in HEP experiments, space science, astrophysics, medical and biological fields. The processes include cross-sections above 10 eV depending on the specific model used.

Both standard and low-energy models are valid in the energy range between 1 keV and 1 GeV [97]. At low energies (below few keV), Geant4 includes parametrized cross-sections, stopping powers and other physical data provided by evaluated data libraries.

To be included inside simulation software a parametrization of the data is required. In that case a substantial effort goes to the comparison between simulation results and evaluated data in order to validate and improve Geant4 in this energy range.

Interfaces of EM Standard and EM Low energy models allow Geant4 EM Physics to combine ultra relativistic, relativistic and low-energy models for all Geant4 EM process achieving high accuracy and performance for a wide energy range [68].

Table 3.1: *Geant4, HEED and Fluka EM physics.*

EM Physics	γ	e^-	e^+
Geant4 Standard	up to 100 TeV	up to 100 TeV	-
Geant4 Low Energy			
Livermore	250 eV – 100 GeV	250 eV – 100 GeV	-
Penelope	250 eV – 1 GeV	250 eV – 1 GeV	250 eV – 1 GeV
PAI	250 eV – 100 GeV	250 eV – 100 GeV	250 eV – 100 GeV
HEED (PAI)	below 10 eV (no Compton)	below 50 eV (treat as δ-e^-)	few keV (treat as δ-e^-)
Fluka	1 keV – 1000 TeV	1 keV – 1000 TeV	1 keV – 1000 TeV

The precision of the simulation depends on chosen theoretical models, parametrization methods, tracking frameworks, and software implementations. All these specifications of the Standard EM physics are described in details in the Geant4 Physics Reference Manual [66]. For a simulation to be accurate and provide correct results the simulation tool, i.e., Geant4 needs to be validated against either experiment data (if available) or older versions of the Geant4 tool. Geant4 EM physics lists are groups of models and processes. In this work, we compare the Standard EM physics models with the Low Energy EM physics models. All these packages contain alternative models for the same physics processes.

The Standard EM physics models in Geant4, do not emit secondary e^-/γ below a set threshold whose range falls typically to $\sim$1 keV. When secondary particles reach these energies are absorbed locally. Low energy EM physics models in Geant4 but also in simulation codes such as Heed, follow low-energy particles taking into account atomic/molecular quantum effects, e.g., inner shell ionization, emission of Auger electrons and fluorescent photons. When such details are included, the overall simulation is improved.
The main Geant4 physics models are:

Standard: The physics is often called "Geant4 Standard EM Physics" [97]. In this work we used the most generalized model called Default. It assumes that the projectile particle has energy greater than 1 keV. The atomic electrons as well as the nucleus are consider (quasi)free and the nucleus' recoil energy is negligible. The Standard EM models are used in a major part of Geant4 Physics Lists such as QGSP BERT, FTF BIC, etc.

Livermore: Livermore physics is based on available evaluated data libraries from the Livermore data libraries (LLNL); EADL (Evaluated Atomic Data Library), EEDL (Evaluated Electrons Data Library) and EPDL97 (Evaluated Photons Data Library) [97]. These libraries mix experimental data and theoretical estimates and contain interpolated data tables and total cross-sections for photoelectric effect, Compton and Rayleigh scattering, pair production and Bremsstrahlung. It also includes secondary electron processes. Each of these processes involve two separated phases; the computation and use of total neutron cross-sections and the final state generation which are based on theoretical and evaluated data models [97]. Its validity range is from 250 eV up to 100 GeV. In principle, it is valid for energies down to ∼10 eV. However, it is not used below 100 eV due to the limited accuracy. In fact, Standard EM models, which are optimized for HEP applications are based on the parametrization of these data. Livermore includes elements with Z from 1 to 100. It contains atomic effects such as fluorescent γ, Auger electrons, and atomic relaxation for Z>5 (data from EADL). It provides high accuracy for electrons, hadrons and ions.

Penelope: Penelope (PENetration and Energy LOss of Positrons and Electrons) [63], is another low-energy model [97]. It has also been designed to provide higher accuracy results (similar to Livermore) [97]. Penelope is a Monte Carlo code and provides at Geant4 low-energy models for $e^{\pm}$ and gamma rays. It is a mixed code and can be described as analytical, parametrized and database-driver. Its applicability energy range is from 250 eV to 1 GeV. Unlike Livermore, Penelope includes also positrons. Penelope and Livermore are low-energy models used as alternatives to the standard models when EM showers and interactions (down to the keV range) need to be treated with high precision. They should also be used when atomic effects (e.g. fluorescence) are of interest. Both models are CPU-consuming due to the intensive simulation they provide.

Geant4 Photoabsorption Ionization: The G4 Photoabsorption Ionization (PAI) [64], model describes the ionization energy loss of charged particles in thin layers of absorbers and the δ-electrons production by charged particles. PAI ionization is implemented according to the model approach "G4 PAI Model". PAI model provides a detailed simulation of ionization being thus a slow model. It allows the calculation of the energy loss due to ionization in any material with elements with atomic number Z between 1 and 100. It includes the generation of fluorescent photons from excited states and Auger electrons. We recall: the Auger effect takes place when the e^- that is removed from the inner-shell creates a vacancy and an e^- from a higher energy level moves to this vacancy by releasing the energy difference of the two energy levels. Sometimes this effect "competes" with the gamma emission (fluorescence). For the case of argon the binding energy of a K-shell electron is 3.2 keV.

3.3.2 Fluka

Fluka is a software tool meant to calculate particle transport and interactions with matter in a wide range of applications [99]. It transports charged particles in many ways;

by switching on/off either δ-ray production and/or ionization fluctuations (continuous slowing down approximation) and by choosing different energy thresholds. In principle, the Fluka code is less reliable than the PAI model since it is not able to generate neither fluorescent γ nor Auger electrons. Figure 3.5 shows the ionization energy loss deposited in a chamber with 15 mm thickness. The chamber is filled with a gas mixture which contains 80% Ar and 20% CO_2 and is exposed to electrons of 500 MeV/c momentum.

3.3.3 Heed

The Heed program [65], is designed to simulate the ionization patterns created by charged particles traversing a nearly arbitrary gas mixture. An underlying assumption in the code is that the hadrons lose only a small part of their energy in the process. Heed can also process the absorption of low-energy photons below $\sim$10 keV. It is widely used and tested by HEP experiments even though is not designed to simulate heavily ionizing particle.

The part of the program that computes the ionization energy loss by a charged particle in a gas mixture is based on the PAI model. Heed goes much further than any other simulation code by containing the electron energy levels inside the gas and by using them to generate (and re-absorb) fluorescent γ and Auger electrons from excited states. Heed also combines a detailed model for the transformation of the energy transferred to the gas into spatial ionization patterns, with the appropriate fluctuations.

One of the weaknesses of the PAI model is the inability to calculate the transverse distribution of the ionization aside from the track which in some cases can be important. In other words, PAI can not differentiate the shells which absorb the energy and therefore, does not estimate the range of δ-electrons knocked out from the atoms. To overcome this weak point, PAI model was improved. By modifying its cross-sections the PAI model was able to discriminate the atomic shells, to model atomic relaxation cascades and to model the paths of the δ-electrons and fluorescent photons. The improved model is called PAIR (Photoabsorption Ionization and Relaxation model).

3.4 Gaseous constituents used in μTPCs

This work focuses on noble gases and quencher constituents, therefore we simulate the ionization energy loss for different gas mixtures. For a gas layer thickness of 15 mm, we test the ionization energy loss for argon, carbon, hydrogen, neon, oxygen and xenon. All the materials are set to approximately same density (argon gas density: ρ=1.782 mg/cm^3). The size of the gas ionization is relevant to the ionizing particle's properties (i.e. energy), the gas atomic number and density, and the ionization potential of the gas mixture.

Table 3.2 lists some values for n_p and n_t in some commonly used gases [50]. Where n_p represents the amount of primary electron pairs per cm and n_t the total number of electron-ion pairs. Both n_p and n_t depend on the incident particle's charge and velocity, and are characteristic of the gas mixture. W_i represents the average energy needed in

order to produce one electron-ion pair. $[dE/dx]_{mip}$ is the energy loss of the ionizing particle [34].

Table 3.2: *Some gas properties at normal temperature and pressure.*

Gas	$[dE/dx]_{mip}$ (keV cm^{-1})	W_i (eV)	n_p (cm^{-1})	n_t (cm^{-1})
Ar	2.53	26	25	97
Xe	6.76	22	44	307
H	0.34	37	5.2	9.2
He	0.32	41	5.9	7.8
O	2.26	31	22	73
Ne	1.41	36	12	39

Figure 3.3 shows, energy loss distributions for different gases. Although there is some agreement, we see that at these low energies the models do not give the same shape of the energy loss distribution.

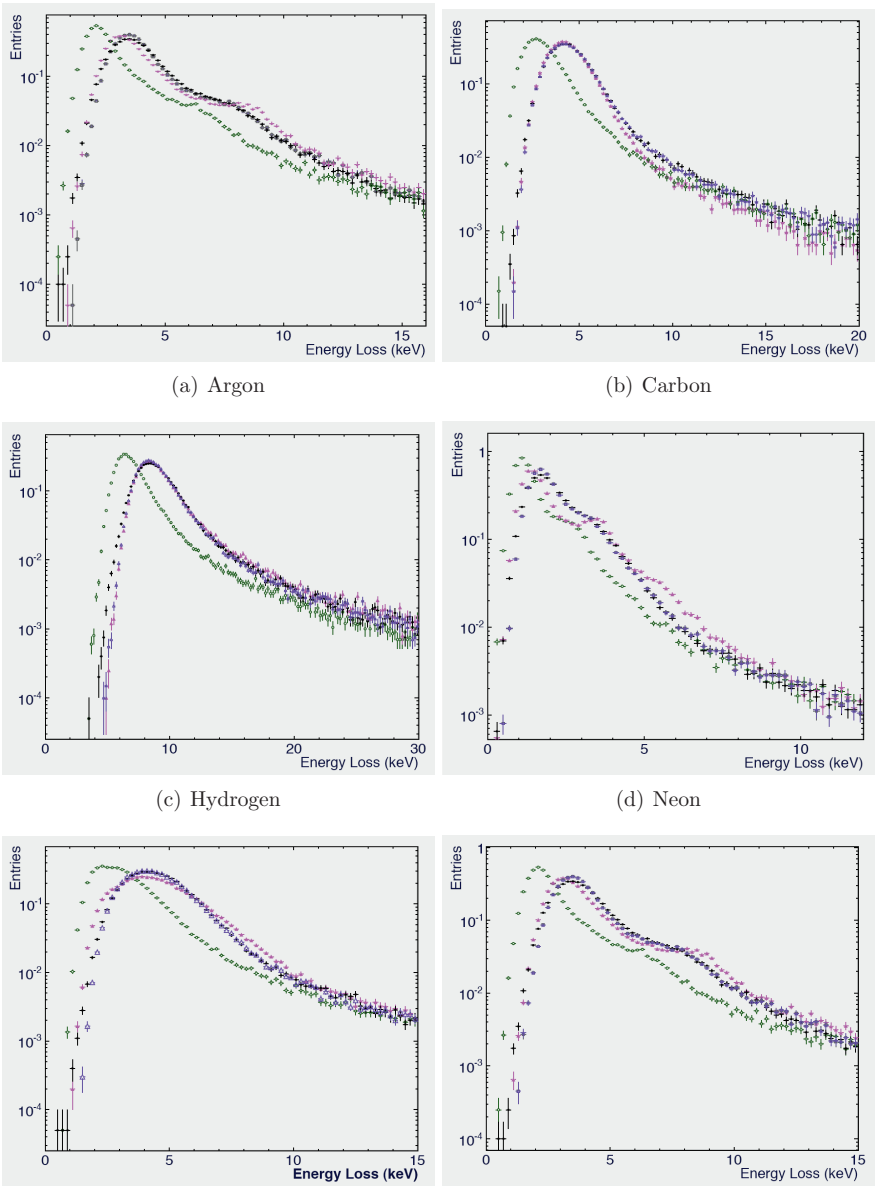

(a) Argon (b) Carbon

(c) Hydrogen (d) Neon

(e) Oxygen (f) Xenon

Figure 3.3: *Ionization energy loss of 500 MeV/c electrons in a 15 mm thin gas layer filled with (a) Argon, (b) Carbon, (c) Hydrogen, (d) Neon, (e) Oxygen and (f) Xenon. Livermore (green), Penelope (pink), Standard (black) and G4 PAI (purple).*

3.5 Simulation results

Following all the reasoning given in Section 3.2, we expect a smooth function that especially on the high energy tail does not show any distinct features. However, the Geant4 simulated energy loss of relativistic charges in thin layers (i.e., a thin layer as defined above) was not as smooth as expected. Instead, as Figure 3.4 shows, a shoulder appears on the ionization energy loss on the higher energetic side of the expected distribution.

The calculation of the energy loss by ionization is made primarily for electrons. Our target is a thin layer (15 mm) of 80% Ar and 20% CO_2 gas mixture. The incident electron beam (500 MeV/c) is sent vertical to the centre of the thin layer.

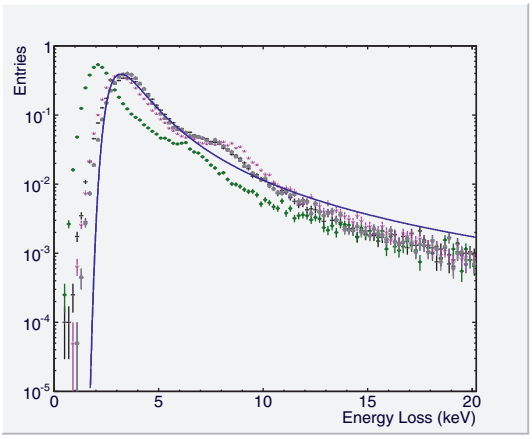

Figure 3.4: *Ionization energy loss by electrons with momentum 500 MeV/c, through a 15 mm thin layer of 80% Ar and 20% CO_2 at 1 atm pressure, using the different physics models: Livermore (green), Penelope (pink), Standard (black) and G4 PAI (purple). Unexpectedly and surprisingly in all models a shoulder appears on the high energy tail (between 6 and 9 keV). A typical Landau distribution is also shown (blue line).*

The energy loss distribution in a thin gas layers is shown in Figure 3.4. The figure shows similar behavior of all models. More specifically, all models indicate a shoulder distribution at 6 – 9 keV. Since there is no experimental data to explain it, its identification is mandatory. The goal of this work is to identify the source of this behavior and correct it. The peculiar behavior of all Geant4 models described earlier for different gaseous constituents requires further studies. Probably the low energy behavior is not well defined and this is the effect we observe. In the following Sections we present more detailed validation results as well as comparisons with simulation tools beyond Geant4.

Fluka and Heed

There are some other simulation tools which are used to predict the ionization energy loss by charged particles, beyond Geant4. Due to the lack of data in the energy range of interest, we turn our attention to Fluka and Heed simulation codes. Both codes are valid down to low energies for the simulation of the energy loss of particles in matter.

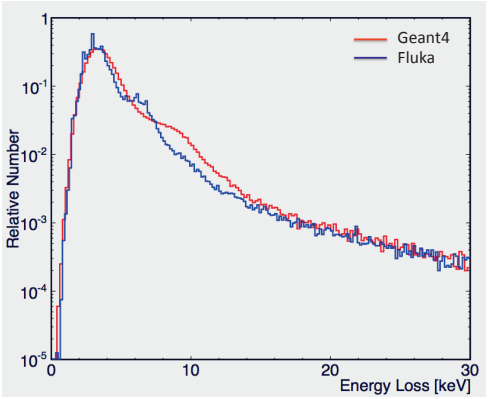

Figure 3.5: *Electrons of 500 MeV/c incident on a 15 mm thin chamber, filled with 80% Ar and 20% CO_2. Geant4 Standard (red) and Fluka (blue) apply the same physics with different approaches. The Fluka result was rather expected due to its similar limited simulation details with Geant4 (i.e. absence of generation of Auger electrons and fluorescent γ) the appearance of the shoulder in different energies is something unforeseen.*

Both Geant4 and Fluka tools seem to suffer from the same effect. Interestingly, the position of the shoulder differs between the two tools even if all the simulation details (i.e. geometry, gas composition, etc.) are the same. Such a result was not expected due to the similarity of the two simulation codes and their physics applied (e.g. absence of generation of Auger electrons and fluorescent photons). The behavior of the ionization energy loss simulated by the Fluka code indicates the need of another more reliable physics justification. For this reason, in this work we present similar simulation results with the Heed simulation program.

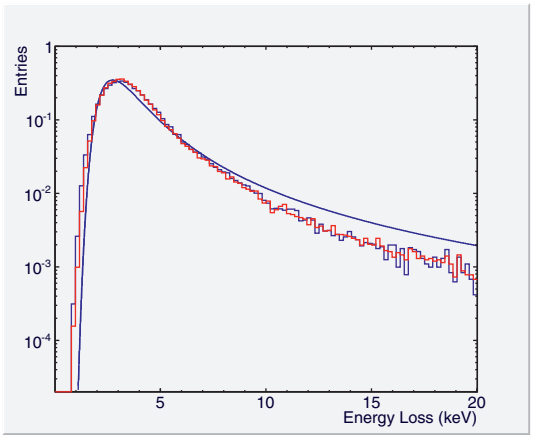

Figure 3.6: *Ionization energy loss of electrons in 15 mm thin layer of 80% Ar and 20% CO_2 as simulated by the Heed code. The two available models in the Heed code: PAI model (light blue) and PAIR model (red) show no significant discrepancies while both are in good agreement with the Landau distribution (smooth blue line).*

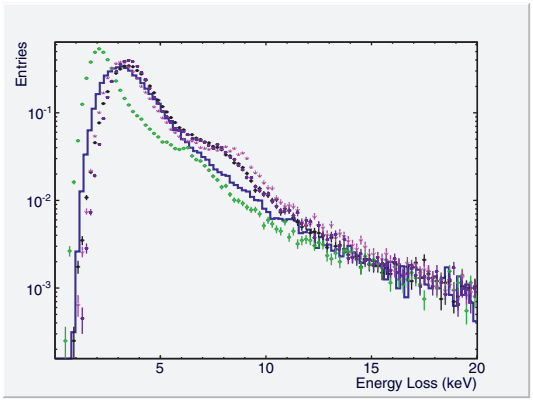

Figure 3.7: *Ionization energy loss of electrons in 15 mm thin layer of 80% Ar and 20% CO_2, using the four available Geant4 models: Livermore (green), Penelope (pink), Standard (black) and G4 PAI (purple). The Heed PAI model is shown with the rather smooth blue line. The overall behavior of Geant4 and Heed is similar with only exception the energy range from $\sim$6 – 10 keV, and the shoulder appearance on the Geant4 models.*

Therefore, the Heed code and its PAI/PAIR models exhibit the best simulation of the energy deposited in the chamber. Taking into account the precise simulation of Heed's models (through the generation of fluorescent γ, Auger electrons and the modeling of relaxation cascades) we conclude that the shoulder effect is something abnormal and it

originates from the Geant4 code. The same conclusion has been taken for the Fluka code (and the responsible Fluka team has been informed).

Geant4 code does not have (so far) a model comparable to PAIR. For this reason and since for our simulation there is no significant difference between Heed's PAI and PAIR models, we continue using Heed's PAI model as a reference. Thus, the PAI and PAIR models as resulting from the Heed program are more reliable comparing them with both Geant4 and Fluka tools. This is due to the precision of these models which follow and treat low-energy particles like $e^{\pm}, \gamma$, etc., taking into account atomic/molecular quantum effects, such as inner shell ionization, emission of Auger electrons and fluorescent photons.

Discussion

Figure 3.8 shows a comparison between Geant4, Heed and Fluka simulation codes. As it can be seen, the general features of the three codes are rather similar. Since the observed differences are significant, they have been investigated. Heed with its detailed and precise simulation through the PAI model indicates the anomalous behavior of the other two codes.

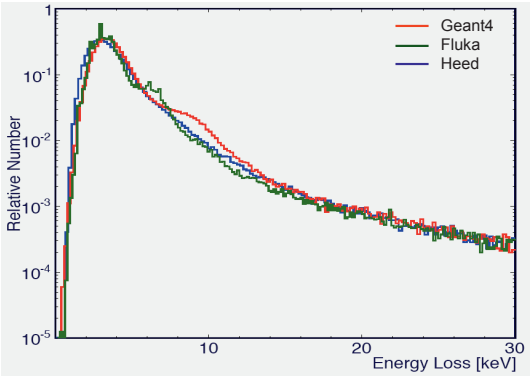

Figure 3.8: *Ionization energy loss of electrons with 500 MeV/c momentum in a 15 mm thin gas layer (80% Ar and 20% CO_2) as simulated with the Geant4 (red), Fluka (green) and Heed (blue) codes. The three codes clearly disagree in the shoulder range with Heed having no shoulder, Geant4 with a shoulder peak at ∼9 keV and Fluka with a shoulder peak at ∼8.5 keV.*

For the improvement of Geant4 we focus in the code and more explicitly in its simulation specifications such as type of particles, geometry details and physical processes. The goal is to identify the source of this shoulder behavior and in parallel validate general features of Geant4.

Incident energy

Each one of the plots given in Figures 3.9 and 3.10 show the ionization energy loss for electrons and muons. The target volume is a thin layer (15 mm) of 80% Ar and 20% CO_2. The electrons and muons are sent perpendicular to the centre of the thin layer having each time a different energy. As it is obvious from the figures, the shoulder that the Geant4 EM models produce depends on the initial e^-/μ^- energies as far as its position and shape are concerned.

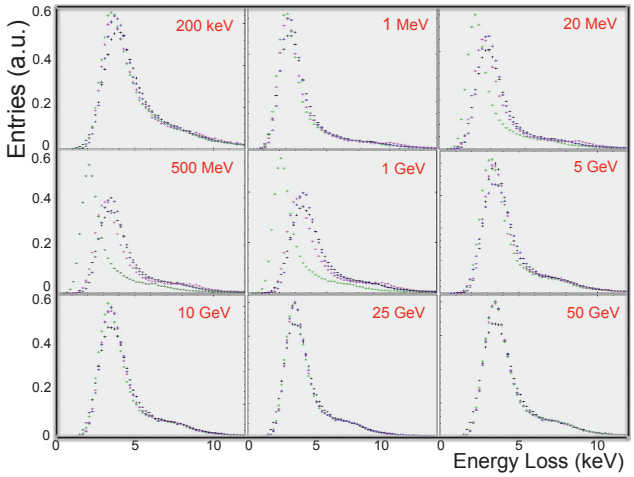

Figure 3.9: *Ionization energy loss for various incident electron energies (15 mm thin layer of 80% Ar and 20% CO_2). Livermore (green), Penelope (pink), Standard (black) and G4 PAI (purple). In addition, the simulation shows that Livermore model is not reliable in the energy range from 1 MeV to 5 GeV.*

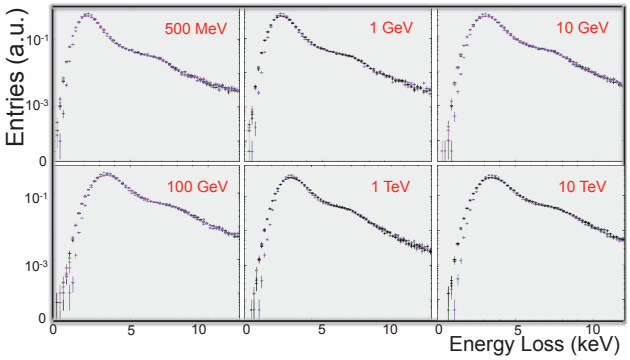

Figure 3.10: *Ionization energy loss for various incident muon energies (15 mm thin layer of 80% Ar and 20% CO_2). Livermore (green), Penelope (pink), Standard (black) and G4 PAI (purple). Unlike the case of e^-, in the case of μ^-, all the Geant4 models agree in all energy ranges including the shoulder's behavior.*

As the electron energy increases (from 200 keV up to 50 GeV) the shoulder becomes more and more stronger. An interesting result here is the fact that the discrepancies between the Geant4 models are large. As an example, we mention the misbehavior of the Livermore distribution which is not accurate at the medium energy region (∼1 MeV to ∼10 GeV). For the case of muons (Figure 3.10), the agreement between the models is good.

Detector gas thickness

Figure 3.11 shows the ionization energy loss of 500 MeV/c electrons. The gas layer consists of 80% Ar and 20% CO_2 and has various thicknesses. The electrons are always sent perpendicular to the centre of each layer. As one can see, the shape of the shoulder depends on the thickness of the detector. More specifically, it starts as a wide bump for thick layers (i.e. 96 mm) of gas and becomes a shoulder as the layer becomes thinner (i.e. 0.75 mm). The agreement between different physics models is poor for very thin layers. Figures 3.12 and 3.13 present in more detail, all the Geant4 models as they behave for two different gas layers: (a) 0.75 cm and (b) 3 cm, for electrons and muons.

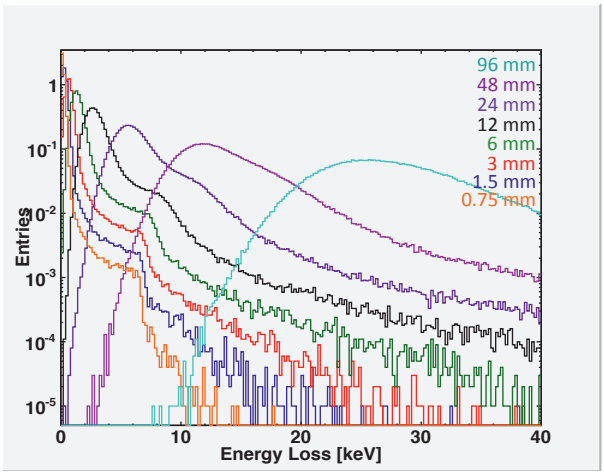

Figure 3.11: *Ionization energy loss of electrons of 500 MeV/c. Geant4 Standard model behavior as we move from thick to thinner gas layers of 80% Ar and 20% CO_2 (from the right to the left).*

For the thinnest gas layer (0.75 cm) the shoulder effect is rather strong for all four models while for a four times thicker gas layer is much weaker. One could understand this, since in thicker layers the charged particle has to interact accordingly more often with the gas atoms/molecules and the deposited energy distribution becomes more and more smooth, and this, as it is expected, in all energy ranges.

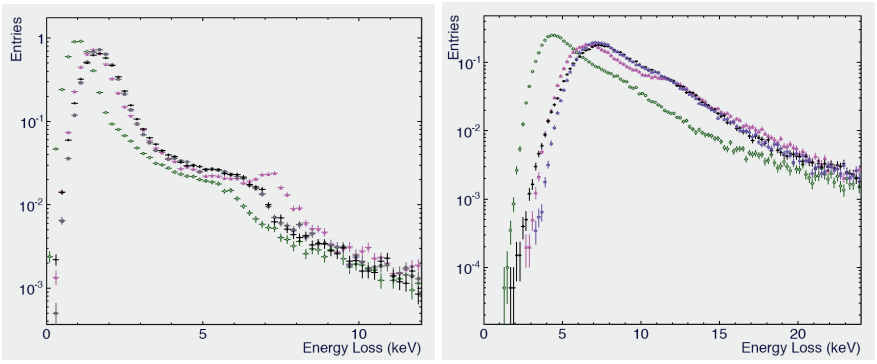

(a) 0.75 cm (b) 3 cm

Figure 3.12: *Geant4 EM models for chamber thicknesses: (a) 0.75 cm and (b) 3 cm. Electrons with momentum 500 MeV/c are sent perpendicular to a gas chamber filled with 80% Ar and 20% CO_2. Livermore (green), Penelope (pink), Standard (black) and G4 PAI (purple).*

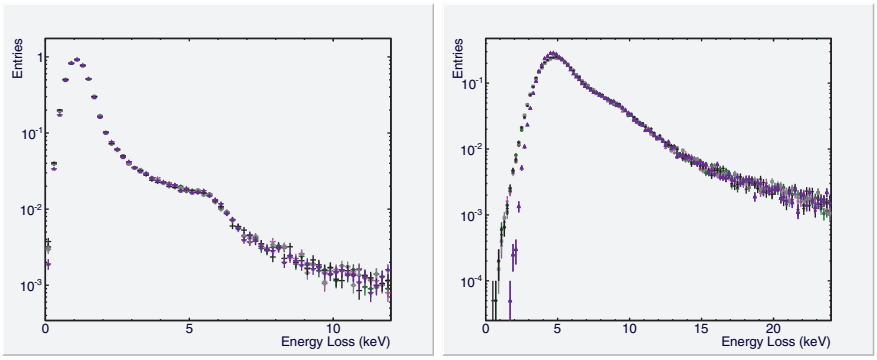

(a) 0.75 cm (b) 3 cm

Figure 3.13: *Geant4 EM models for chamber thicknesses: (a) 0.75 cm and (b) 3 cm. Muons with momentum 500 MeV/c are sent perpendicular in a chamber filled with 80% Ar and 20% CO_2. Livermore (green), Penelope (pink), Standard (black) and G4 PAI (purple) are in agreement.*

Investigation of Geant4 at 25 GeV/c electrons

In this Section, we consider the ionization energy loss of 25 GeV/c electrons (in a 15 mm thin gas layer) as a study case. The main reason for that, is the fact that at this

energy all the models are behaving similarly (see Figure 3.14). In the next Sections we do not focus on the differences between the various Geant4 models but rather on the overall performance of Geant4. We use Figure 3.14 as a reference since it has no special requirements (all processes/models are activated by default). Below we present various results aiming at the identification of the origin of the shoulder.

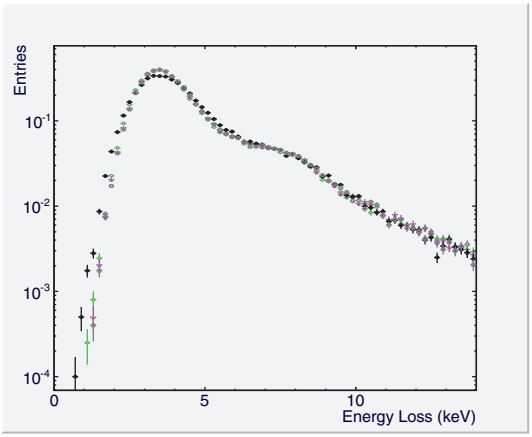

Figure 3.14: *Ionization energy loss of 25 GeV/c electrons in 15 mm gas thin layer (80% Ar and 20% CO_2). Livermore (green), Penelope (pink), Standard (black) and G4 PAI (purple).*

Range cut-off

The main parameter of Geant4 EM simulation is the range cut-off which represents the accuracy of the particle's stopping position. In other words, range cut-off is the threshold (or distance) at which no secondary particles are produced anymore. The default value of the range cut-off is usually set at 1 mm, since for lower cuts the corresponding CPU time of the simulation increases. The choice of the production cut depends on two parameters. One is the desirable accuracy of the simulation for the energy deposition in the gas layer and the other is the geometry demands (i.e. different geometry regions might require different cuts or different degree of accuracy). For a given single range cut-off, Geant4 calculates the corresponding energy at which the production of secondary particles stops for each individual material.

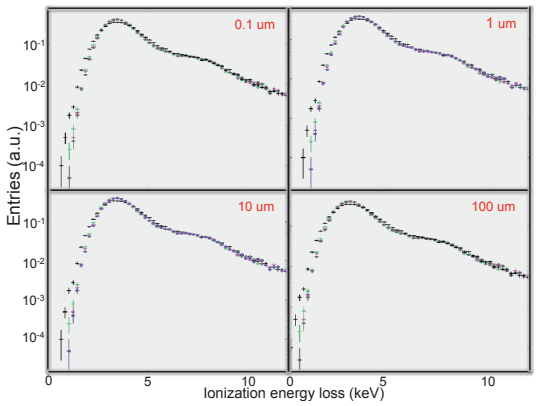

Figure 3.15: *Ionization energy loss of 25 GeV/c electrons for four different range cut-offs inside 80% Ar and 20% CO_2. Livermore (green), Penelope (pink), Standard (black) and G4 PAI (purple).*

As Figure 3.15 shows, applying various range cut-offs in all the physics models has no impact on the shape of the energy loss distribution. This means, the secondary particles play no important role. To confirm this, we activate the Geant4 process "kill secondaries". In this way, during our simulation there is no secondary particle production. Figure 3.16 leaves no doubts that also the production of secondary particles is not responsible for the shoulder in any of the Geant4 models.

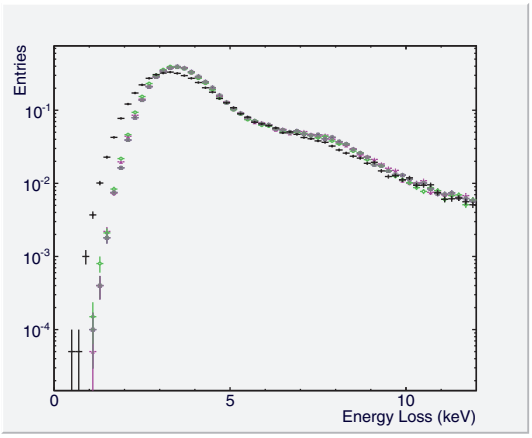

Figure 3.16: *Ionization energy loss of 25 GeV electrons with no production of secondaries. Chamber thickness: 15 mm filled with 80% Ar and 20% CO_2. Livermore (green), Penelope (pink), Standard (black) and G4 PAI (purple).*

Gas layer thickness

As we indicated earlier, the shape of the energy loss distribution depends strongly on the thickness of the gas layer. In particular, it becomes stronger for thinner gas layers. Figure 3.17 shows that indeed, also for the case of 25 GeV electrons by increasing the thickness of the chamber to 3 cm, we actually hide the shoulder effect, that is to say the increasing number of scattering processes probably does not suppress the shoulder but rather it is being washed out.

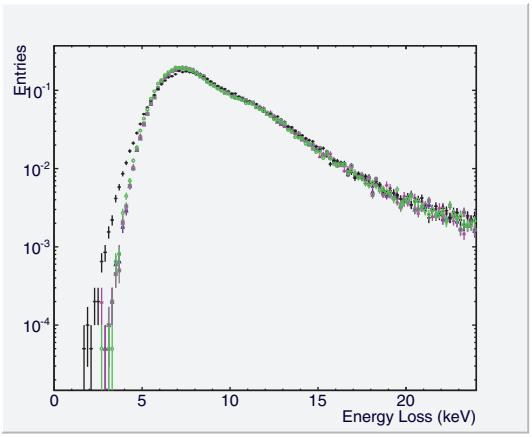

Figure 3.17: *Ionization energy loss of 25 GeV electrons. Chamber thickness: 3 cm filled with 80% Ar and 20% CO_2. Livermore (green), Penelope (pink), Standard (black) and G4 PAI (purple).*

Other processes

Aiming to eventually localize the origin of the appearance of this shoulder-like distribution of the ionization energy loss of relativistic electrons (and muons), we have tested various EM processes. In particular, we look in detail EM physics processes which can contribute to the ionization energy loss of charged particles inside the thin gas layer. The frequent occurring reactions such as Bremsstrahlung, multiple scattering and electron ionization are considered here.

The bremsstrahlung process [66], calculates the energy loss of relativistic e^- (and e^+) due to the emission of radiation when they pass near the Coulomb field of a nucleus. During the present work, we deactivated the bremsstrahlung process, meaning that the electrons do not lose/deposit their energy via this process. Moreover, in a try to understand the effect of multiple scattering process, we deactivated the process of multiple scattering process as well. The electron multiple scattering process seems also not related to the shape of the energy loss distribution.

We recall that the ionization process inside the gas provides continuous and discrete energy losses by the electron (and positron) traversing the gas layer. The value of the maximum energy an electron can transfer to a free electron is given by the following:

$$T_{max} = \frac{E - mc^2}{2} \tag{3.4}$$

where mc^2 is the electron rest mass and E the electron energy. As in the previous two cases, Figure 3.18 shows that suppressing the electron ionization has also no effect on the shoulder appearance.

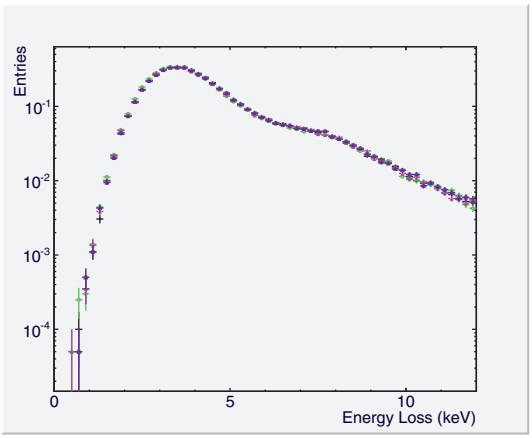

Figure 3.18: *Ionization energy loss of 25 GeV/c electrons in 15 mm thin gas layer filled with 80% Ar and 20% CO_2 while electron ionization process is deactivated. Livermore (green), Penelope (pink), Standard (black) and G4 PAI (purple).*

Fluctuations

Last but not least we look whether the nature of the statistical fluctuations in Geant4 can explain the origin of the shoulder. The fluctuation model in Geant4 (Urbán method) was introduced in 1988 [54]. The goal of its use is to produce a relatively simple and fast fluctuation code which reproduces the energy loss straggling for thin layers. The Monte Carlo method is similar to Landau theory and it can be used for any detector thickness, including thin gas layers. The first version of the Urbán fluctuation model has implemented the particle-atom interaction, while the atom is assumed to have two energy levels E_1 and E_2 [60]. In this model, the energy loss distribution is given via the function:

$$g(E) = \frac{(E_{max} + I)I}{E_{max}} \frac{1}{E^2} \tag{3.5}$$

where E_{max} is the Geant4 cut for delta-rays.

The Urbán fluctuation model computes the cross-sections for various processes and uses simple sum rules for oscillator strengths and energy levels (details can be found in the Physics Reference Manual of Geant4 [66]). The Urbán model has many advantages over the other models (Landau, Vavilov):

— it is fast,
— it describes the energy loss distribution rather well and
— by approaching the limit of the validity of the Landau theory, approaches smoothly the Landau distribution.

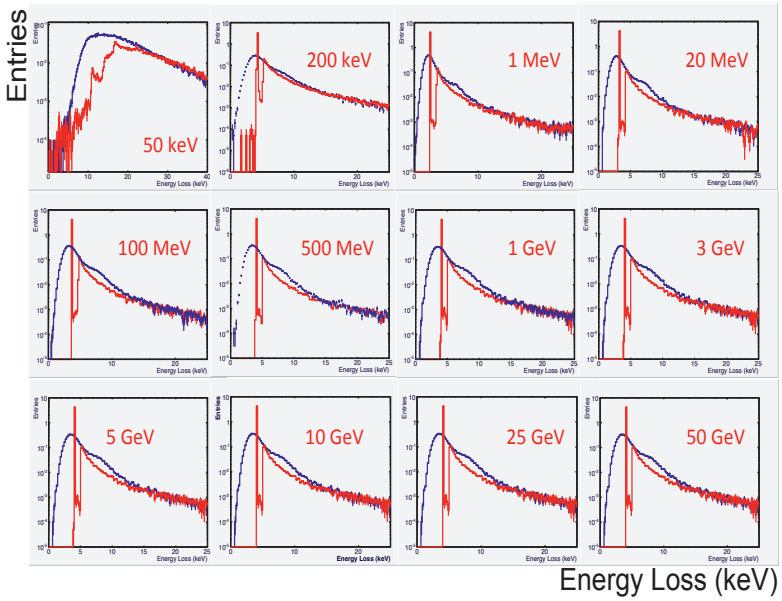

Figure 3.19: *Ionization energy loss fluctuations for various incident electron energies in a 15 mm thin gas layer filled with 80% Ar and 20% CO_2. The results concern the EM Standard model. Fluctuations activated (blue) and de-activated (red).*

All the changes in the fluctuation model since the first version are mathematical/technical modifications. They have been made in order to get a more precise value of the most probable energy loss or a better estimation of the width (FWHM) of the minimum ionizing peak. All these changes were done using some Monte Carlo – data comparison. Later, they were validated running additional simulations for other parameters (energies, target thicknesses, particle types), and making comparisons with experimental data [62].

Interestingly, as Figure 3.19 shows, the shoulder is strongly dependent on the fluctuation model. More specifically, the red curves in Figure 3.19 show the simulated ionization

energy loss if no fluctuation model is taken into account. With blue color we show the same simulation results but this time with the Urbán fluctuation model being included. Obviously, when the Urbán fluctuation model is deactivated, the tail of the ionization energy loss for electrons shows no shoulder. After all the previous negative cross checks prove that the shoulder appearance is related to the Urbán fluctuation model and its calculations on the fluctuations of the ionization energy loss. The fact that the same problem appears through all our study and for various e^- incident energies strengthens the conclusion that the Urbán fluctuation model in Geant4 has to be fixed/improved.

3.6 Conclusions

We have investigated the ionization energy loss of minimum ionizing particles in thin gas layers as it has been simulated by the Geant4. Several models showed an unexpected shoulder on the high energy tail of the energy loss distribution for 500 MeV/c and 25 GeV/c incident electrons in several gas constituents. We provided a detailed validation by examining possible shoulder dependence on the electron incident energy, the gas of the detector, the thickness of the gas layer, the various physics processes and the fluctuation model included in the Geant4.

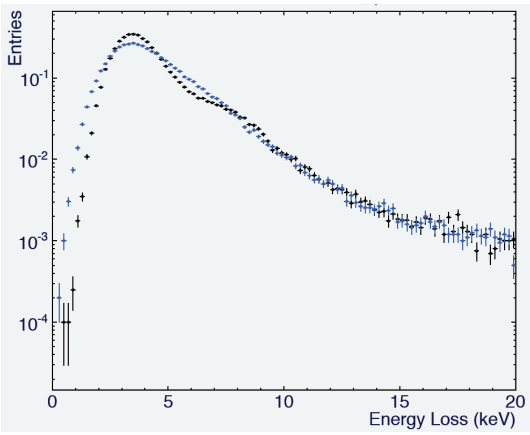

Figure 3.20: *Ionization energy loss of 500 MeV/c electrons inside a thin layer (15mm) consisting of 80% Ar and 20% CO_2 as modeled with the Standard model. The black points represent the old fluctuation model and the blue, the improved one by the most recent update.*

The origin of the shoulder was finally localized and traced to the fluctuation model implemented by the Geant4 code. The correction of the fluctuation model is important for the achieved improvement and it can be interpreted as a correction for small energy losses in one step. Thus, if the mean energy loss is smaller than 25 times the mean excitation energy (I) of the target atom, the fluctuation of this energy loss is computed

in two steps (with a mean pion energy loss per step equals the (energy loss)/2). This way the achieved smearing of the energy loss is bigger and there is no more shoulder appearance in the energy loss distribution [62].

The Geant4 fluctuation model which reproduces the ionization energy loss for charged particles in thin layers was enhanced in order to be valid for very thin gas layers and low density materials. The improved model is less dependent on range cut-offs for the secondary particles' production. The comparative analysis between the old and the updated fluctuation model for the different Geant4 physics models is given in Figures 3.20 and 3.21. Note that the fluctuation model applies to all the EM physics models in Geant4 and its correction improves all the different physics models (Standard, Livermore and Penelope).

Although Geant4 remains a powerful tool in detector response simulation its use in the lower energy regime should be with care. It is worth noticing here that this correction to the fluctuation model may have a significant impact for simulations also in LHC experiments.

The updated fluctuation model is therefore recommended for detector simulations, especially for thin targets or thin surface gas detectors where the minimum energy deposition is of interest. Figure 3.21 shows the improvement of the fluctuation model for argon, carbon, hydrogen, neon, oxygen and xenon using the Standard model.

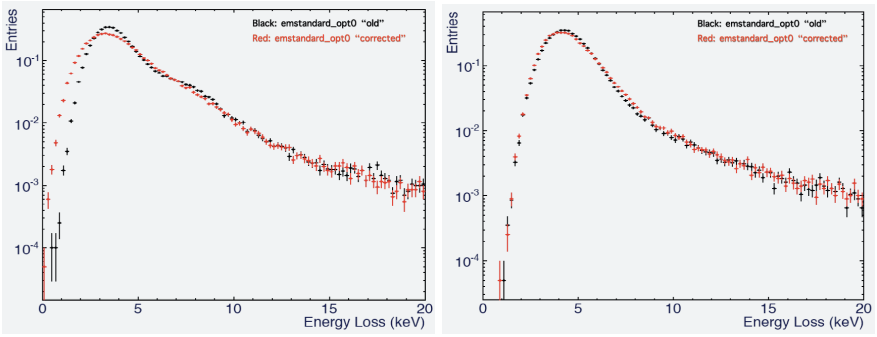

(a) Argon (b) Carbon

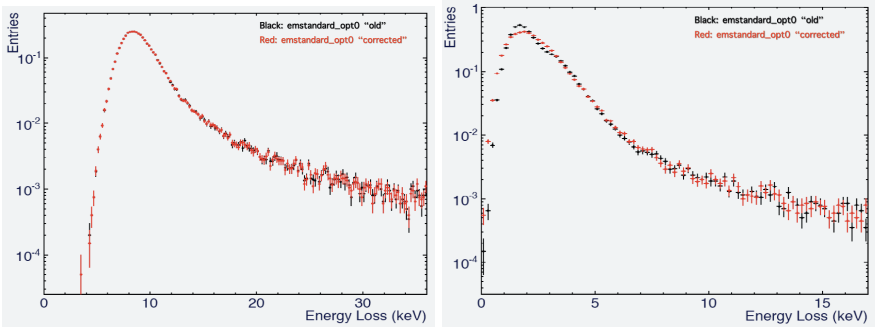

(c) Hydrogen (d) Neon

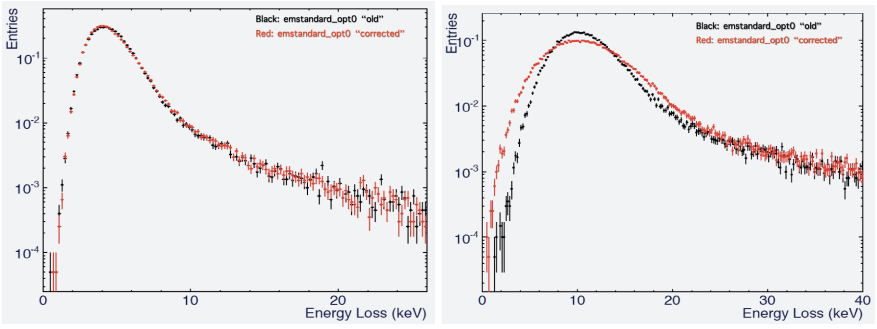

(e) Oxygen (f) Xenon

Figure 3.21: *Simulated ionization energy loss for 500 MeV/c electrons using the Standard model in 15 mm gas layer filled with (a) Argon (ρ=1.782 mg/cm^3), (b) Carbon (ρ=1.799 mg/cm^3), (c) Hydrogen (ρ=1.799 mg/cm^3), (d) Neon (ρ=0.899 mg/cm^3), (e) Oxygen (ρ=1.79 mg/cm^3) and (e) Xenon (ρ=5.458 mg/cm^3).*

CHAPTER 4

NEUTRON PHYSICS

Outlook

This work focuses exclusively on neutron simulation and the behavior of neutron cross-sections in the Geant4 tool. For this purpose, we had to extract the neutron cross sections from Geant4 and run a comparative analysis. As a benchmark, we had to use several neutron databases which provided us with measured cross-sections including old as well as most recent data sets. As a result of this work, Geant4's neutron data are updated improving thus Geant's performance and reliability on neutron simulation for all LHC experiments.

Sections 4.1 and 4.2 explain the importance of neutrons in the LHC environment and summarize their interactions with matter. Section 4.3 describes how Geant4 models neutron interactions while 4.4 gives an introduction to the physics processes as applied by the Geant4. In section 4.5 we discuss the evaluated data libraries and the method followed to extract the neutron cross-sections. Finally, Section 4.6 presents the comparison and concludes by showing the updated Geant4 results.

4.1 LHC - neutron environment

Whilst neutron detection and measurement is an important task, this work emphasizes the modeling of neutrons as a background field, aiming to understand the performance of the current detectors and design future ones.

The most common source of neutrons in the LHC are hadrons – mostly pions – produced from beam-beam collisions. These hadrons excite nuclei of the detector medium. The following de-excitation results in the production of neutrons. In fact, per GeV absorbed hadron energy, about five neutrons are liberated with kinetic energy of a few MeV. While the neutron production is simulated by Geant4, its simulation will not concern us in this work.

With a mean energy of about 8 GeV and an integrated flux of about $10^{12}\pi^{\pm}/\mathrm{cm}^2/\mathrm{yr}$, at a distance of 1 m (distance from crossing point) [77], the derived neutron kinetic

energy is about 10 – 20 MeV and the neutron flux at ∼1 m is about $4{\cdot}10^{13}$ n/cm^2/yr. Neutrons can also be produced by the interaction of the accelerator beams either with the beam pipes or the bending magnets, the focusing quadrupoles, etc. This explains the interest in neutrons, which is after all a strong background field in LHC experiments [103].

The thermalization time of ∼10 MeV neutrons is about 1 ms, according to the findings of the TARC experiment [96], where neutrons were produced by few GeV protons in a beam dump and were thermalized by multiple elastic scatterings in Pb. The LHC detectors such as ATLAS consist of lighter elements reducing the thermalization time (due to the 1/A dependence of the energy loss), but it still remains slow compared to the 25 ns time interval between two beam crossings, so that at experiments such as ATLAS a kind of neutron gas remains. Once the neutrons have thermalized, they are absorbed very fast by the detector material: neutrons disappear after 1 ms, very much shorter than their lifetime (900 sec).

Neutron-nucleus resonances play an important role in neutron interactions. As neutrons slow down via interaction with matter they cross resonance energies where the cross-sections increase by several orders of magnitude (figure 4.3). An accurate simulation of neutron interactions thus needs a precise knowledge of all these resonances. The resonance spectra are difficult to predict and in practice we rely on measured spectra.

The possible interaction processes of neutrons with the detector material and their impact via the resulting reaction products is important. For example, one should be cautious with gas constituents such as hydrogen in order to avoid recoil protons, as well as the n+p→d+γ interaction emitting energetic photons. Also, the dynamical behavior of the much heavier recoiling noble gas atoms can result in an extreme ionization, triggering spark. Correct modeling of neutron interactions is also important for the choice of shielding to reduce the ubiquitous neutron field.

Neutron and other hadronic interactions in detectors result in crystal defects known as non-ionizing energy loss (NIEL). These can reduce detector performance (energy resolution, efficiency, etc) in solid state detectors such as silicon trackers or crystal calorimeters. For this reason radiation robust detector components are needed. A good simulation can help to choose the appropriate elemental composition of future detector materials in order to reduce (but not eliminate) the neutron flux.

4.2 Interaction with matter

Neutrons that transverse a thin layer of material can pass through without interacting, or can have interactions that change their direction and energy, or they may fail to emerge from the material [104]. The probability of an interaction to occur is related to the cross-section σ. The cross-section has the dimensions of area and its main unit is the barn (1 barn = 10^{-24} cm^2).

Most neutron-nucleus scatterings proceed via a compound nucleus. The scattering can be elastic or inelastic. Neutron elastic scattering can occur by the collision of an incident neutron and a nucleus. After the collision the neutron rebounds with a lower

speed than its initial. The recoiling nucleus gains kinetic energy during the scattered process, which is measurable. After the collision, the nucleus returns to its ground state and no other particles are produced. Figure 4.2 shows the neutron elastic cross-sections for scattering off argon. In an elastic scattering off a nucleus with mass number A the ratio between the final and the initial neutron energy is

$$\frac{E'}{E} = \frac{A^2 + 1 + 2Acos\theta}{(A+1)^2} \tag{4.1}$$

where θ is the scattering angle in the center-of-mass system. For θ=0 (no scattering) E'=E and for θ=180° (head-on collision)

$$(\frac{E'}{E})_{min} = (\frac{A-1}{A+1})^2 \tag{4.2}$$

Therefore, light nuclei are more efficient for elastic neutron energy degradation with significant energy fraction given as kinetic energy to the recoiling nucleus. In inelastic scattering the total energy of the outgoing scattering particles is less than their initial energy. The lost energy is carried by either new particles (p, n) or by exciting internal degrees of freedom of the scattering particles. Typical neutron inelastic reactions are of the type z(n,p)z′ (charge exchange).

If the nucleus have no initial kinetic energy, the neutron must have bigger kinetic energy than the excitation energy, in order to react. For this reason, the inelastic scattering is known as a threshold reaction (minimum kinetic energy of the neutron required). The excited nucleus de-excites by emitting gamma radiation.

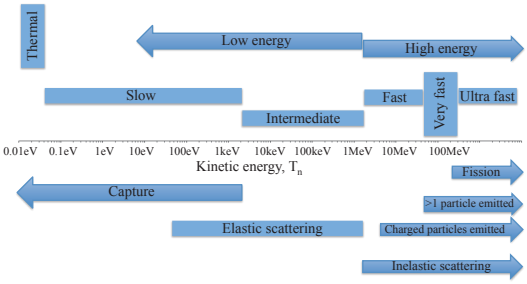

Figure 4.1: *Classification of neutrons (above the scale) according to their kinetic energy, and summary of the most important interactions at different energies (below the scale).*

Inelastic collisions generally have a threshold energy below which the reaction is kinematically suppressed. Above this, there is enough energy to excite the nucleus so that it produces extra particles (α, p, γ, etc.). Hence inelastic interactions are most important

for fast neutrons. However some interactions are exothermic, e.g. fission, producing a lower mass nucleus. Slow neutrons can also give rise to such inelastic interactions.

Though the probability of the inelastic scattering is lower than the elastic, the neutron energy loss is higher in an inelastic collision. The secondary particles produced in inelastic collisions are important in radiation damage of detector components and in generating background signals in detectors.

In the elastic scattering z(n,n)z, the nucleus actually carries kinetic energy and momentum. However, during inelastic scattering z(n,p)z′, a significant part of the kinetic energy of the neutrons is lost into intrinsic degrees of freedom of the recoiling nucleus.

There are four different types of neutrons based on their kinetic energy:

— *Fast neutrons*: typically with energies above 1 MeV. Depending on their energy, they can be split in "Fast", "Very fast" and "Ultra fast". These neutrons are usually produced in nuclear reactions. During such processes, they gain in addition some kinetic energy above the binding energy of about 7 – 8 MeV per nucleon. ,

— *Intermediate neutrons*: with energies between 0.4 eV and 1 MeV,

— *Slow neutrons*: with energies below ∼2 meV. Additionally, there are "very cold" neutrons (0.3 μeV $\leq$ E$_n$ $<$ 50 μeV) and "ultra cold" neutrons (E$_n$ $<$ 300 neV). and

— *Thermal neutrons*: with very low kinetic energies of about 25 meV at room temperature

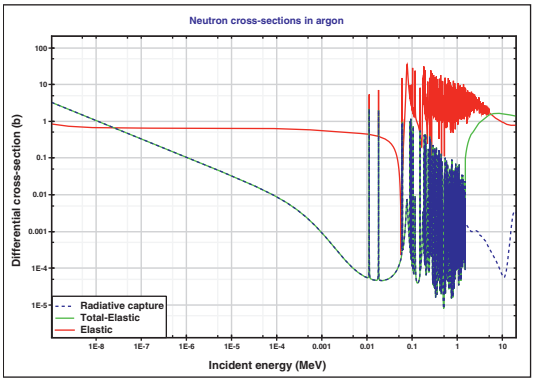

Figure 4.2: *Neutron cross-sections in argon. Elastic scattering is dominant in the range 10^{-3} –10 MeV which coincides with the LHC neutron field. The green color (Total – Elastic) represents the cross-sections for a non-elastic interaction (we have subtracted the elastic cross-sections from the total ones).*

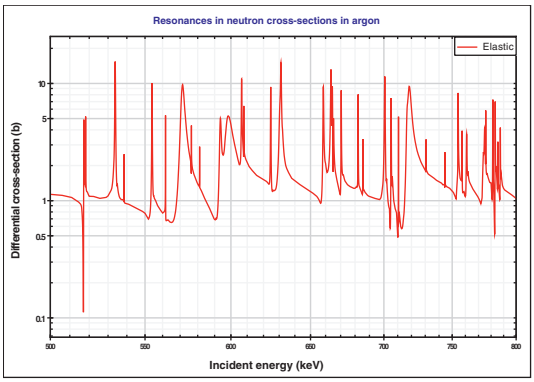

Figure 4.3: *Elastic neutron cross-sections in argon (zoom-in of figure 4.2). These dominant resonances correspond to excited nuclear states. The resonances are grouped tightly together with widths less than 1 eV.*

In radiative capture the incident neutron is absorbed by the nucleus (A), forming a heavier nucleus ($A+1$). A neutron can penetrate a nucleus easier than a proton since it does not have to overcome the Coulomb potential barrier. The compound nucleus then decays to its ground state and emits gammas [105]. In fission the incident neutron is absorbed by heavy nucleus (e.g. uranium), which then splits into two or more smaller nuclei, called the fission fragments. In parallel, gamma rays and neutrons can also be emitted. The fission fragments often decay by beta and/or gamma radiation and neutron emission.

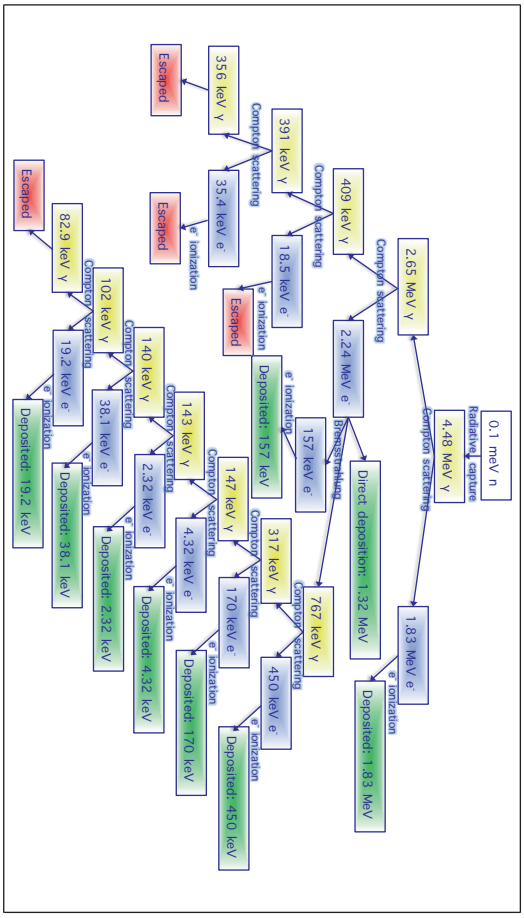

Figure 4.4: *Geant4 single event of 0.1 meV neutron on natural argon.*

4.3 Nuclear data in the Geant4 code

Geant4 models production of neutrons in hadronic interaction, transport of those neutrons through the detector, and their interactions with the material of the detector. The interactions are modeled via Physics models; these models use cross-sections for the various interactions described above which are calculated from the Geant4 Neutron Data Libraries (G4NDL). The values in G4NDL [106] are based on available published compilations of neutron cross-sections, known as Evaluated Nuclear Data Libraries.

We investigate G4NDL Version 3.13, which was available in Geant4 release 9.2 September 2010. These cross-sections were based on evaluations made in the late 1990s, with some updates during the last 10 years. This investigation was motivated by the following:

— the last updates in G4NDL version 3.13 were not documented, and so the data source is unknown,
— data for several important isotopes are missing,
— the data format is not documented making it difficult to investigate directly and
— there are published tools to process the Evaluated NDL data into G4NDL versions.

In this work we have used Geant4 to produce plots of the neutron cross-sections it derives from G4NDL. We compare these to various Evaluated NDL data sets, allowing us to identify the origin of the G4NDL data. Since the origin-data is outdated and significantly different to modern Evaluated NDL sets, the Geant4 group have updated the G4NDL. In the next sections we give more details on G4NDL and how Geant4 models the physics of particle interactions. We also describe various models available, concluding that for this study we should use the QGSP BERT HP physics model. In addition, we explain how the cross-sections are extracted in Geant4. We then discuss the Evaluated NDLs and summarize how we extract cross-sections for comparisons with Geant4 values. The comparison and analysis show that the more recent version of G4NDL (version 4.0) uses the more up-to-date data sets.

4.3.1 G4NDL: The Geant4 Neutron Data Library

G4NDL contains neutron cross-sections as functions of energy for different isotopes and different physics processes [106]. The Geant4 Neutron Data Library covers neutron interactions from thermal energies up to 20 MeV. This limitation is fixed by the Evaluated Nuclear Data Libraries. In this work we have tested the G4NDL 3.13 version, available in Geant4 9.4 release.

G4NDL includes neutron cross-sections, angular distributions and final state information. However, as we will see later, the library is not complete because either there are no data for several elements or the existing data are not up to date. The G4NDL format is from the one of the Evaluated Nuclear Data Libraries, therefore the combination of the data from these libraries into Geant4 format is not an easy task. Most of the neutron cross-section data are derived from the ENDF/B-VI.8 evaluated data library. The ENDF/B-VI.8 library has been processed, in order to explicitly include all neutron

nuclear resonances [107].

4.3.2 Geant4 Physics Lists, Particles, Processes and Models

A Geant4 Physics List includes a list of all particles to be considered, a list of physics processes that can occur as well as production thresholds needed for an application. Only particles in this list will be tracked through the detector, and they can only undergo interactions, reach final states, etc., contained in the process(es) to which are assigned.

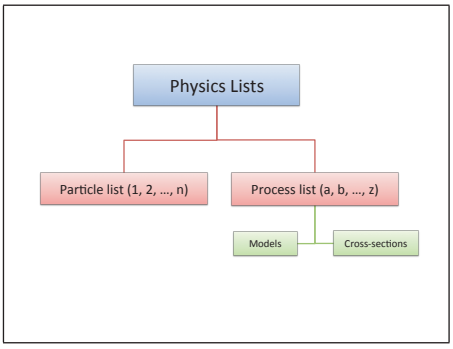

Figure 4.5: *Physics list contents in Geant4. Each Physics list contains a list of particles and processes. A particle can be assigned to more than one process, e.g. an electron can undergo a multiple scattering and bremsstrahlung.*

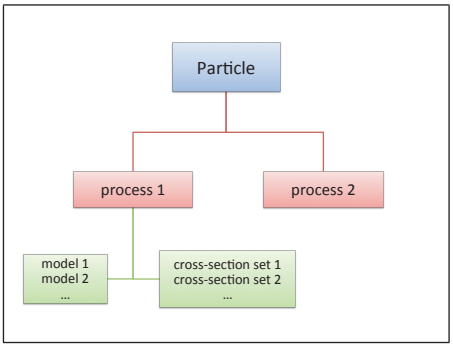

Figure 4.6: *Each particle is assigned to a process. The process holds two sets of information; the cross-sections (which give the probability of each process to occur) and the models (which generate the final state of each process).*

A particle has its intrinsic properties (mass, charge, etc.) and a list of processes that it undergoes while traveling through the detector medium (Figure 4.6). This list is a

subset of those in the Physics List (Figure 4.5). Many particles can undergo a particular process, e.g. all charged particles can include a multiple scattering process.

Processes (Figure 4.7) describe the various interactions that particles can undergo in the detector medium (e.g. elastic scattering), and their decays if they are unstable. Transportation (e.g. charged particle motion in a magnetic field) is also treated as a process. Most processes have two basic types of information: cross-sections from which the probability of when and where something will happen can be calculated; and Models, which generate the final state of the interaction, describe what new particles are created and calculate the four-momenta of all the outgoing particles(Figure 4.8). A process can have several "cross-section–model" pairs, for example to cover different energy ranges.

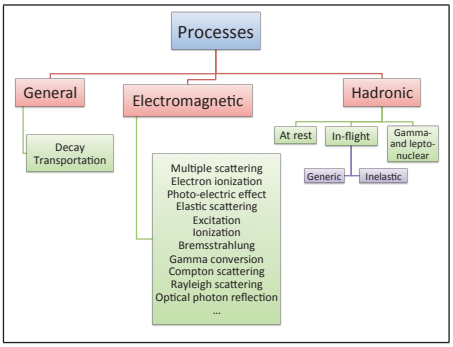

Figure 4.7: *General, electromagnetic and hadronic are the three types of processes in the Geant4 code. Each of these processes can be modeled with the use of different approaches/models (Figure 4.8).*

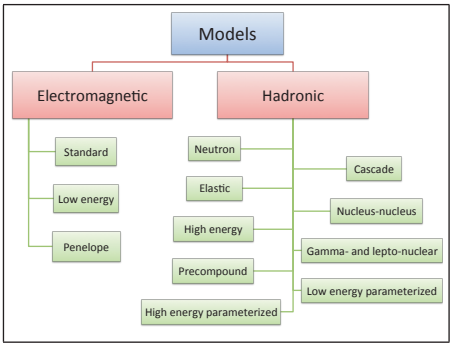

Figure 4.8: *A model (electromagnetic or hadronic) generates the final state of a process. Different models use different approaches of modeling.*

A physics list can be built in three different ways: either by the use of ready physics lists provided by Geant4 (also known as reference physics lists, e.g. QGSP), or by a

user-made combination of physics processes, or by the use of physics constructors. For some of the physics lists, many variants exist (QGSP, QGSP BERT, QGSP BIC, etc.). The user can combine any of the high, intermediate and low energy models shown in Figure 4.9, in order to create a physics list.

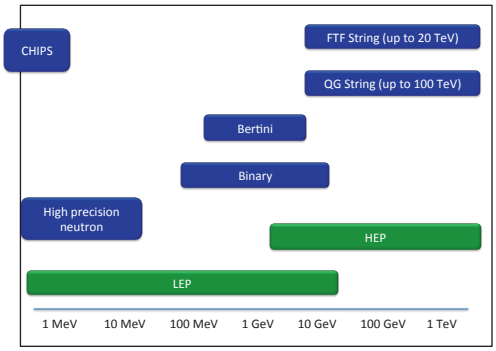

Figure 4.9: *Geant4 models and their energy range validity in terms of particle's incident energy.*

High energy models

QGS: the Quark Gluon String model applies the interaction modeling for protons, neutrons, pions and kaons above ∼12 GeV [97].
FTF: the Fritjof model [79] is used for the de-excitation of the nucleus. This model is valid for incident energies above ∼4 GeV and is used for the final-state model of all hadrons.
HEP: the High Energy Parametrization model is based on a parametrized modeling for pion-, kaon-, proton- and neutron-nucleus inelastic interactions above 25 GeV.

Intermediate energy

Bertini cascade: The Bertini model simulates the intra-nuclear cascade and it is mainly intended for incident energies below ∼9 GeV [107]. In this model incident hadrons collide with protons and neutrons producing secondary particles. The latter collide in turn with other nucleons. At the end of this cascade process the excited nucleus is producing additional secondary neutrons and protons. This detailed process makes Bertini model more precise than the Binary cascade [80].
Binary cascade: The propagation of an incident hadron through the nucleus as well as the propagation of its produced secondaries are modeled by a cascading series of two-particle collisions [108] based on the particle's total cross-section. This model is

mostly used in the energy region below 10 GeV. It is also used for the re-scattering of secondary particles produced by the Quark Gluon String model [81].

Low energy

LEP: the Low Energy Parametrization model is based on a parametrized modeling for pion-, kaon-, proton- and neutron-nucleus inelastic interactions below ∼55 GeV [78].
CHIPS: the Chiral Invariant Phase Space Decay model is a three dimensional event generator at the quark-level for the fragmentation of excited hadronic systems in to hadrons [82].
High precision neutrons: Below 20 MeV incident energy, the Geant4 tool provides the high precision neutron model (Neutron HP) for the treatment of low-energy neutron interactions. Neutron HP is a data driven model and depends on the G4NDL for neutron cross-sections.

4.4 Physics Lists

In this work we focus on the QGSP BERT HP physics which is the combination of the QGSP BERT model and High Precision model.

QGSP BERT: is the physics list most recommended for HEP and is used in the ATLAS experiment. It combines Standard EM processed and used Bertini for hadron energies below ∼10 GeV and the QGS model for energies above 20 GeV. For high energy hadrons the model uses the Bertini intra-nuclear model followed by nucleus de-excitation (BERT) below 9.9 GeV [97]. Between 9.5 GeV and 25 GeV it uses the LEP model and for energies above 12 GeV uses the Quark-Gluon-String model (QGS) followed by Precompound and evaporation models for the nucleus de-excitation (QGSP).
QGSP BERT HP: This model is similar to the QGSP BERT model. It makes use of the High Precision neutron package known as Neutron HP for transporting neutrons with kinetic energies below 20 MeV. It is significantly slower than QGSP BERT when thermal cross-sections are used. QGSP BERT HP can be also used for radiation protection and shielding applications [97].

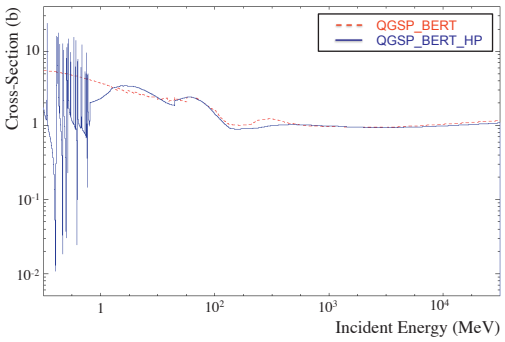

Figure 4.10: *Total cross-section data for neutrons off Ar using QGSP BERT (dotted red line) and QGSP BERT HP (solid blue line). As was expected the QGSP BERT physics list is lacking the low energy neutron data and therefore is not reliable for a complete neutron simulation.*

4.4.1 Neutron cross-sections

Cross-sections are used for the calculation of the interaction length [98]. The Geant4 class G4CrossSectionDataStore contains combinations of data and processes for a variety of ionizing particles and detector materials [98]. In order to extract the Geant4 cross-sections, we used the extended hadronic example of Geant4, Hadr00. Hadr00, is an example of the Geant4 code made for testing and validation. It demonstrates the usage of G4HadronicProcessStore to access cross-sections. By default elements are chosen from the Geant4 NIST database while the natural isotope composition is assumed. Hadr00 provides cross-section histograms as a function of the neutron incident energy. With a ROOT script we converted the decimal logarithmic scale into a linear scale (MeV). As we will see later, the data from the evaluated nuclear data were in the same linear format making thus the comparison possible.

In order to avoid technical problems, in this work and for the comparison between the Geant4 and the data libraries we use the concept of the non-elastic cross-section. We calculated the sum of the inelastic and the radiative capture cross-sections which gives us the non-elastic cross-sections.

$$\frac{d\sigma_{(non-elastic)}}{dE_n} = \frac{d\sigma_{(inelastic)}}{dE_n} + \frac{d\sigma_{(capture)}}{dE_n} \tag{4.3}$$

4.5 Evaluated Nuclear Reaction Data

Nuclear evaluated data are produced through comparisons and renormalization between experimental and theoretical data. Such combined libraries consist of individual data

sets for several isotopes and elements and find large applications technological and nuclear applications. Each material in the libraries is subcategorized by type of data (e.g. cross-sections, energy distributions, etc.) and/or by reactions type (e.g. inelastic/elastic reaction cross-sections) [83].
There are currently three main groups producing evaluated nuclear data;

1. the Cross Section Evaluation Working Group (CSEWG) of the United States (ENDF/B libraries) [84],
2. the international collaboration of Data Bank member countries co-ordinated under the NEA Data Bank (Joint Evaluated Fission and Fusion File – JEFF) [85] and
3. the Japanese Nuclear Data Committee (Japanese Evaluated Nuclear Data Library – JENDL) [86].

In this work and in order to validate the Geant4 code, we used the nuclear information software JANIS (Java-based nuclear information software) [83]. JANIS is a display program which gives access to nuclear data. JANIS uses NEA database as the default database. It contains experimental and evaluated nuclear reaction data. All major evaluated data libraries are available in JANIS.

The ENDF/B-VII.0 [88] contains a considerable amount of neutron cross-sections. These cross-sections were obtained by complex and well established evaluation process which start from measured microscopic cross-sections and, at energies above neutron resonances, are supplemented by nuclear reaction model calculations. The resulting cross-sections are tested against experimental data which in general, are more precise than the microscopic cross-sections.

Each evaluation represents a collection of every possible neutron reaction on a single nucleus, of a particular isotope, for neutrons with energies ranging from $1e^{-5}$ eV up to 20 MeV. Each reaction contains the reaction cross-section and the outgoing probability tables for nearly every particle that can be emitted in the reaction. This is a lot of data for each evaluation and the modeling and data fitting are time consuming. Experiments were carried out at an accelerator at Rensselaer Polytechnic Institute [87].

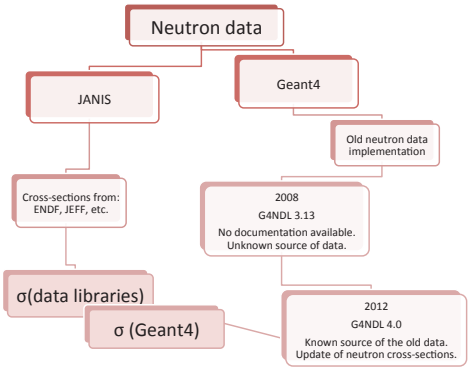

Figure 4.11: *Cross-sections extracted and compared from JANIS and Geant4.*

4.5.1 Overview of the Neutron Data Libraries

We describe here some of the evaluated data libraries relevant to Geant4. The latest release – ENDF/B-VII.0 library [88], released in December 2006, was extensively tested and improved over its previous version ENDF/B-VI.8 [89]. In general ENDF/B-VII.0 represents considerable update and improvement over ENDF/B-VI.8 as it includes more elements. ENDF provides very limited error information for few elements, but not for the ones presented in this work.

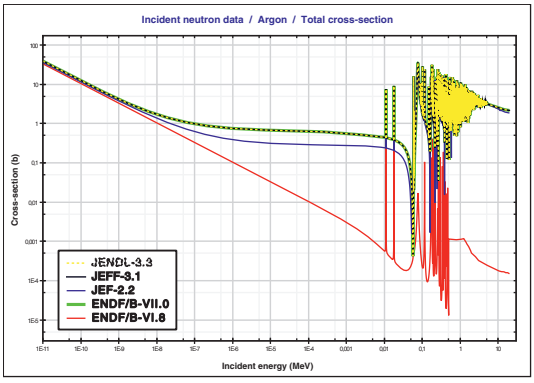

Figure 4.12: *A comparison of the neutron total cross-section for argon from five different evaluated nuclear data libraries.*

The international collaboration of Data Bank member countries co-ordinated under the NEA Data Bank has produced the Joint Evaluated Fission and Fusion File (JEFF) [90]. All JEFF sets are in the same format as the ENDF sets. JEF was introduced in 1985,

and was followed by its improved version (JEF-2.2 [90]) in 1993. JEFF-3.0 [91] library which was released in 2002 superseded JEF-2.2.

The JEFF-3.0A [92] (Joint Evaluated Fission and Fusion File including the Neutron Activation File) library enhances the JEFF-3.0, adding neutron activation data and doubles the number of target nuclei. The most update JEFF set is the JEFF-3.1 which was released in May 2005 [93]. The radioactive decay data library contains data for 3852 isotopes, of which 226 are stable.

The Japanese have also produced a nuclear data library in order to standardize Japanese calculations for thermal reactors, fusion and shielding calculations. The most recent version is the JENDL-3.3 (Japanese Evaluated Nuclear Data Library) released in 2002. JENDL is also in ENDF-6 format [94].

Table 4.1: *Summary of several evaluated data sets, from which the plots of cross-sections presented in this work have been produced.*

Neutron Data Libraries						
Library	Version	Year	# of materials	# of elements	Thermal scattering # of nuclei	Activation # of materials
ENDF/B	VII.0	2006	393	3	20	-
	VI.8	2001	329	16	15	-
JEF(F)	3.1	2005	381	7	9	-
	2.2	1992	313	14	5	-
	3.0/A	2005	774	-	-	774
JENDL	3.3	2002	337	2	-	-

4.5.2 Cross-sections

In order to obtain a correct comparison between Geant4 code and the data, we have used the non-elastic scattering. As Section 4.5.2 explains, the definition of inelastic scattering is different between the Geant4 code and the data libraries. For the purposes of this work the non-elastic scattering is a common term between the Geant4 and the evaluated data libraries.

The cross-section data cover a neutron energy range up to 20 MeV, starting at 10^{-5} eV or the lower limit of the reaction threshold if higher. For other reactions, the cross-section should start at the reaction threshold energy and should continue up to a common upper energy limit. The data are separated in *files* and *sections*. The following table gives a very brief overview of MT numbers and how these are defined for each neutron interaction.

Table 4.2: *Definition of MT numbers in Evaluated NDL [83].*

Neutron Reactions	
MT Number	Neutron reaction
1	z(n,all) Neutron total cross-section
2	z(n,n′)z Elastic cross-section
3	z(n,non-elastic) Nonelastic neutron cross-section Sum of inelastic scattering, (n,2n), (n,γ), (n,p), (n,α), ...
4	Total inelastic cross-section Sum of MT=50-91
5	(z,anything) The sum of cross-sections for all reactions not covered by any other MT number
10	(z,continuum) Total continuum cross-section Includes all continuum reactions and excludes all
16	(z,2n) Cross-section for producing two neutrons and a residual nucleus
17	(z,3n) Cross-section for producing three neutrons and a residual nucleus
22	(z,nα) The cross-section for the production of a neutron and alpha particles plus a residual nucleus
33	(z,nt) Cross-section for the production of one neutron and one triton plus a residual nucleus
50	z(n,n′)z^* The cross-section for neutron production, with the residual nucleus left in the ground state
51	z(n,n′)z*,1 Inelastic cross-section to the first excited level
90	z(n,n′)z*,40 Inelastic cross-section to the fortieth excited level
102	z(n,γ)z′ Radiative capture cross-section
... 999 MT numbers	

Files (MF): are subdivisions of isotopes and elements; each file represents different data. For example, MF=3 refers to reaction cross-sections data, MF=4 to angular distributions, etc. MF values are between 1 to 99.
Sections (MT): are subcategories of a File (MF); each section refers to a certain reaction or data (e.g., MT=102 represents capture data). MT takes values between 1 and 999 [83].

The difficulty in the comparison of Geant4 code and the neutron data libraries was the correspondence of the data. More specifically, the definition of the "inelastic scattering" term was different between the Geant4 code and the data libraries. As figure 4.13 shows, the "total inelastic" cross-section in data libraries (MT=4) is incomplete since it contains only the cross-sections of the interactions with one neutron in the final state and the residual nucleus left in the first, ...fortieth level but not e.g. the cross-section for the inelastic process. This means that the term "total inelastic cross-section" does

not correspond to what one would consider as non-elastic.

For this reason, in this work we make a comparison between elastic cross-sections and non-elastic cross-sections without entering in details at the "inelastic" part. Most of the evaluated nuclear data libraries contain ready-calculated data for non-elastic cross-sections (MT=3). However, for the elements tested in this work such information was not available. In order to solve this technical problem, we subtracted the elastic cross-section (MT=2) from the total cross-section (MT=1) resulting thus to the non-elastic cross-sections (Equation 4.4). The difference between the terms "total inelastic" (solid red line) and "non-elastic" (dotted blue line) is shown in figure 4.13.

$$\frac{d\sigma_{(non-elastic)}}{dE_n} = \frac{d\sigma_{(total)}}{dE_n} - \frac{d\sigma_{(elastic)}}{dE_n} \tag{4.4}$$

This way we are sure that both the Geant4 code and the data libraries are referring to the same cross-sections. In some element cases (not in the case of argon that is shown) the non-elastic cross-sections (MT=3) are available. For these cases we just used the data directly without subtraction.

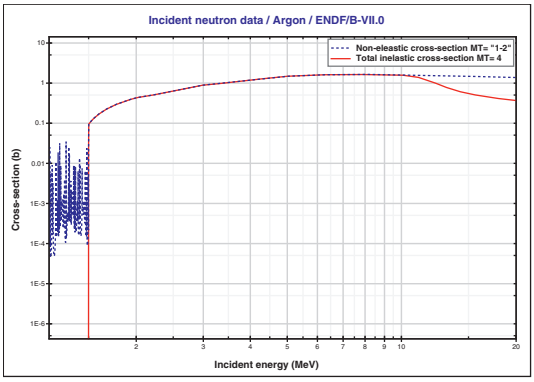

Figure 4.13: *Non-elastic and "total inelastic" cross-sections as defined by ENDF/B-VII.0. The difference between the terms "total inelastic" (solid red line) and "non-elastic" (dotted blue line) shows the lack of data in MT=4. The disagreement is obvious above ∼10 MeV due to the threshold of the inelastic reactions.*

As we mentioned earlier, in this work we used the nuclear information software JANIS to access nuclear data. JANIS uses NEA database as the default database and it contains all major evaluated data libraries. JANIS takes as an input the incident particle (e.g. incident neutron data), the data library we want to access (e.g. ENDF/B-VII.0) and then for the kind of data we need (e.g. cross-section), the periodic element we study (e.g. argon). The result is provided in two different formats; either as a histogram or as data points (text file). Using the TBrowser class of ROOT we can browse all ROOT objects (Geant4 and JANIS data) and plot them together.

4.6 Geant4 neutron cross-sections vs Nuclear Evaluated Data

4.6.1 Natural elements

The following figures (4.14 to 4.20) show a comparison between G4NDL and data taken from various widely used evaluated neutron data libraries. The data cover the range of interest (for LHC type experiments) from few keV up to about 20 MeV kinetic energy. We refer here to noble gases like argon, xenon, helium, krypton, and other active fillings like hydrogen, oxygen and carbon.

In the data libraries the data are separated by isotopes. For every element presented in this work, we assume the natural composition e.g. for argon: 0.337% ^{36}Ar + 0.063% ^{38}Ar + 99.6% ^{40}Ar and sum the cross-sections weighted by these fractions. For the Geant4 we derived the elements from the NIST database of elements and isotope compositions. For example for the case of argon we used the material G4Ar. As we will see later in this work, we could not sum the weighted cross-sections for each isotope in order to get the natural argon cross-sections due to the lack of isotope data in G4NDL.

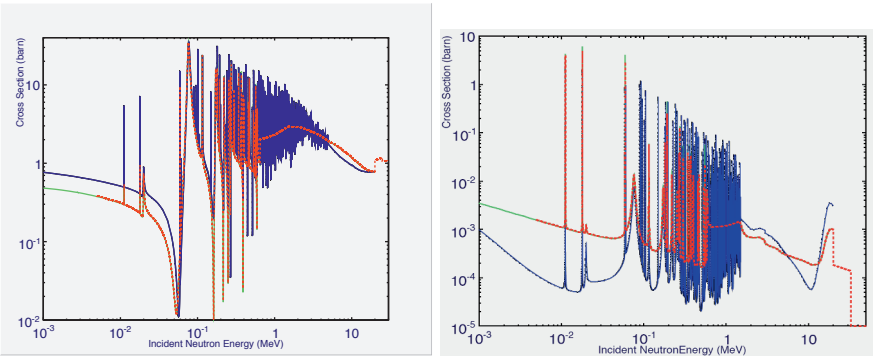

(a) Elastic cross-section for argon.

(b) Non-elastic cross-section for argon.

Figure 4.14: *Argon cross-sections (a) elastic and (b) non-elastic. G4NDL (red), JEF-2.2(identical to JEFF-3.0) (green), ENDF/B-VII.0 (identical to JEFF-3.1) (blue). For energies up to ∼0.5 MeV there are not major differences. Significant differences appear in neutron non-elastic scattering. In the region below 1 MeV which corresponds in neutron radiative capture the difference between G4NDL and the recent data libraries is up to one order of magnitude.*

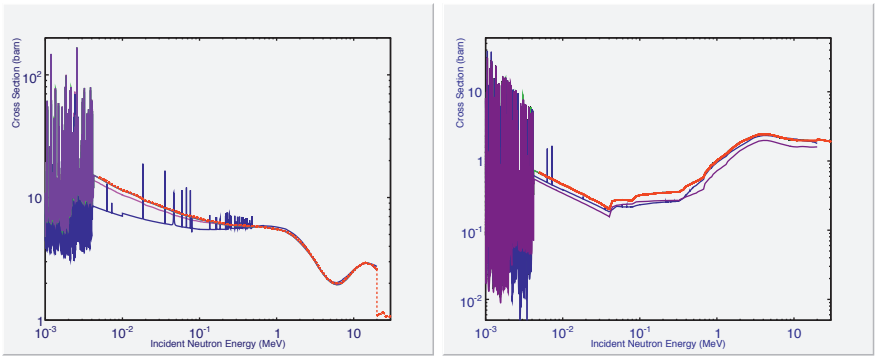

(a) Elastic cross-section for xenon. (b) Non-elastic cross-section for xenon.

Figure 4.15: *Xenon cross-sections (a) elastic and (b) non-elastic. G4NDL (red), ENDF/B-VI.8 (identical to JEFF-3.0) (purple), JEF-2.2 (identical to JENDL-3.3) (pink), ENDF/B-VII.0 (identical to JEFF-3.3) (blue).*

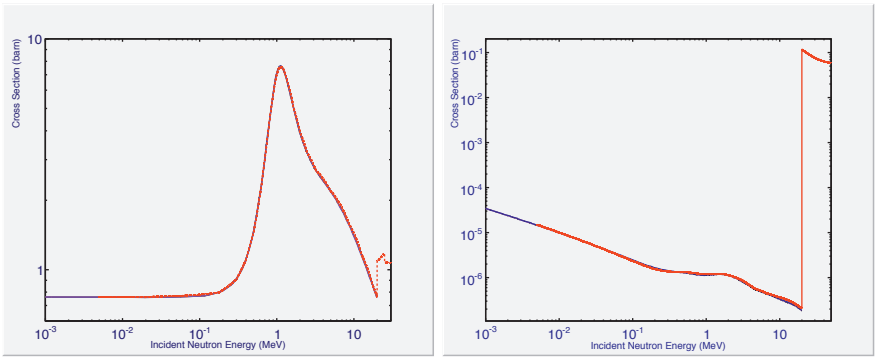

(a) Elastic cross-section for helium. (b) Non-elastic cross-section for helium.

Figure 4.16: *Helium cross-sections (a) elastic and (b) non-elastic. G4NDL (red), ENDF/B-VI.8 (identical to JEFF-3.0, ENDF/B-VII.0 and JEFF-3.1) (purple). The Geant4 step at 20 MeV is related to the different model used by Geant4 above 20 MeV (G4NDL limit) and will not concern us in this work.*

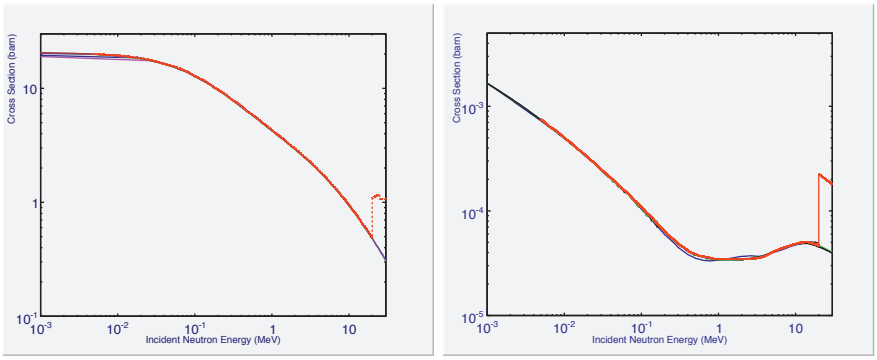

(a) Elastic cross-section for hydrogen. (b) Non-elastic cross-section for hydrogen.

Figure 4.17: *Hydrogen cross-sections (a) elastic and (b) non-elastic. G4NDL (red), ENDF/B-VI.8 (identical to JEFF-3.0) (pink), ENDF/B-VII.0 (identical to JEFF-3.1) (blue). There is good agreement between older and recent data libraries. The Geant4 step appearing at 20 MeV coincides with the fact that Geant4 above 20 MeV does not use the G4NDL but different data.*

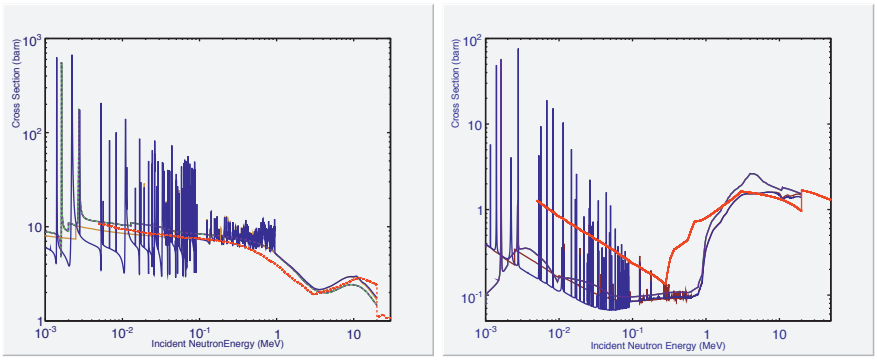

(a) Elastic cross-section for krypton. (b) Non-elastic cross-section for krypton.

Figure 4.18: *Krypton cross-sections (a) elastic and (b) non-elastic. G4NDL (red), JEFF-3.0 (identical to JEFF-3.1) (green), ENDF/B-VII.0 (blue), and JENDL-3.3 (yellow). G4NDL does not contain data for krypton. Instead the user has to take data for bromine (one less proton than krypton), plotted here, which clearly does not follow any of the libraries. Krypton data should be added to G4NDL.*

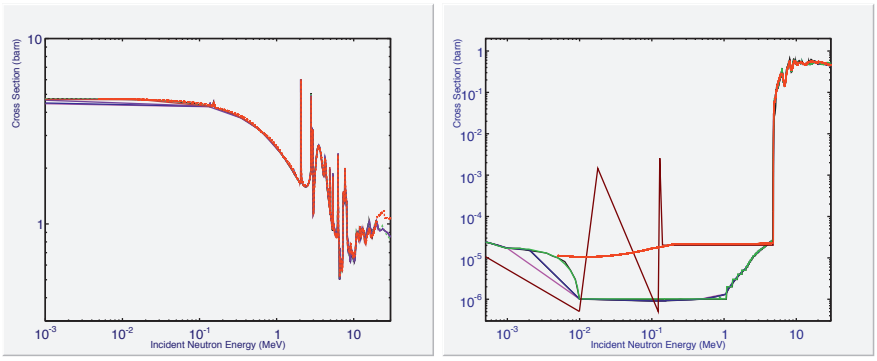

(a) Elastic cross-section for carbon. (b) Non-elastic cross-section for carbon.

Figure 4.19: *Carbon cross-sections (a) elastic and (b) non-elastic. G4NDL (red), ENDF/B-VI.8 (identical to JEFF-3.0) (green), JEF-2.2 (identical to JENDL-3.3) (pink), ENDF/B-VII.0 (blue), JEFF-3.1 (brown). For elastic cross-sections older and recent data libraries are the same and G4NDL follows them. For non-elastic, the libraries differ from each other and G4NDL seems to follow none of them. G4NDL carbon cross-sections should be updated to follow the recent library ENDF/B-VII.0 (or JEFF-3.1).*

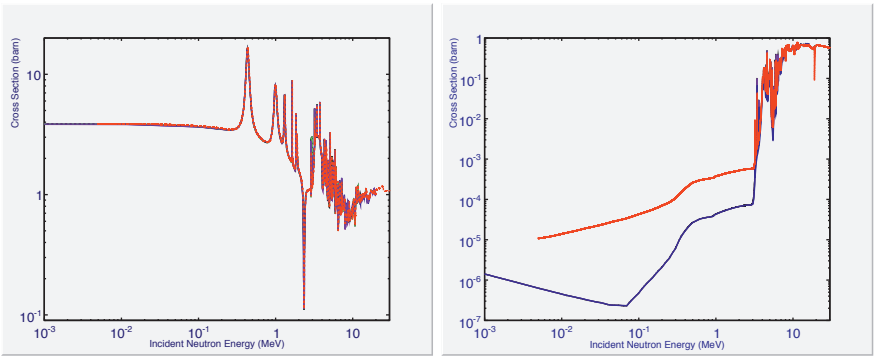

(a) Elastic cross-section for oxygen. (b) Non-elastic cross-section for oxygen.

Figure 4.20: *Oxygen cross-sections (a) elastic and (b) non-elastic. G4NDL (red), ENDF/B-VI.8 (similar to JEF-2.2, JEFF-3.0, ENDF/B-VII.0 and JEFF-3.1) (blue). G4NDL is in good agreement with all data libraries for the case of elastic scattering in oxygen. For non-elastic, all the libraries are very similar. G4NDL follows them above 3 MeV but is very different below that. G4NDL non-elastic oxygen cross-sections should be updated to follow the libraries.*

4.6.2 Isotopes

Figure 4.21 shows the cross-sections for the three stable argon isotopes ^{36}Ar, ^{38}Ar and ^{40}Ar from the ENDF/B-VII.0 Data Library. Natural argon contains 0.337% ^{36}Ar and 0.063% ^{38}Ar with the rest being ^{40}Ar. The cross-section for ^{36}Ar can be ∼100 times bigger than ^{40}Ar, so even these small impurities can make the difference.

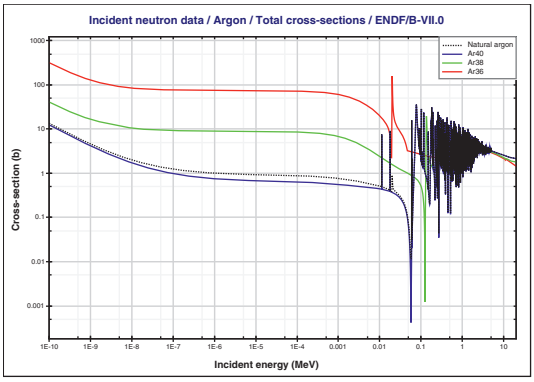

Figure 4.21: *Neutron cross-sections for argon isotopes - ENDF/B-VII.0.*

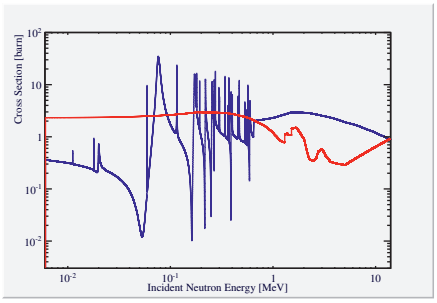

(a) Elastic cross-section for ^{40}Ar.

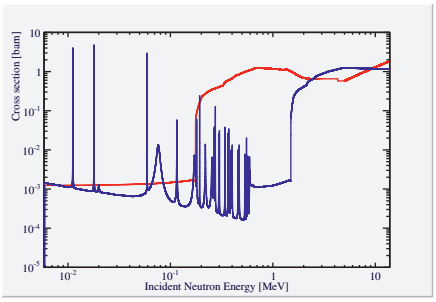

(b) Non-elastic cross-section for ^{40}Ar.

Figure 4.22: *^{40}Ar cross-section comparison. G4NDL (red), ENDF/B-VII.0 (blue). Clearly G4NDL ^{40}Ar data does not follow the recent ENDF/B-VII.0 library. It is also very different to argon data in G4NDL (material G4Ar), when compared to Figure 4.14. G4NDL should have ^{40}Ar data updated, and ^{36}Ar and ^{38}Ar added.*

The isotopes ^{36}Ar and ^{38}Ar do not exist in G4NDL, while ^{40}Ar is not accurately modeled (figure 4.22). ^{40}Ar in G4NDL should be updated. The addition of ^{36}Ar and ^{38}Ar may have benefits for users, allowing them to make new gas compositions. Consistency with G4Ar cross-sections and equality with the weighted sum of the other isotopes is also desirable.

4.6.3 Summary

We have compared G4NDL versions 3.13 cross-sections with several evaluated neutron data sets. We focused on typical elements used in gaseous detectors for HEP experiments such as helium, argon, xenon and krypton. We have also studied some main constituents of quenchers such as hydrogen, carbon and oxygen. Table 4.3 summarizes the origin of the G4NDL data; clearly it is mostly based on the older versions of JEFF evaluated neutron data sets.

The most recent evaluated nuclear data library ENDF/B-VII.0 has many improvements making it the best candidate to base a future G4NDL version on. The advances which make the recent neutron library, ENDF/B-VII.0, the best candidate for the update of G4NDL are described in details in the article [95].

Table 4.3: *The source of neutron cross-sections exist in G4NDL version 3.13. Results are given for each of the tested materials for both elastic and non-elastic interactions [83].*

Summary		
Material	Neutrons Process	G4NDL3.13
Argon	elastic	JEF-2.2, JEFF-3.0
	non-elastic	JEF-2.2, JEFF-3.0
Xenon	elastic	JEFF-3.1
	non-elastic	JEFF-3.0, ENDF/B-VI.8
Krypton	elastic	Bromine's Data
	non-elastic	Bromine's Data
Neon	elastic	No data
	non-elastic	No data
Helium	elastic	ENDF, JEFF
	non-elastic	ENDF, JEFF-3.0, JEFF-3.1
Hydrogen	elastic	ENDF, JEFF, JENDL-3.3
	non-elastic	ENDF, JEFF, JENDL-3.3
Oxygen	elastic	ENDF, JEFF
	non-elastic	ENDF, JEFF
Carbon	elastic	ENDF/B-VI.8, JEFF-3.0, JEF-2.2, JENDL-3.3
	non-elastic	ENDF/B-VI.8, JEFF-3.0, JEF-2.2 JENDL-3.3 (above 5 MeV)

The most relevant updates for particle physics detectors are:
— new and precise neutron cross-sections are available for more elements,
— new evaluations up to 150 MeV for many neutron- and proton-induced reactions,
— neutron and proton reactions with new light nucleus and
— a larger set of photonuclear reactions.
We therefore have recommended several modifications to the Geant4 maintainers.

Geant4 update

The ENDF/B-VII.0 neutron cross-sections were implemented in the version 4.0 G4NDL. The new Geant4 neutron data library has been included in the Geant4 9.5 release and contains improved data for most of the chemical constituents. The data had to be translated into the Geant4 format, in order to convert the resonance contribution into cross-section data points, and also to transform all cross-section data points into linear-linear interpolated form, which is required by the Geant4 code.

Figure 4.23 compares the old and the new G4NDL for argon, while Figure 4.24 shows the same comparison for various constituents. The data shown refer to the total neutron cross-sections and ENDF/B-VII.0 total neutron cross-sections, as well as the old G4NDL values. The new version implements the recommended new evaluated data library, and in some cases shows a big change.

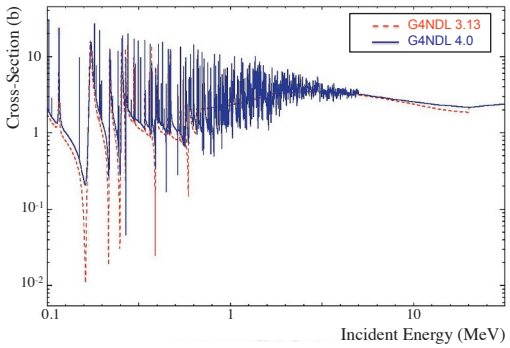

Figure 4.23: *Argon cross-sections. Comparison of old (red) and new (blue) G4NDL (ENDF/B-VII.0) total neutron cross-sections versus incident neutron energy. The latest Geant4 release (9.5) now follows the best available data.*

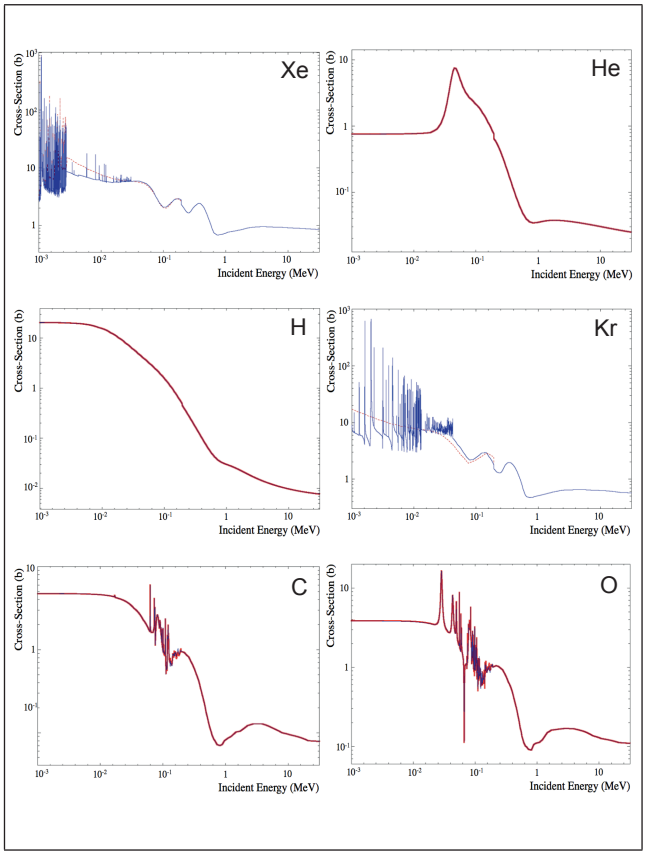

Figure 4.24: *Comparison of old (red) and new (blue) G4NDL (ENDF/B-VII.0) total neutron cross-sections versus incident neutron energy for various constituents. The latest Geant4 release (9.5) now follows the best available data.*

CHAPTER 5

MEASUREMENTS WITH THE MICROMEGAS DETECTOR

Outlook

This Chapter presents some measurements we took in Saclay with a Micromegas detector, focusing on the experimental estimation of the electron transmission. In our setup, we could change the operating conditions of the Micromegas detector. Applying few combinations of voltages to the three different layers of the Micromegas detector, i.e. the cathode, the μ-mesh and the anode, we could measure the transmission of electrons with few eV kinetic energy. Back at CERN, we compared with the simulated values obtained with the Ansys and Garfield++ codes.

In the following sections we present shortly the main properties and the working principle of a Micromegas detector. All these will also serve as an introductory to the next Chapter of this work on Gossip detector. Section 5.1 introduces the concept of the detector, its ionization and its signal production. Section 5.2 describes the InGrid technology and development. The Section 5.3 presents the comparison between the simulated and the measured electron transmission, and finally Section 5.4 concludes this Chapter.

5.1 The Micromegas working principle

Micromegas (MICROMEsh GAseous Structure) is a particle gas detector which originates from the further development of the wire chamber, which was invented in 1995 by I. Giomataris et al. [69]. Micromegas detectors are made out of light material, minimizing the interaction of passing ionizing particles. The gas volume is split into two regions; the conversion and the amplification region.

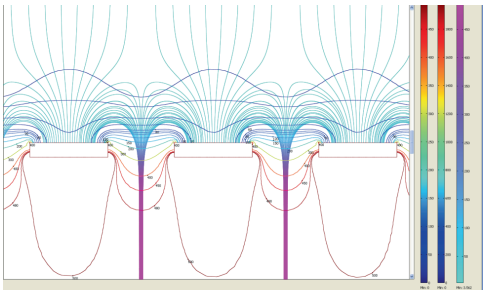

Figure 5.1: *Electric field around a high opacity micro-mesh with 250 µm avalanche gap as derived by COMSOL. On the right, the first color column gives the potential, the second refers to the strength of the electric field (V/mm) and the third one is for the electric field lines.*

In the region above the mesh, the conversion or ionization region, the electron-ion pairs are produced by the conversion of x-rays (photoelectric effect) or by the ionization along a charged particle's track. The released electrons are drifting towards the micro-mesh and amplification region. The drift field in the conversion region is fixed by the voltage set between the drift cathode and the mesh, which define the detector volume. The thickness of this region ranges from few mm to few meters in the case of a large TPC.

The liberated electrons drift towards the mesh, which they pass with a high efficiency thanks to the funnel shape of the field lines (Figure 5.1). In the following amplification region, a high electric field causes an avalanche which leads to a large number of electrons producing thus an electric signal at the anode, which is sufficient to trigger the read out electronics. For a given voltage, the gain depends on the distance between the micro-mesh and the anode wire. The geometry of the amplification region (some tens of microns thick) is crucial for achieving analog signal amplification and therefore good energy resolution.

Ionization and charge amplification in a Micromegas detector:
Figure 5.2 illustrates the various detector layers (1) – (5) and shows the gas ionization inside the conversion region if a charged particle is passing through the layer, creating electron ion pairs (1). In the absence of electric field the electron ion pairs recombine. For an electric field of about 400 V/cm, the electrons move towards the micromesh (2) while the positive ions drift towards the cathode wire (HV1) [70]. Once the electrons are close to the micromesh (3) it starts feeling the force of an intense electric field of several kV/cm in the amplification gap, which provides the multiplication of the initial ionization electrons.

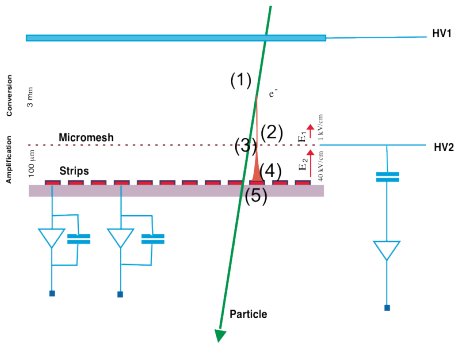

Figure 5.2: *Working principle of a Micromegas detector. The green arrow shows the passing charged particle though the detector volume, allowing to obtain the information of its position, arrival time and momentum direction. The detection process of a particle, be it a charged particle as it is shown here, be it an x-ray photon, goes by amplifying the primary charges that have been created by ionization in the conversion volume (the 3 mm given here between HV1 and HV2). The gas volume of a Micromegas detector is divided in two partitions by the micromesh which can be found at a fixed distance (using pillars) between 25 µm and 150 µm above the readout electrodes ("Strips") [70].*

The electric field is homogeneous both in the drift volume and also in the amplification gap. The drift electrons when they reach the Micromesh openings they start being accelerated by the field E_2 and gain enough energy to produce new electron-ion pairs which in turn will also ionize the gas and create even more pairs. This process results to an avalanche effect (region (4) in Figure 5.2). The short amplification region allows for small gain fluctuations and good energy resolution.

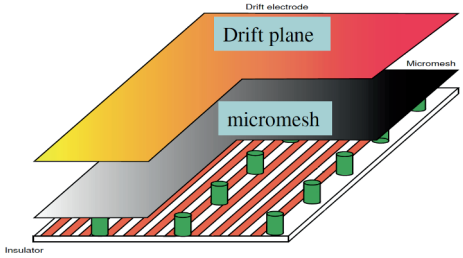

Figure 5.3: *Schematic drawing of Micromegas detector. In green color we see the pillars (of 400µm diameter) that define the distance between the micro-mesh layer and the anode (strips) [72].*

This very simple detection concept has many advantages: a very low material budget,

only two moderate-voltages suffice to operate it, a fast electron signal, an efficient and fast positive ion collection (due to the small gap size), high rate capabilities as well as a low space charge build-up. The mentioned avalanche effect represents a built-in signal amplifier, which allows the electronic signal to be read by the connected charge sensitive preamplifiers on the readout electrode (5).

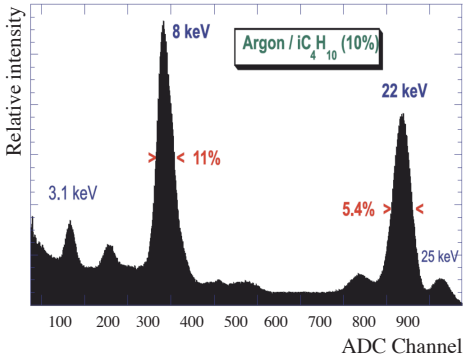

Figure 5.4: *Cd-109 analog source spectrum obtained with Micromegas using an Ar / iC_4H_{10} [90:10] mixture [100].*

The readout electrode is usually divided in strips and/or pixels which allow to reconstruct the particle's xy position as well as read the arrival time and energy through the amplitude and the shape of the signal on the readout electron [70]. The small amplification gap of the Micromegas allows for an excellent spatial resolution: micromegas is a precise detector reaching 12 μm (RMS) accuracy (limited by the pitch of micro-mesh) for MIPs with a low diffusion Ar/iC_4H_{10} [90:10] mixture and very good energy resolution $\sim$12% FWHM at 6 keV (Figure 5.4). Today, the use of the Micromegas technology is growing over a very wide field of experimental physics. Micromegas studies with fast CF_4-based gases are described in [100].

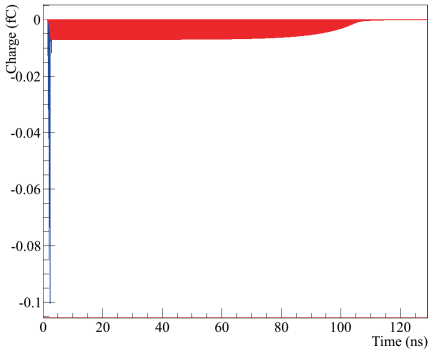

Figure 5.5: *Simulation of the induced signal of a Micromegas detector, due to the movement of electrons and ions. The electrons are amplified in the high electric field region (amplification gap). These signals have both slow (∼kHz) and fast (∼GHz) components, which are modified by the signal propagation properties of the detector, before being filtered, shaped and discriminated by the read-out electronics. It is unavoidable that electronic noise is added throughout this process. Qualitatively, the electron peak is shown in blue, while the slow positive ion tail is given in red, reflecting the underlined processes, which take place inside the detector gas volume [70].*

Applications: Micromegas finds several applications including neutron detection. Neutron interaction with matter results to secondary charged particles such as electrons and/or recoiling nuclei. In order to detect this kind of secondary ionization by a Micromegas, two practical possibilities exist: either using the detector gas filling itself, or target for example its entrance window with an appropriate deposition with sufficient large cross section for neutrons. Micromegas detectors are also used in searches for dark matter particles e.g. solar axions with the CAST experiment at CERN [73], where the signal originates from the solar axion conversion into low energy photons (1 – 10 keV). Micromegas detector with high granularity anode elements can largely reduce the background event rate ($\sim 10^{-6}$ counts $\mathrm{keV}^{-1}\mathrm{cm}^{-2}\mathrm{s}^{-1}$), benefiting from its good resolution (spatial and energy) and its stability [21]. The pixelized anode readout of Micromegas-type detectors is used widely since it allows a two-dimension image reconstruction and opens novel detection opportunities for: high rate particle tracking as well as dark matter and dark energy particle candidates [51].

5.2 Micromegas Technology

The basic idea behind manufacturing large size gaseous detectors is to integrate the micro-mesh into the printed circuit board (PCB), that carries the readout electrodes, becoming thus a robust monolithic detector, aiming to meet the needs of a variety of

state-of-the-art experimental configurations. We mention, for example, the so called InGrid technology, which provides an accurate control of electronic alignment and grid geometry [51].

In the past, there has been a continuous trend towards higher channel count and smaller readout pitches. A new gas detector, Gossip (Gas On Slimmed Silicon Pixels) being still under development, consists of a thin gas layer (only 1 mm) and CMOS pixel array read out on a thinned silicon substrate.

The Gossip detector may become a complimentary development to the present Si-strip tracking systems, since they can be produced cheaper and lighter than the current Si-based detectors. With gas as detection medium (instead of silicon) has certain advantages: the detector charge signals can be relatively large, and the input pixel capacitance can be extremely small reducing this way the power dissipation and preamplifier noise. The pixel chips can be slimmed down to 50 μm, reducing the material budget. Due to its low power dissipation only modest cooling is required. We present the InGrid technology and the Gossip detector in the next Chapter.

5.3 Electron Transmission of a Micromegas: comparison between experiment and simulation

Figure 5.6 shows a simplified diagram of the Micromegas detector assembly, which was used to measure the electron's transmission and final detection.

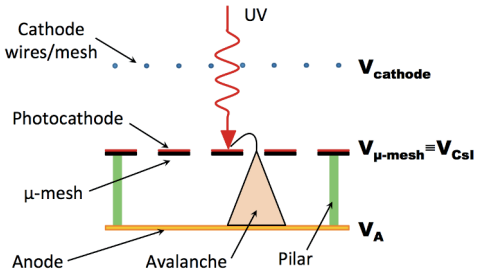

Figure 5.6: *Schematic view of the Micromegas detector assembly which was used to measure the electron transmission in the final amplification stage, i.e., the detection efficiency of a photo-electron produced near the μ-mesh by the UV irradiation. It shows the anode plane (bottom), the photo-sensitive micro-mesh ("photocathode") and the plane of the partially transparent cathode made out of wires or a mesh (top).*

The set-up allowed to extract photo-electrons from the micro-mesh, which was covered with a thin photo-sensitive CsI layer. The external UV light incident on this photo-sensitive mesh caused the electron extraction in a controlled way.

The ultimate goal was to measure the electron transmission, which includes the combined a) photo-electron extraction efficiency, and b) the probability of the photo-electron to enter into the amplification gap giving also rise to a signal. In order to

estimate the electron transmission of the micro-mesh, the following measurement was performed: the assembly of the Micromegas and the cathode plane were placed into a chamber with a quartz window, being transparent to the used UV light ($E_\gamma \approx 6$ eV). In this set-up we could apply different voltages to the anode, the micro-mesh and the cathode (wires/mesh), follow thus the detector performance and compare it finally with the simulation.

5.3.1 Measurements applying a combination of voltages

Case–A: Extraction efficiency of photo-electrons:

In this first configuration, the anode and the μ-mesh were set to the ground, while the cathode-wires were polarized positively ($V_{anode} = V_{mesh} = 0$ V, $V_{cathode} = +$ V). In this case, we could measure the electron extraction efficiency from the photosensitive μ-mesh (CsI) as a function of the electric field between cathode and μ-mesh. The extracted electrons propagate only towards the cathode and the cathode current is a measure of their intensity. The extracted number of electrons is then used for normalization purposes, in order to derive in an additional measurement the actual transmission efficiency from the μ-mesh to the anode plane. The measurement was repeated for three different gas mixtures of Neon with 5%, 10% and 50% ethane (quencher), in order to know when electron amplification occurs eventually also inside the conversion region and avoid it (Table 5.1).

The measurements of the electron transmission in the detector are compared with Ansys – Garfield++ simulation, in which 400 initial electrons were emerging perpendicular out of the photocathode. Later, a slightly more negative voltage was applied on the cathode relative to the photosensitive mesh, in order to suppress electrons moving towards the cathode. Because this "escaping" possibility would reduce the actual electron transmission from the μ-mesh all the way to the anode, where the signal is measured.

Table 5.1: *Simulation results for Ne/C_2H_6: photo-electron extraction.*

a1 – Ne/C_2H_6 [95:5] – $V_{anode} = V_{mesh} = 0$ V						
$V_{cathode}$	-1V	-2V	-5V	-10V	-50V	-100V
Total number of e^-	400	400	400	400	400	400
Number of e^- on the μ-mesh	379	376	390	382	396	399
Number of e^- on the cathode	0	0	0	0	0	0
Number of e^- in the avalanche gap	21	24	10	18	4	1

a2 – Ne/C_2H_6 [95:5] – $V_{anode} = V_{mesh} = 0$ V						
$V_{cathode}$	+1V	+2V	+5V	+10V	+50V	+100V
Total number of e^-	400	400	400	400	508	1452
Number of e^- on the μ-mesh	284	218	131	73	12	7
Number of e^- on the cathode	104	179	269	325	496	1443
Number of e^- in the avalanche gap	12	3	0	2	0	2

b1 – Ne/C_2H_6 [90:10] – $V_{anode} = V_{mesh} = 0$ V						
$V_{cathode}$	-1V	-2V	-5V	-10V	-50V	-100V
Total number of e^-	400	400	400	400	400	400
Number of e^- on the μ-mesh	372	381	391	385	394	395
Number of e^- on the cathode	0	0	0	0	0	0
Number of e^- in the avalanche gap	26	19	9	15	6	5

b2 – Ne/C_2H_6 [90:10] – $V_{anode} = V_{mesh} = 0$ V						
$V_{cathode}$	+1V	+2V	+5V	+10V	+50V	+100V
Total number of e^-	400	400	400	400	427	912
Number of e^- on the μ-mesh	291	243	124	73	22	7
Number of e^- on the cathode	105	155	274	327	405	905
Number of e^- in the avalanche gap	4	2	2	0	0	0

c1 – Ne/C_2H_6 [50:50] – $V_{anode} = V_{mesh} = 0$ V						
$V_{cathode}$	-1V	-2V	-5V	-10V	-50V	-100V
Total number of e^-	400	400	400	400	400	400
Number of e^- on the μ-mesh	386	388	390	394	393	396
Number of e^- on the cathode	0	0	0	0	0	0
Number of e^- in the avalanche gap	14	12	10	6	7	4

c2 – Ne/C_2H_6 [50:50] – $V_{anode} = V_{mesh} = 0$ V						
$V_{cathode}$	+1V	+2V	+5V	+10V	+50V	+100V
Total number of e^-	400	400	400	400	400	401
Number of e^- on the μ-mesh	258	234	139	104	33	13
Number of e^- on the cathode	141	166	261	296	367	388
Number of e^- in the avalanche gap	1	0	0	0	0	0

Case–B: Loss of extracted photo-electrons:
In this second measuring configuration, the anode was set to ground while the cathode wires/mesh and the μ-mesh ("photocathode") were polarized to the same negative potential ($V_{anode} = 0$ V, $V_{cathode} = V_{mesh} =$ - V). During such a measurement, the extracted electrons are forced by the electric field (Figure 5.1) to enter into the micro-mesh holes. The difference in the normalized current between case–A and case–B gives then the loss due to electron reattachment to the μ-mesh (Table 5.2).

Table 5.2: *Simulation results for Ne/C_2H_6: Estimation of electron loss.*

a – Ne/C_2H_6 [95:5] – V_{anode} = 0 V, $V_{cathode} = V_{mesh}$					
$V_{cathode}$	-10V	-20V	-50V	-100V	-200V
Total number of e^-	400	404	505	1126	7121
Number of e^- on the μ-mesh	217	401	223	204	173
Number of e^- on the cathode	11	6	3	0	1
Number of e^- in the avalanche gap	171	182	279	922	6947

b – Ne/C_2H_6 [90:10] – V_{anode} = 0 V, $V_{cathode} = V_{mesh}$					
$V_{cathode}$	-10V	-20V	-50V	-100V	-200V
Total number of e^-	400	402	464	1152	10760
Number of e^- on the μ-mesh	213	202	186	181	152
Number of e^- on the cathode	9	5	1	0	0
Number of e^- in the avalanche gap	178	194	242	971	10610

c – Ne/C_2H_6 [50:50] – V_{anode} = 0 V, $V_{cathode} = V_{mesh}$					
$V_{cathode}$	-10V	-20V	-50V	-100V	-200V
Total number of e^-	400	400	400	449	2056
Number of e^- on the μ-mesh	223	220	188	164	141
Number of e^- on the cathode	2	1	0	0	0
Number of e^- in the avalanche gap	175	179	212	285	1915

Case–C: Loss of extracted photo-electrons with cathode wires (see Case–B):
In the third detector configuration, the anode was set to the ground, while the cathode mesh/wires and the μ-mesh ("photocathode") were polarized negatively (V_{anode} = 0 V, $V_{cathode} = V_{mesh}$ + 1 Volt). The extracted electrons are forced also in this case by the electric field (Figure 5.1) to enter into the μ-mesh holes. This case with +1 Volt more positive potential on the cathode is considered rather as an approximation to a cathode made out of wires, with the potential being not ideally constant over the whole cathode surface.

Table 5.3: *Simulation results for Ne/C_2H_6 like in Table 5.2 with cathode wires (see text).*

a – Ne/C_2H_6 [95:5] – V_{anode} = 0 V, $V_{cathode}$ = V_{mesh} + 1 V					
V_{mesh}	-10V	-20V	-50V	-100V	-200V
$V_{cathode}$	-9V	-19V	-49V	-99V	-199V
Total number of e^-	400	400	504	943	6997
Number of e^- on the μ-mesh	191	204	208	166	148
Number of e^- on the cathode	83	66	67	70	46
Number of e^- in the avalanche gap	126	130	229	707	6802

b – Ne/C_2H_6 [90:10] – V_{anode} = 0 V, $V_{cathode}$ = V_{mesh} + 1 V					
V_{mesh}	-10V	-20V	-50V	-100V	-200V
$V_{cathode}$	-9V	-19V	-49V	-99V	-199V
Total number of e^-	440	400	447	973	9801
Number of e^- on the μ-mesh	206	86	195	159	120
Number of e^- on the cathode	82	198	71	69	60
Number of e^- in the avalanche gap	112	116	181	745	9621

c – Ne/C_2H_6 [50:50] – V_{anode} = 0 V, $V_{cathode}$ = V_{mesh} + 1 V					
V_{mesh}	-10V	-20V	-50V	-100V	-200V
$V_{cathode}$	-9V	-19V	-49V	-99V	-199V
Total number of e^-	400	400	400	450	2259
Number of e^- on the μ-mesh	226	208	179	145	130
Number of e^- on the cathode	79	84	71	45	20
Number of e^- in the avalanche gap	95	108	150	260	2109

5.3.2 Experimental data

The ratio of the measured normalized electron intensity in the case–B to that in the case–A gives the experimentally measured electron transmission. The transmission starts its propagation caused by the ambient electric field, from the upper surface of the μ-mesh (the "photocathode") and all the way to the anode. The results of the measurements are shown in Figure 5.7 and 5.8. As these plots show, the measured electron current for low electric field values is independent of the gas mixture. For stronger electric fields amplification starts to occur first for the 10% ethane admixture (even earlier for the 5% ethane admixture, which is not shown), and for the 50% ethane content later (i.e., at higher electric fields). This allows to use the 50% mixture values in order to derive the plateau values, and build thus the ratio $I_{(Case-B)}/I_{(Case-A)}$. Moreover, using the 50% mixture allows to utilize a wider range of applied voltages.

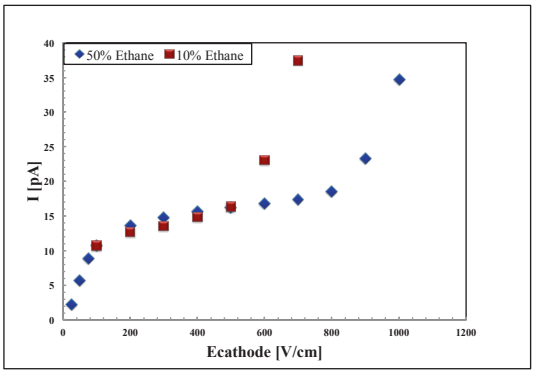

Figure 5.7: *Electron current measured with the cathode wires ($V_{anode} = V_{mesh} = 0$ V, $V_{cathode} = +$ V).*

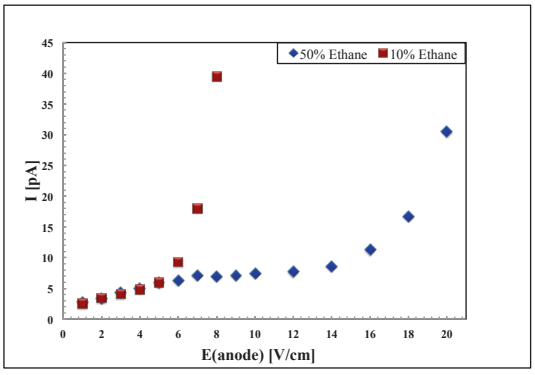

Figure 5.8: *Electron current measured with anode strips ($V_{mesh} = V_{cathode}$, $V_{anode} = +$ V).*

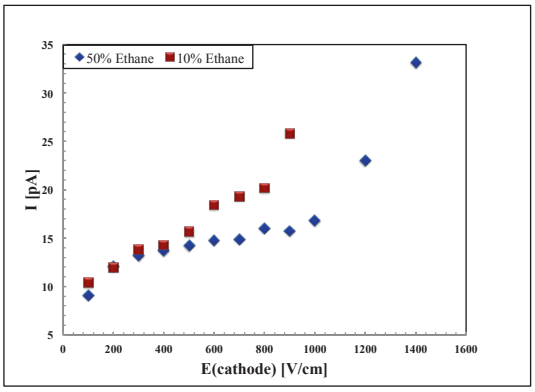

Figure 5.9: *Electron current measured with cathode mesh ($V_{anode} = V_{mesh} = V_{CsI} = 0$, $V_{cathode} = + V$).*

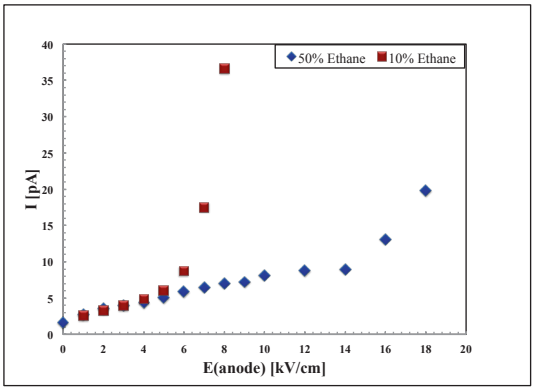

Figure 5.10: *Electron current measured with anode strips ($V_{cathode} = V_{mesh} = V_{CsI} = 0$, $V_{anode} = + V$).*

From the case–A with the cathode wires (Figure 5.7 and 5.8) it follows that the plateau of the extracted photocurrent by the cathode is about 18 pA. From case-B, the transmitted electron photocurrent measured at the anode is about 7 pA (for $E_{anode} \approx 9$ kV/cm). Thus, the so derived electron transmission, i.e., the measured electron intensity at the anode divided by that emitted by the photosensitive μ-mesh, is:

$$f_{transmission} \simeq \frac{7pA}{18pA} \simeq 39\% \tag{5.1}$$

In the case of $E_{anode} \approx 5$ kV/cm, this ratio becomes:

$$f_{transmission} \simeq \frac{5pA}{18pA} \simeq 27\% \tag{5.2}$$

When the cathode wires are replaced by a transparent cathode mesh (Figure 5.9 and 5.10), the corresponding photocurrent measured by the cathode is about 15 pA (Figure 5.9). The transmitted electron photocurrent at the anode was measured to be 8 pA for $E_{anode} \approx 9$ kV/cm (Figure 5.10) and 5 pA for $E_{anode} \approx 5$ kV/cm (Figure 5.10). Using these values, the derived electron transmission is:

$$f_{transmission} \simeq 53\% \tag{5.3}$$

and

$$f_{transmission} \simeq 33\% \tag{5.4}$$

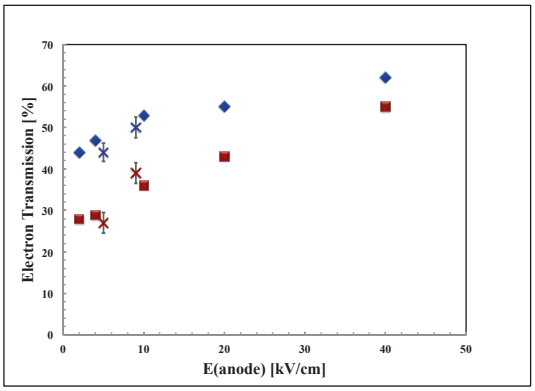

Figure 5.11: *Experimental validation of simulation results using Ansys and Garfield++ tools. The blue points refer to the cathode mesh and the red ones to the cathode wires plane for the gas mixture: 50% Ar and 50% C_2H_6. The blue and red crosses are the corresponding measured values for anode electric fields $E_{anode} \approx 5$ kV/cm and $E_{anode} \approx 9$ kV/cm, using cathode wires (red crosses) and cathode mesh (blue crosses).*

We performed a simulation with the Garfield++ code and we compared the results with the measurements. Interestingly, similar to the experimentally obtained transmission values were derived also from our simulations. A precise 3D model of the μ-mesh was introduced, while the ambient electric field was calculated using the Ansys code.

A uniform voltage was applied on the cathode mesh ($V_{cathode}$) and on the anode (V_{anode}), when simulating the actual experimental configurations. Both, experimental and simulated results are shown in Figure 5.11; it is seen that the maximum measured transmission with the cathode wires is ∼39%, while that with the cathode mesh is, as expected, even better and equal to ∼50%. Interestingly, these two values, at

$E_{anode} \approx$ 9 kV/cm, together with the other two values at a little lower anode electric field, at $E_{anode} \approx$ 5 kV/cm, reproduce the simulation results.

5.4 Conclusions

The electron transmission from the Micromegas μ-mesh layer all the way to the anode includes also the charge amplification occurring during this last step of the initially produced ionization charges in the conversion volume. In these measurements the electrons were produced near the μ-mesh by photo-ionization, using a UV-light source. Applying a few combinations of voltages to the three different layers of the Micromegas detector, i.e. the cathode, the μ-mesh and the anode, we could measure the transmission of electrons with few eV kinetic energy.

The so derived experimental values of the electron transmission have been compared with the simulated values obtained with the Ansys and Garfield++ codes. The agreement between simulation and measurement is quite satisfactory. This is certainly an experimental validation of the simulation codes used throughout this work. In addition, these measurements provide more insight of the actual processes occurring during this last step of signal creation in a Micromegas detector. We recall, this very last propagation of the initial ionization charges occur in a region whose configuration distinguishes Micromegas from all the other detectors used in particle physics.

CHAPTER 6

THE GOSSIP DETECTOR

Outlook

Gas On Slimmed Silicon Pixels (Gossip), is a detector from the grid pix family [109]. The Gossip has been designed to operate with a minimal drift gap (∼1 mm). Gossip is an assembly of a Timepix pixel chip acting as an active anode, covered with a thin protection layer of Silicon Rich Nitride (SiRN), an integrated amplification grid (InGrid) [110] on top of the chip, a drift gap and a cathode wire.

This work aims to predict the performance of the Gossip design and improve it. This is done in different steps; measurements of the InGrid holes, field calculations and a set of laser measurements that we performed at Nikhef. The Gossip operating point is a collection of many parameters such as the pixel size, the drift gap, the avalanche gap, the gas mixture, the gas gain, the drift field and the signal shaping time. We use the Garfield++ simulation code in order to provide a reasonable simulation of the ionization, drift, avalanche and signal.

In Section 6.1 we give an overview of the operation principle of the Gossip detector and we describe some technical details of the detector. Section 6.2 presents the measurements of the InGrid holes under the electronic microscope. Section 6.3 shows the field calculations made for our detector. In Section 6.4, the laser set-up used for the characterization of the GridPix as well as the data calibration are described. Finally, in Section 6.5 we present various simulations with different detector geometries and different gas mixtures.

6.1 Principle of operation

As we showed at the beginning of this work, future LHC experiments require long lifetime of detectors since they will have to operate reliably for several years in high radiation environment. Gossip does not suffer from degradation by radiation since gas can be flushed inside. Another advantage is that the gas has a low density and therefore shower effects are reduced [36]. An important aspect in Gossip's development is the

protection of the chip against destructive discharges. The resistivity of the chip against discharges has to be assured by a very safe protection layer.

Gas as detection medium (instead of silicon) has certain advantages: the detector charge signals can be relatively large, and the input pixel capacitance can be extremely small reducing this way the power dissipation and preamplifier noise. The pixel chips can be slimmed down reducing thus the material budget. Due to a low power dissipation only modest cooling is required.

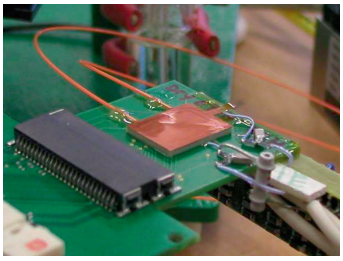

Figure 6.1: *Gossip prototype with SiProt.*

The prototype Gossip detector consists of a CMOS chip which is covered with an integrated grid (InGrid) [110] with holes located at 50 μm above the pixel grid. Given that the detector operates under an electric filed, the pixel matrix is connected to the ground while the grid is at negative potential. The signal in a Gossip detector is formed in a thin gas layer (1 mm) and amplified in the gap of 50 μm (thickness originally designed), between the surface of the CMOS chip and the InGrid. A minimum ionizing particle will produce electron-ion pairs. From these pairs the electrons will drift towards the InGrid through the low field drift region (100 V over 1 mm). The drift time is only 16 ns due to the small size of the drift distance. Figure 6.1 shows a Gossip prototype.

6.1.1 InGrid

The InGrid is a result of a technique called wafer post-processing [111]. This technology allows to build the InGrid - a 1μm thin aluminium plane with holes on top of insulating pillars (SU8) which are placed roughly 50μm above the CMOS pixel chip. Holes and pixels are aligned in order to have an efficient signal measure. The signal inside the detector is mainly collected by one central pixel and its neighboring ones.

Electrons that traverse the gas medium will create avalanches between the grid and the anode wire. Depending on many parameters such as a rising voltage between the anode and the cathode, secondary particles can initiate further avalanches resulting to sparks. Sparks can destroy the InGrid as shown in Figure 6.8. In order to minimize the risks of sparks, a protection layer against sparks is provided by a 10 – 20 μm thin layer of highly resistive material (hydrogenated amorphous silicon) deposited directly over the chip surface [52]. This protection is called “SiProt” and its optimal thickness

is being investigated. The ongoing active R&D work in this field continues beyond this work.

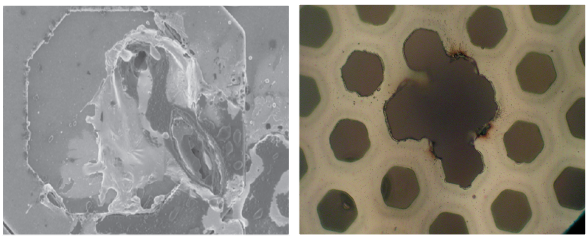

(a) (b)

Figure 6.2: *(a) A pixel input pad melted after the high temperature plasma during a spark and (b) 1 mm thin grid damaged due to a spark.*

Due to the statistical fluctuations in charge during an avalanche, sparks can nor be prevented or predicted. This highly resistive layer is supposed to spread the charge caused by a spark by draining it off much slower than if it was deposited directly on the pixel pad and in parallel protect against the melting of the pads' surface layer.

6.1.2 The Timepix chip

The Timepix chip was designed using the MediPix (X-ray detection) chip as a base design [117]. The chip comprises a 256×256 matrix of 55×55 μm^2 pixels. The fiducial area of the chip itself is 14 mm×14 mm. A pixel cell, as is shown in Figure 6.3, contains a pre-amplifier, a discriminator and a counter. It also contains the octagonal pixel pad on which the charge is collected. The design is an evolution of the Medipix2 chip (MPX) but has a major advantage. An external clock with a frequency up to 100 MHz is controlling the counter of the pixels. This enables each pixel to provide time information with a time resolution down to 10 ns.

The Timepix has four modes of operation which are the following; masked, counting, time over threshold (ToT), and time of arrival (ToA) [121]. The masked mode allows a pixel to be switched off. The counting mode gives one count for each time the output of the amplifier passes the threshold. The counting and ToT modes use the pixels shift register counter with a range of 11,810 counts. When a signal at a pixel cell is above threshold in TOT-mode the counter is incremented by the external clock frequency. The counting stops when the signal at the pixel cell is no longer above threshold [114]. TOT digitalizes the pulse from the pixel pad: a larger avalanche stays longer over threshold.

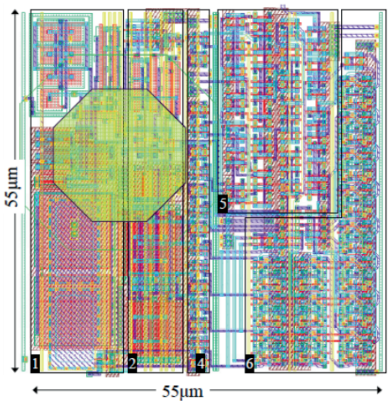

Figure 6.3: *Timepix chip overview: 1. Preamplifier, 2. Discriminator, 4. 8-bit configuration register, 5. Tunable clock reference buffer and Timepix synchronization and 6. 14-bit shift register. In yellow the Octagonal pixel pad. Figure taken from [113].*

In ToA mode, the counter is initiated when the charge on a pixel is above threshold and it stops when the shutter closes. Beyond 11,810 counts the counter saturates. This counting continues until a common stop is set by the read-out software [121]. One such acquisition, called a frame, should not exceed a certain time (depending on the clock frequency) to avoid overflow (represented by count value of 11,810 [114]). If the external clock frequency is 100 MHz the total acquisition window should be at maximum: $(1/100{\cdot}10^6){\cdot}11{,}810{=}118.1$ μs. This allows for a 3D position reconstruction of the drifting electrons, because besides the (x,y) location of the hit pixel cell, time information relative to the other cells is stored in the individual counters. The initial point of the ionization in the gas above the grid can be reconstructed using the corresponding drift velocity of the electrons [121]. The Timepix is beyond the scope of this work.

6.1.3 Relaxd read-out system

The read-out system of our prototype GridPix device is called "Relaxd" and shown in figure 6.4. A Relaxd-board is connected to the computer using a 1 GB ethernet cable and a 100 pins cable to communicate with a quad-board: a chip carrier board of up to four pixel chips, either MediPix or Timepix. Besides hardware also Relaxd software was designed at Nikhef. A program developed by the Czech Technical University in Prague called "Pixelman" was used to read-out the chip connected with the Relaxd hardware [116]. Both programs are able to control the Relaxd-board but have different features. Pixelman allows to visualize the measurements, set read-out settings, save data and perform a threshold equalization scan. The latter calibrates the threshold level of each pixel to all other pixels and subsequently set an overall threshold level. The Relaxd-board has an input for a hardware trigger to determine externally when the pixels on the chips counter are reset and when the common stop is given.

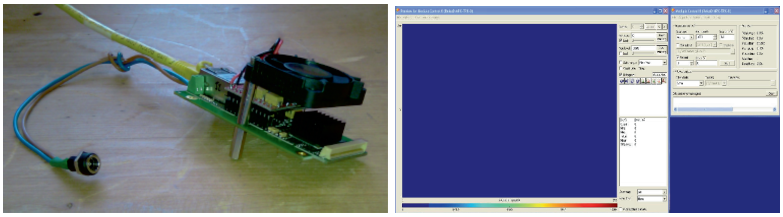

(a) (b)

Figure 6.4: *Left: Relaxed read-out board, a connection to the computer is made using a 1 GB ethernet connection. Right: The Pixelman software screen. Pixelman allows to modify the DAQ settings.*

6.2 GridPix under the microscope

6.2.1 Measuring the holes' diameter on the InGrid

With the use of an optical and a scanning electron microscope (SEM) we focus on the InGrid surface (figure 6.5). Concluding, two independent measurements indicate a hole diameter which varies from 0.30 to 0.35μm. Those results would indicate an inaccuracy in the production of the InGrid's holes, in the spread of the achieved InGrid height as well as in systematic errors in the (microscopic) focussing method.

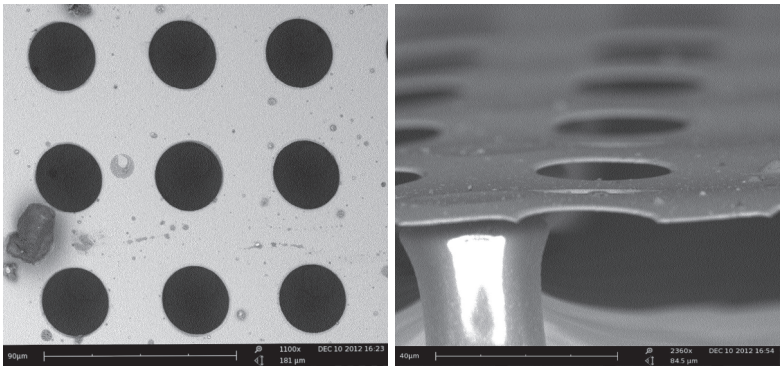

(a) (b)

Figure 6.5: *InGrid holes of the Gossip detector.*

6.3 Field map calculations

6.3.1 Avalanche multiplication

When a single electron initiates a large enough avalanche in the amplification region it can be detected. The primary electrons can ionize the gas under a strong electric field and multiply that way the number of electrons which in turn will cause extra ionization.

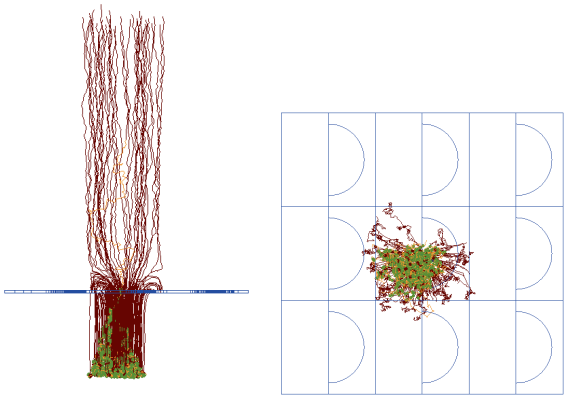

(a) (b)

Figure 6.6: *Electron tracking inside a Gossip detector. The yellow line above the InGrid represents the initial electron while the yellow points below the InGrid show the 200 avalanches produced. The ion tracks are shown with red color.*

6.3.2 Field maps

The electric fields have to be taken into account in the detector structure therefore the potential has to be simulated in advance by Finite Element Methods (FEM) (figures 6.7 and 6.8). The description of the FEM method is beyond the scope of this report. The Garfield++ code provides an interface with ANSYS simulation software [123]. ANSYS is used to find out how a given design (e.g., Gossip detector) works under operating conditions. In this section we present the field calculations for Gossip detector. In Figure 6.8(e) we show the Gossip detector's volumes. The parts "outside" the detector's volume are used for illustration purposes only(yellow and green parts in figure 6.8(c).

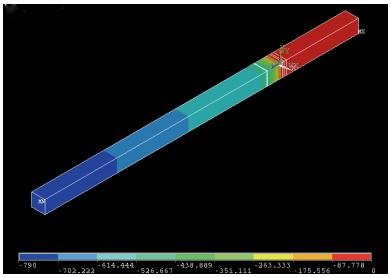

Figure 6.7: *Screen shot of the ANSYS model for the Gossip detector. One example of the meshing and the nodal solution by ANSYS for a 50 µm avalanche gap.*

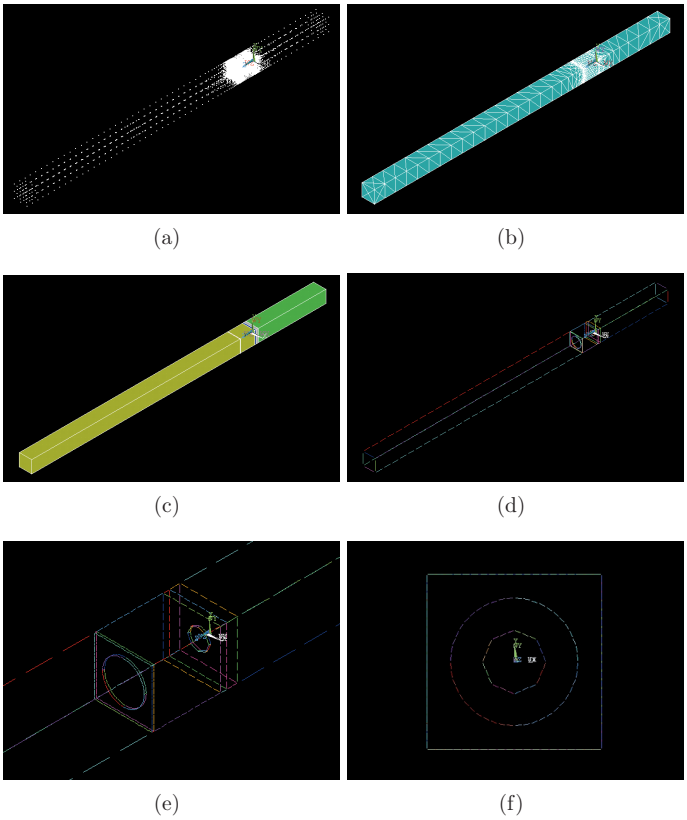

Figure 6.8: *Screen shot of the ANSYS model for the Gossip detector. (a) Nodal solutions (nodes), (b) meshing result (elements), (c) Detector volumes, (d) Detector lines, (e) Detector lines zoom-in, (f) Lines Top View.*

Depending on the applied electric field, the measured current on the readout chip varies. The higher the electric fields the higher the electron kinetic energy (figure 6.8). The higher the kinetic energy the bigger the amount of secondary electrons and therefore the signal measured. Very high electric field should be avoided since this could lead in very large number of secondary electrons (large avalanche) something that could "kill" the readout electronics.

The electric field in the Gossip detector is set at approximately 300 V/cm along the drift region preventing thus recombination. An ionization in the drift region between the cathode and the InGrid will drift a separated electron towards the InGrid. The electric field between the InGrid and the CMOS chip is more dense (80 kV/cm) close to the InGrid due to the negative potential applied on it. As a result secondary electrons will accumulate at the pixel producing the signal. The measured signal is induced by the slow ions which travel towards the cathode.

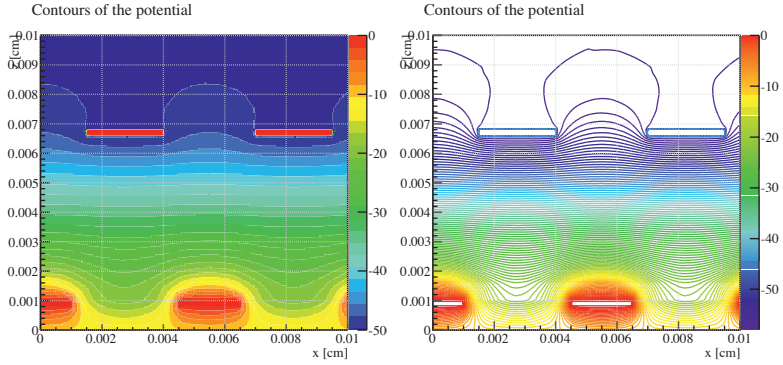

(a) (b)

Figure 6.9: *Surface contours and contours of the potential in the Gossip detector. The InGrid holes (top) and the pixels (bottom) are shown here.*

6.3.3 Weighting field

The Shockley-Ramo theorem is used to compute induced signals from both electrons and ions. The current induced on the electrode is given by the following equation:

$$i = q \cdot \vec{u} \cdot \vec{E_w} \tag{6.1}$$

where q is the moving charge and $\vec{u}$ its velocity. Here $\vec{E_w}$ is the so-called weighting field of an electrode w. It is defined as the field obtained by applying a potential V to that electrode while grounding all other electrodes. The total induced charge (Q) on the

electrode is

$$Q = q \cdot \Delta\phi_w \tag{6.2}$$

where $\Delta\phi_w$ is the weighted potential difference across the charge track.

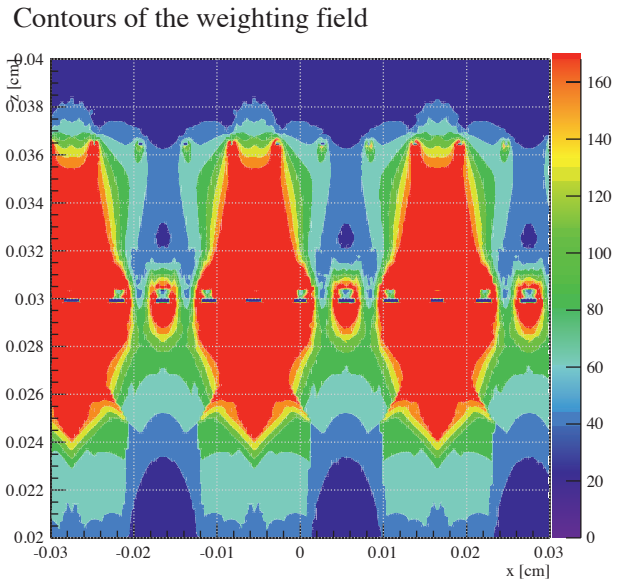

Figure 6.10: *Contours of the weighting field of the Gossip detector calculated with Ansys. It shows the instantaneous current induced on a neighbor electrode (cross talk) by the charge movement. In our case, we set the electrodes voltage at 0 V and every three zero-voltage electrodes we set one at 1 V. At x=-0.005, the electrode is at 1 V (strong field with red color) while its six neighbors - three on the left and three on the right - are set at 0 V.*

Cross talk

As mentioned earlier, the signal collected is not only on a single pixel but also on its neighbors. The effect of this induced signal is called cross talks and is created by the capacitance between pixels. Cross talk is an extra contribution to the signal noise and worsens the spatial resolution.

6.4 Experimental laser set-up

6.4.1 Nitrogen laser

The Nikhef nitrogen laser ((figure 6.11)) has been developed in the 80's by Fred Hartjes [112]. It has been used frequently in the past for the calibration and characterization of many gaseous detectors and detector systems. Such nitrogen lasers have been implemented in two big LEP experiments (L3 and Delphi).

Figure 6.11: *Image of the Nikhef nitrogen laser.*

With this laser setup, we can generate in the focal point of the laser beam a confined charge at a certain position in the gas on a well defined moment (figure 6.12). Subsequently, we may observe where and on which moment the charge arrives at the detector. With this method the response to one single electron can be determined. With x-rays or minimum ionizing particles the detector effects are always obscured by a relatively high number of primary electrons.

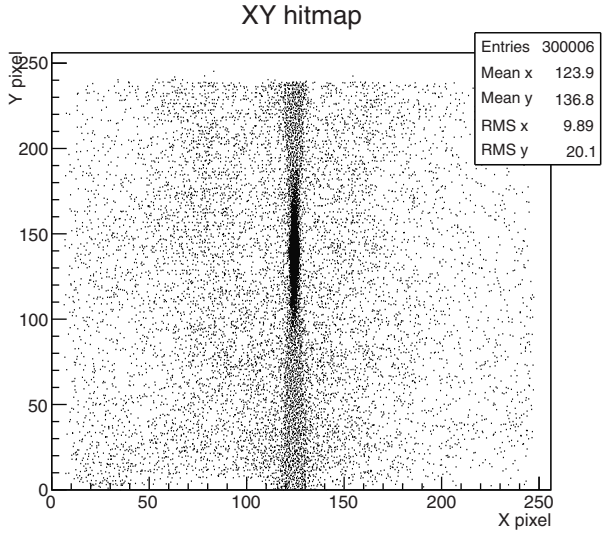

Figure 6.12: *The X and Y hit map of the laser beam as shown in Pixelman for 1000 frames.*

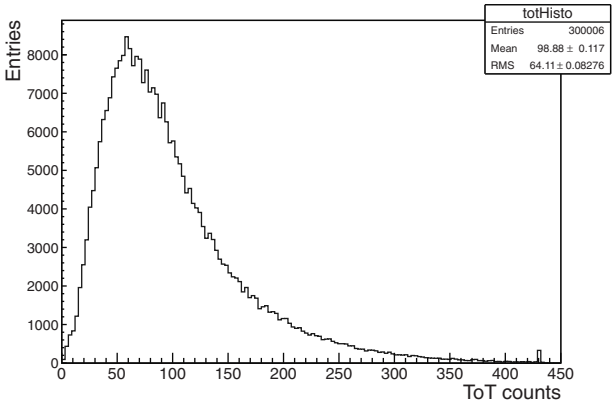

Figure 6.13: *The raw ToT data for high gain (V_{INGrid}= -650 V).*

The pulsed N2 laser emits at 337 nm, i.e. the near UV, the pulse width is 1 ns, and the repetition frequency can be tuned to 5 Hz maximum. The energy of a single pulse is around 80 μJ. The laser operates according to the MOPA (Master Oscillator Power Amplifier) principle. As figure 6.11 shows, the system consists of two identical and synchronized lasers. The "oscillator" and the "amplifier". Each section consists of two

thick metal plates P1, P2, P3 and P4, which are charged to 18 kV [112]. The laser light is generated in the gaps between the plates of each section which are filled with nitrogen at atmospheric pressure. The plates P1 and P3 are connected to a triggered spark gap acting as a fast switch. The "oscillator" starts to emit a laser beam having high divergence because of the absence of the double mirror system (the short duration of the laser pulse (1 ns) does not permit reflections between two mirrors. Subsequently the beam is 20x expanded, reducing the beam divergence very substantially, but at the cost of a great loss of beam power. The weak, but very parallel beam is then directed into the "amplifier", the second stage of the laser, where it is enhanced to a powerful beam that is almost diffraction limited.

6.4.2 Threshold equalization

The pixel discriminator thresholds are set by the low-threshold Digital to Analog Converter (THL DAC). In certain applications equalization can be used to compensate radiation damage effects. The process of setting the bits is the so-called "threshold equalization". This is a standard process and detailed described here: [121].

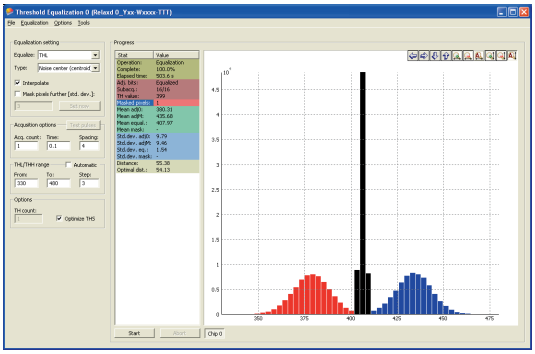

Figure 6.14: *"Noise center" threshold equalization.*

The method of threshold equalization used in this report is the "noise center" method which provides a good approximation of the general noise of the chip by scanning the threshold level and binning the pixels depending on the threshold DAC value at which they start becoming noisy [121]. Threshold scans are made with trims set to minimum (red) and maximum (blue) values(Figure 6.14). The optimum value of the trim is then determined for each pixel and the threshold is rescanned to confirm the width of the distribution (black).

6.4.3 Charge calibration

For the data presented in this work, the mean THL DAC value returned by the equalization scans described above, is ∼410 (DAC steps). The threshold set in DAC steps

is 430, while the nominal threshold in electrons is ∼530, as it can be calculated by the difference between the THL DAC scanned value (∼410) multiplied by the 25.4 electrons expected and the threshold set (430) [118].

In order to correctly interpret the data in the analysis which follows, a charge calibration was performed. For this purpose we have followed the procedure taken from [121]. The goal of the charge calibration is to obtain the relation between the ToT values and the deposited charge in the detector medium. The response in ToT counts is a linear function of the input charge (with a general offset for each hit pixel) with a value dependent on the threshold [121]. In addition, there is a non-linear behavior for charges within about 3000 electrons of the threshold. This behavior is described in [119], where the "surrogate function" is used to parametrize the detector response. The non-linear behavior close to threshold affects the charge sharing distributions between pixels.

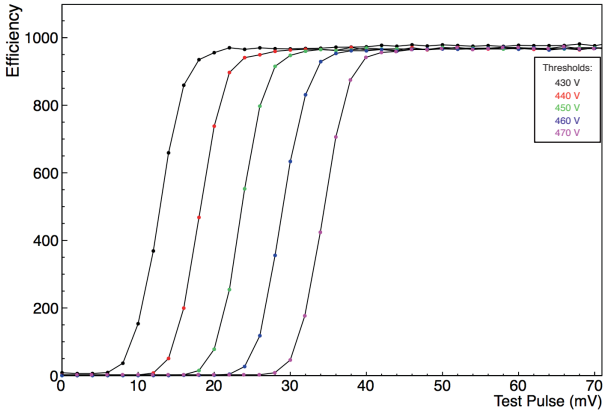

Figure 6.15: *The above efficiency curves show experimental data behavior in relationship to the applied pulse voltage.*

The calibration is performed with test pulses. Each test pulse generates negative (rising edge) and positive (falling edge) pulses [121]. We send several test pulses per shutter to each pixel in order to measure the ToT ("medipix mode" measurement) and efficiency ("counting mode" measurement) for each test pulse height. This is done in two steps, as described below. Note that the period of the test pulses reaching the pixels is important and sent one at a time so that our results are accurate.

We first look at the response in counting mode. Thousand test pulses are sent per frame. We perform five measurements (10 DAC steps) with the values of 430, 440, 450, 460, and 470, corresponding to nominal thresholds of roughly 508, 762, 1016, 1270, and 1524 electrons. Figure(6.15) shows the number of counts (efficiency) as a function of the test pulse voltage. The differences in thresholds between the five measurements (10 DAC steps) correspond very well to the expected value of 25.4 electrons. The second part of the calibration focuses at the chip response and derives the ToT value relationship with

the input charge. Ten test pulses per shutter were sent and in Figure 6.16 we show the ToT values divided by ten, as a function of the applied test pulse voltage. As described in [119] these curves are well described with the following "surrogate function":

$$f(x) = ax + b - \frac{c}{x - t} \tag{6.3}$$

where a is the slope, b the intercept of the line that describes the behavior above threshold. The t and c parametrize the non-linear behavior close to threshold [122]. Figure 6.16 shows the calibration curves for the five thresholds studied. The average parameters can also be obtained by fitting the same "surrogate function" to the ToT value curves as a function of test pulse. Table 6.1 shows the parameters describing the fitted surrogate functions.

Table 6.1: *Surrogate function fit parameters as a result from the ToT test pulse scans.*

Surrogate function fit parameters					
THL	a	b	c	t	Charge (e^-)
430	0.14	11.9	66.2	8.59	508
440	0.10	14.5	270	0.13	762
450	0.10	11.5	241	4.44	1016
460	0.11	9.64	242	7.32	1270
470	0.10	7.69	219	11.9	1524

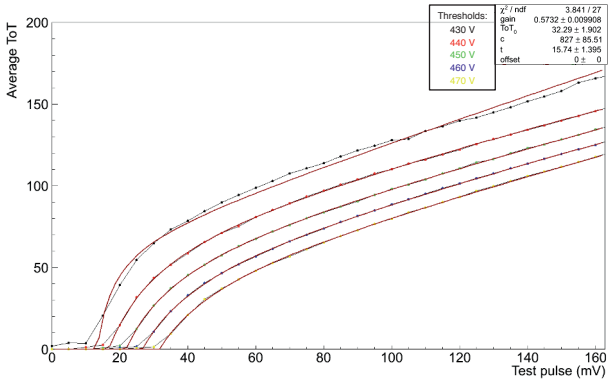

Figure 6.16: *Test pulse response in ToT mode, for five different thresholds. The average pulse response is shown above as a function of the test pulses.*

6.5 Results

One of the most important things in detector performance is the single electron detection efficiency. In other words, the ability to detect all primary electrons which are produced in the drift region. Not all primary electrons reach the gain region and electrons that do initiate an avalanche may escape when the gain is not sufficient.

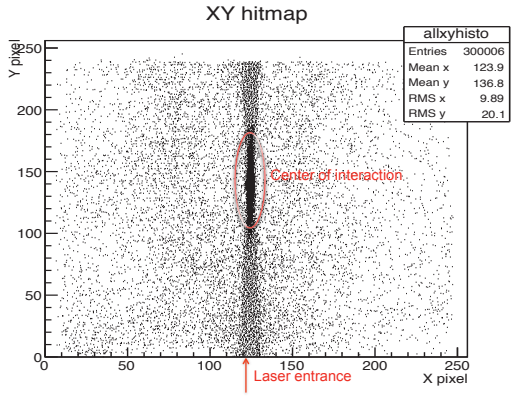

Figure 6.17: *The X and Y hit map of the laser beam. The laser beam entrance is shown as well as the center of the detector/interaction.*

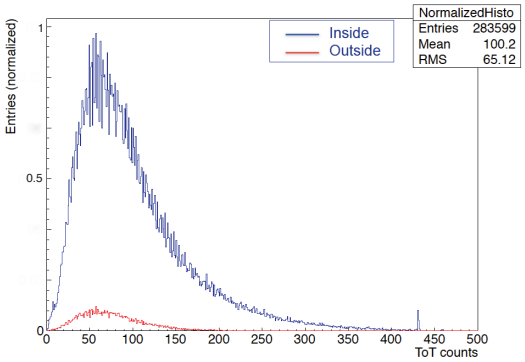

Figure 6.18: *ToT curves for the hits inside (blue) and outside (red) the center of interaction.*

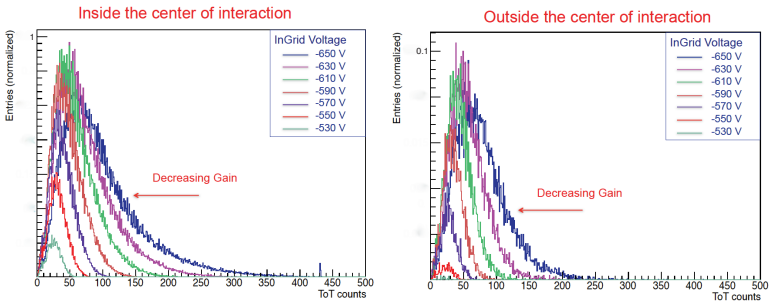

(a) (b)

Figure 6.19: *ToT curves for different sets of applied voltage on the InGrid. Left: ToT behavior taken into account only hits in the center of the detector and Right: ToT behavior for hits outside the center of the detector.*

With the number of electrons arriving in the gain area we can measure the induced charge. The amplitudes of individual avalanches follow a Pólya distribution (figure 6.18 and 6.19) [121].

In this work, we extract the gain from the ToT counts and compare it with the Garfield++ simulation results. We also estimate the detector efficiency as it results by the fraction between the number of events and the run time. We use a GridPix detector with a 20 mm drift gap. The laser beam is placed at 2 and 10 mm above the InGrid (figure 6.20). When single electrons are drifting to the grid these two measurements should give similar results.

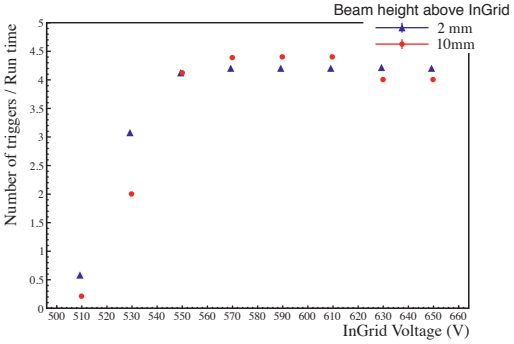

Figure 6.20: *Relative efficiency for two different laser beam heights. The laser is entering the detector at a height of 2 mm (blue points) and 10 mm (red points) above the InGrid.*

The chip is set in ToT mode in order to measure the amplitude of the pixel induced

signals [116]. Using a gas mixture of DME:CO_2 [50:50] a 20 V step scan was made of InGrid voltages between -510 V and -650 V. The calibration data mentioned in last Section could help in calculating the detected charge via the "inverse surrogate function" [121]:

$$q_{in}(e^-) = 46.9 * \frac{t \cdot a + ToT - b + \sqrt{(b + t \cdot a - ToT)^2 + 4 \cdot a \cdot c}}{2 \cdot a} \tag{6.4}$$

which above the threshold region becomes:

$$q_{in}(e^-) = 46.9 * \frac{ToT - b}{a} \tag{6.5}$$

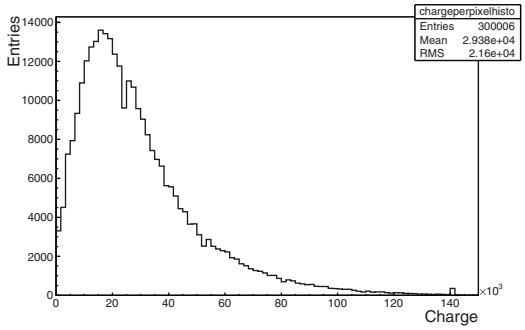

Figure 6.21: *Charge deposited in the detector and as resulted from the raw ToT data.*

Total number of electrons

The following simulations describe the expected behavior of the Gossip detector. Figure 6.22 (a) shows the total number of electrons in the gas volume as a result of 500 initial electron avalanches. Depending on the voltage applied on the InGrid, the size of the avalanches changes (i.e., the total number of electrons produced). This figure also gives information about the size of the InGrid holes and how this affects the created total number of electrons. For example, applying -650 V InGrid voltage we notice that the results vary without following any special shape (note that the InGrid holes' diameter of the Gossip detector which was used in this work were measured at ∼32 μm). Figure 6.22 (b) shows also the total number of electrons only that this time it is drawn as a function of the applied InGrid voltage. In this case, we notice, as expected, a strong increase of the number of avalanche electrons as the InGrid voltage increases.

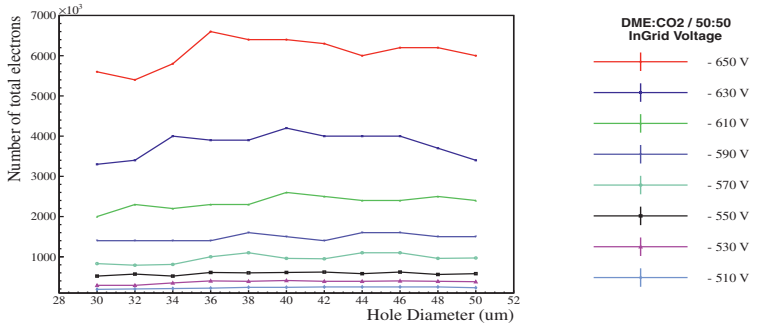

(a)

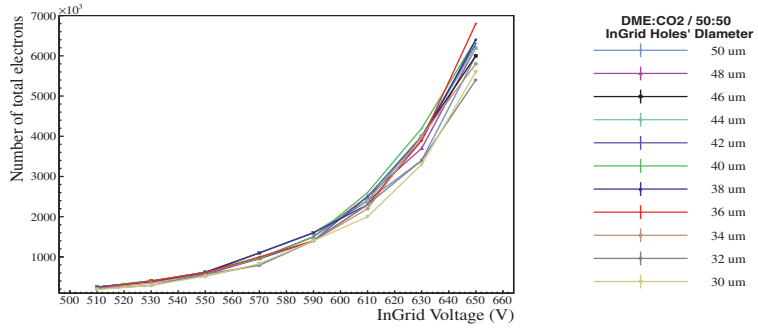

(b)

Figure 6.22: *Garfield++ simulation for the Gossip detector. The gas volume was filled with 50% DME and 50% CO_2. The voltage on the InGrid varies from -530 V to -630 V while the voltage on the anode is set at -790 V. The total number of the avalanche electrons is shown as a function of the diameter of the InGrid holes (a) and the InGrid's voltage (b).*

Gain

Figure 6.23 presents the gas gain of our detector, with (a) showing actually no significant dependence of the detector gain on the InGrid hole diameter for each applied voltage to the InGrid between -510 V and -650 V. The same result is actually illustrated also by the bottom curves (b), which show a rather similar gain dependence on the InGrid voltage for eleven different InGrid hole diameters between 30 and 50 μm.

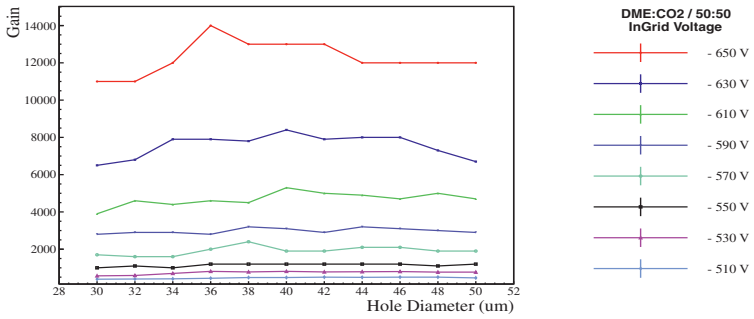

(a)

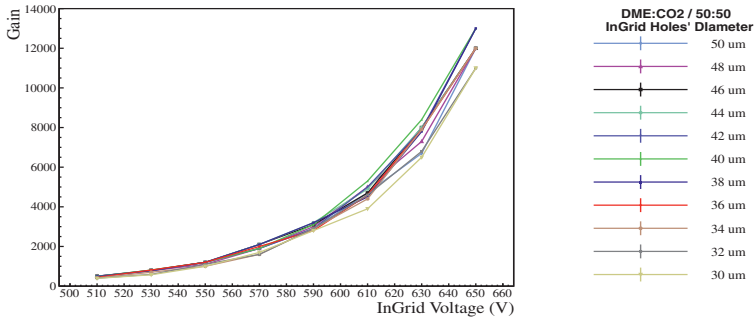

(b)

Figure 6.23: *Garfield++ simulation for the Gossip detector. The gas volume was filled with 50% DME and 50% CO_2. The gain is shown as a function of the diameter of the InGrid holes and the InGrid's voltage which varies between -530 V and -630 V while the voltage on the anode is set at -790 V.*

Number of electrons attached in the gas

The following Figure 6.24 shows the number of the electrons which get "lost" in the gas due to the attachment for a total number of 500 initial electron avalanches. As we see from the plot, this number strongly depends on the voltage applied on the InGrid as well as on the choice of the gas mixture. Losses of avalanche electrons due to the attachment are apparently important for the expected signal strength and make the choice of the gas mixture very important.

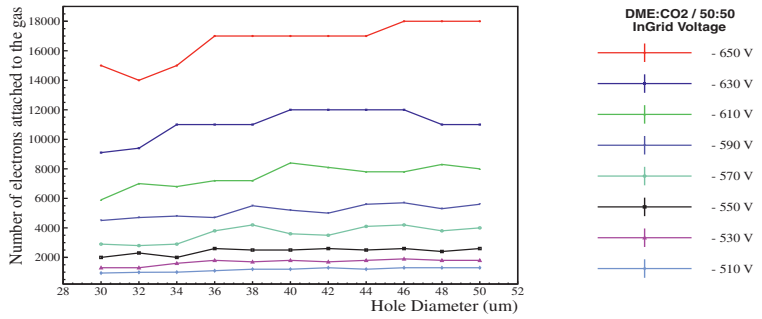

(a)

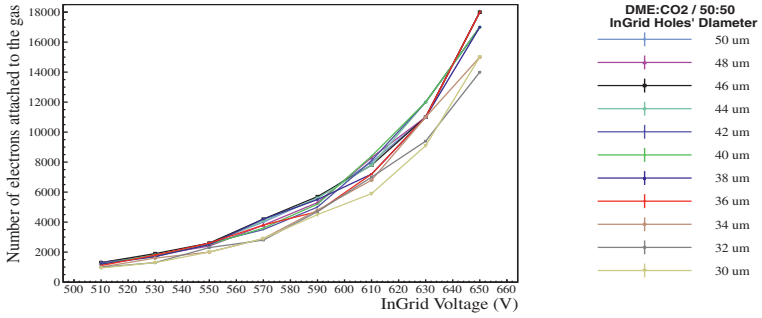

(b)

Figure 6.24: *Garfield++ simulation for the Gossip detector. The gas volume was filled with 50% DME and 50% CO_2. The voltage on the InGrid varies from -530 V to -630 V while the voltage on the anode is set at -790 V. The number of the electrons attached to the gas is shown as a function of the diameter of the InGrid holes (a) and the InGrid's voltage (b).*

Ions stopped on the InGrid

The next two Figures 6.25 and 6.26 show the behavior of the ions in the gas volume as a function of the InGrid voltage and the InGrid holes' diameter. More specifically, in Figure 6.25 we see the amount of ions that stopped on the InGrid (i.e., the ions which finally did not drift through one of the InGrid's holes). As it is expected, the number of ions depends on the diameter of the InGrid holes and indeed it is small for a larger hole diameter. In Figure 6.26, one sees the amount of ions that drift towards the cathode

(i.e., the ions that finally passed through the InGrid holes). The results here are similar to Figure 6.25, as we see that the bigger the InGrid hole the more ions drift through and reach the cathode.

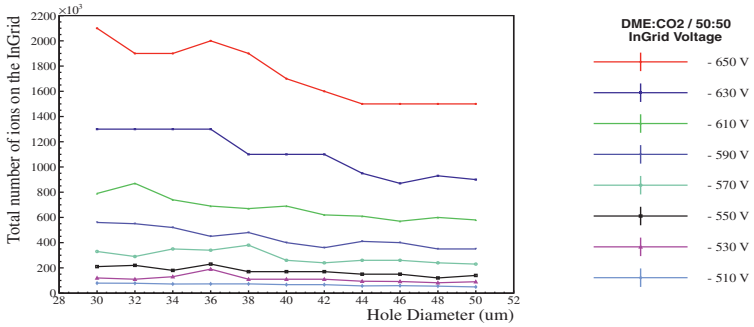

(a)

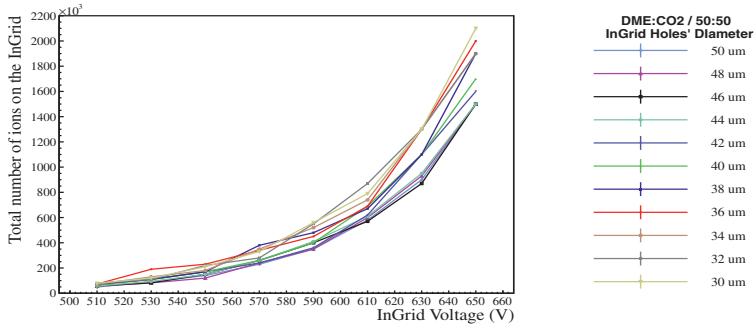

(b)

Figure 6.25: *Garfield++ simulation for the Gossip detector. The gas volume was filled with 50% DME and 50% CO_2. The number of ions stopped at the InGrid is shown as a function of the diameter of the InGrid holes and its voltage. The voltage on the InGrid varies between -530 V and -630 V while the voltage on the anode is set at -790 V.*

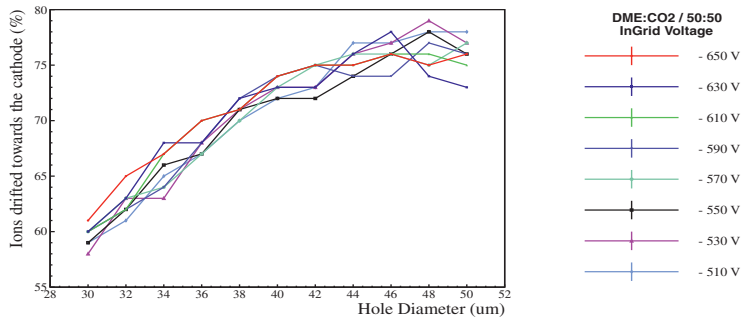

(a)

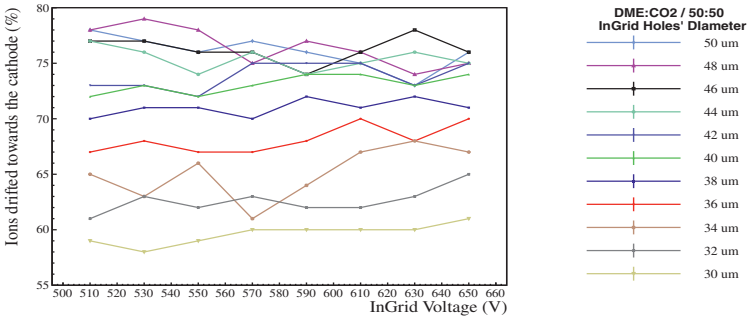

(b)

Figure 6.26: *Garfield++ simulation for the Gossip detector. The fraction of the ions drifted towards the cathode is shown as a function of the diameter of the InGrid holes (a) and the InGrid's voltage (b). The gas volume was filled with 50% DME and 50% CO_2 and the voltage on the InGrid varies between -530 V and -630 V while the voltage on the anode is set at -790 V.*

6.6 Conclusions/Remarks

At low voltages the discrepancies between experimental data and simulation are big, but at the high gain part the simulated underestimation reduces to ∼10% (figure 6.27). The overall behavior expected by the simulation is actually confirmed by the measured data.

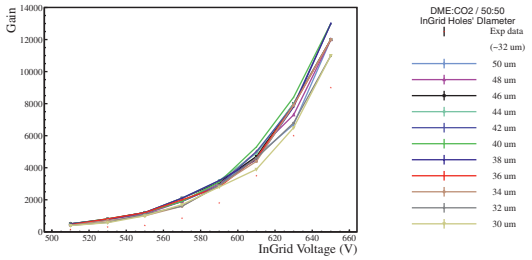

Figure 6.27: *Qualitative agreement between both data (red stars) and simulation (color lines) for a gas mixture of 50% DME and 50% CO_2. While the simulated data are higher than the measured values, the behavior is quite similar.*

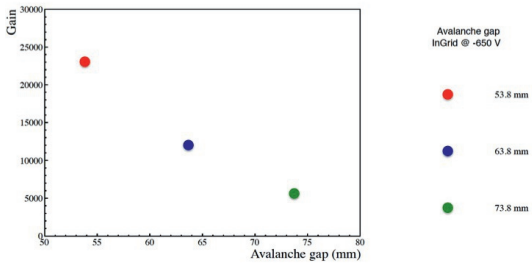

Figure 6.28: *Gas gain behavior as a function of the avalanche gap size in a 50:50 mixture of DME and CO_2.*

At a certain grid voltage the gas gain reaches a maximum. A reduction of the avalanche gap size at constant InGrid voltage results in an increased electric field. For gaps of few mm, the electric field increases resulting in an increase of gain. The relationship between the gas gain and the amplification gap thickness was investigated in this section. The avalanche gap size was set to 53.8, 63.8 and 73.8 μm and the gas mixture was DME/CO_2 50/50. The dependence of the gain with the avalanche gap is illustrated in Figure 6.28 where the InGrid voltage is of -630 V. The hole diameter is the same for all the avalanche gap sizes and therefore it does not affect the gain. Simulation results show

that the gain depends on the gap size and tends to be high for the lowest avalanche gap size shown here. This study could be repeated for other gas mixtures, different avalanche gap sizes and InGrid hole diameters.

APPENDIX

Electron drift velocity

The following plots show the simulated drift velocity of electrons as a function of the electric field for gas mixtures at T=300°K and 1 atm. The simulations are made with the Garfield and Magboltz programs. For this work, the important component is the one parallel to the electric field (orange color) since it is related to the Lorentz angle and diffusion.

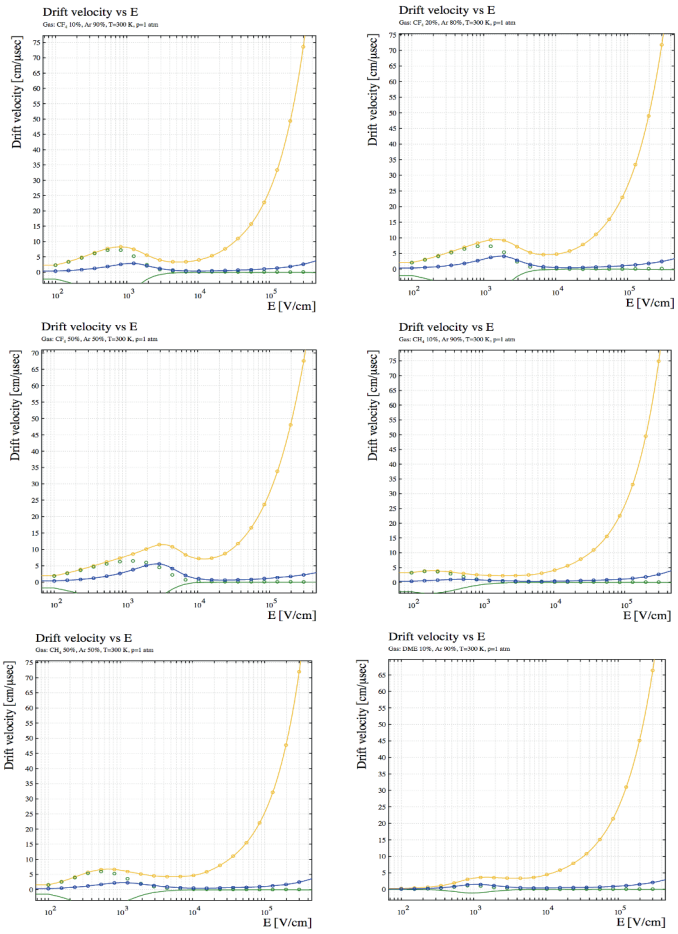

Figure 6.29: *Magboltz simulation of the electron drift velocity as a function of the electric field in the drift volume for several gas mixtures. Different colors represent different components of the drift velocity. Orange: component parallel with the electric field (0°), green: component parallel with the orthogonal part of the magnetic field (45°) and blue: component parallel with ExB (90°).*

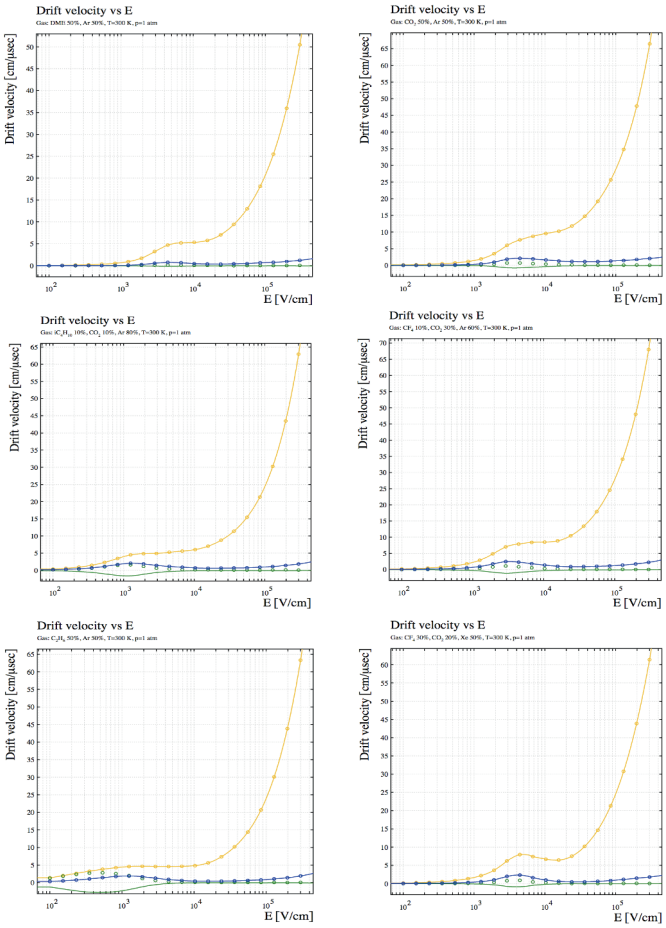

Figure 6.30: *Magboltz simulation of the electron drift velocity as a function of the electric field in the drift volume for several gas mixtures. Different colors represent different components of the drift velocity. Orange: component parallel with the electric field (0°), green: component parallel with the orthogonal part of the magnetic field (45°) and blue: component parallel with ExB (90°).*

Electron and ion diffusion

The presence of a quencher is one of the most efficient ways to minimize the sidewalks of the electrons or in other words the transverse diffusion. In addition, a small electron diffusion implies larger electron drift velocity. Figure 2.10 shows the electron diffusion as a function of the electric field for the gas mixtures: (a) Ar:CO_2 and (b) Ar:C_2H_6. In Figures 6.31 and 6.32 electron diffusion is shown for various gas mixtures.

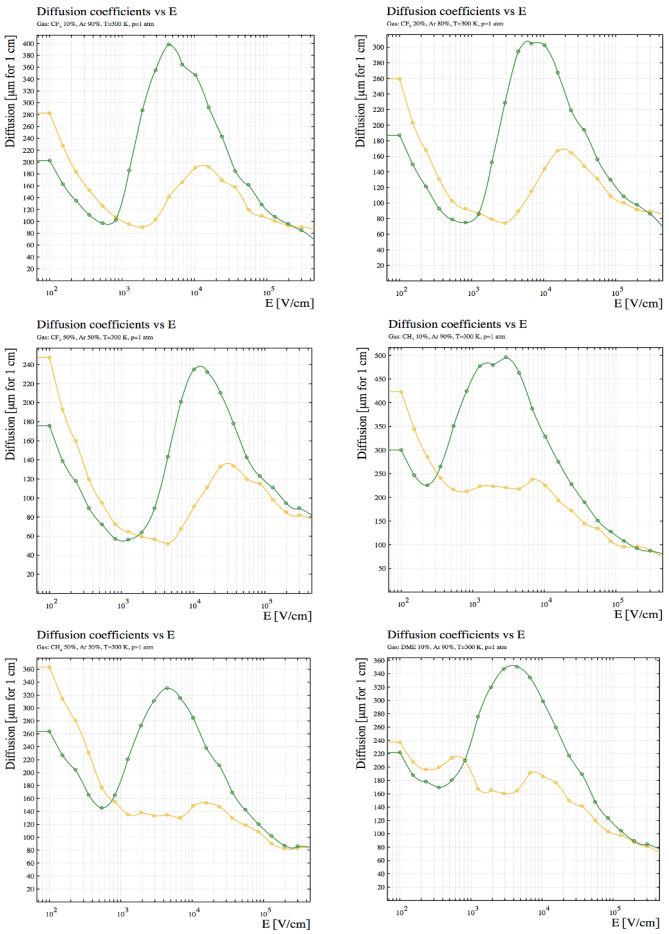

Figure 6.31: *Magboltz simulation of the electron drift velocity as a function of the electric field in the drift volume for several gas mixtures. Transverse diffusion (green) is the diffusion perpendicular to the drift direction and longitudinal diffusion (orange) is the diffusion in the drift direction.*

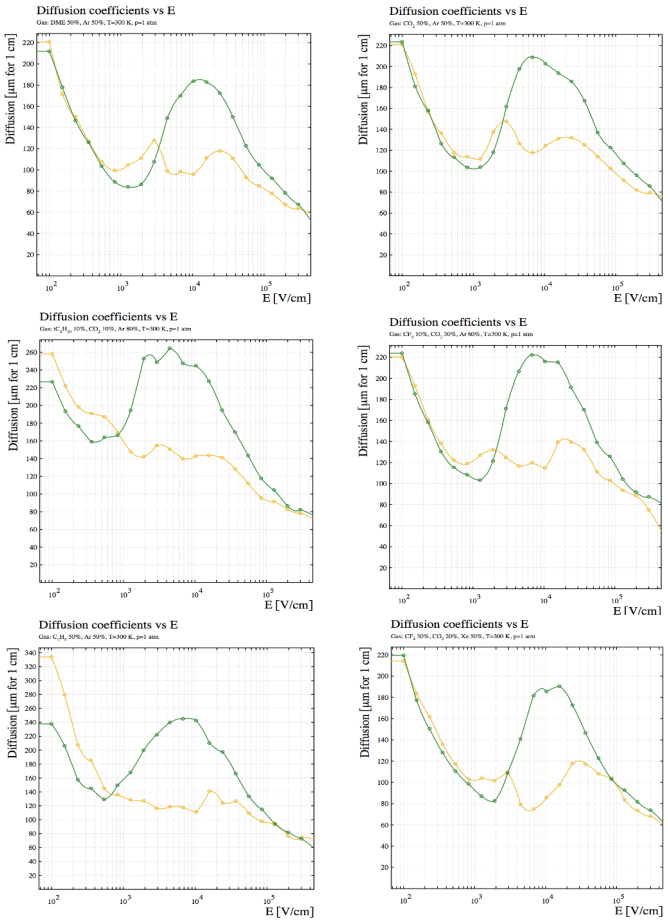

Figure 6.32: *Magboltz simulation of the electron drift velocity as a function of the electric field in the drift volume for several gas mixtures. Transverse diffusion (green) is the diffusion perpendicular to the drift direction and longitudinal diffusion (orange) is the diffusion in the drift direction.*

The Lorentz angle

The Lorentz angle can be used e.g. to enhance charge sharing. If the goal is to minimize the Lorentz angle, the drift velocity should be low, but the electric field should be high (in case the electric and magnetic fields are orthogonal). The following plots show the angle between the drift velocity and the electric field as a function of the electric field for several gas mixtures [37]. The curves correspond to a 90° angle between electric and

magnetic field.

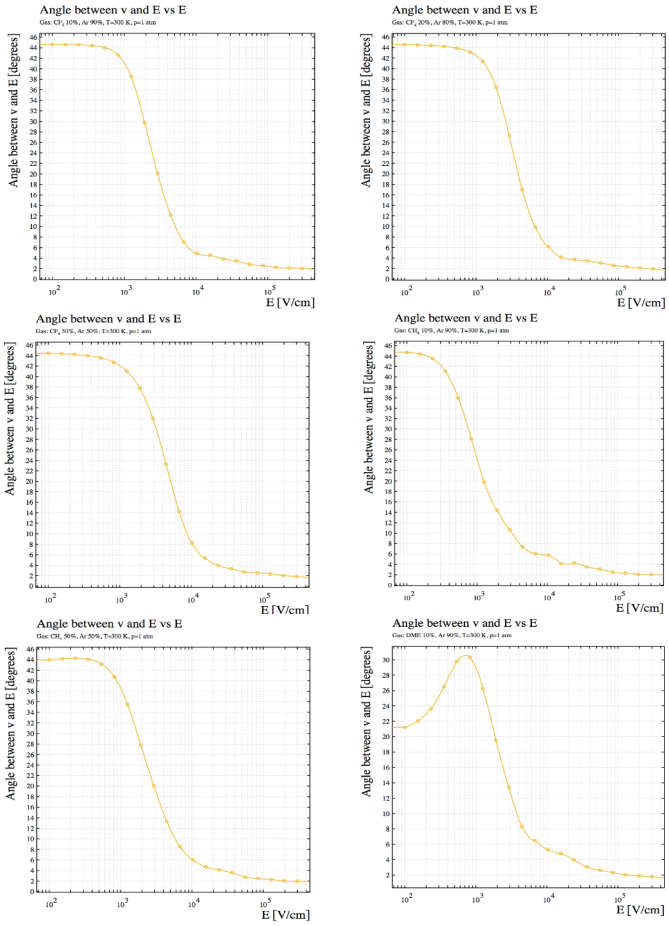

Figure 6.33: *Magboltz simulation of the Lorentz angle for the E×B component as a function of the electric field for various gas mixtures.*

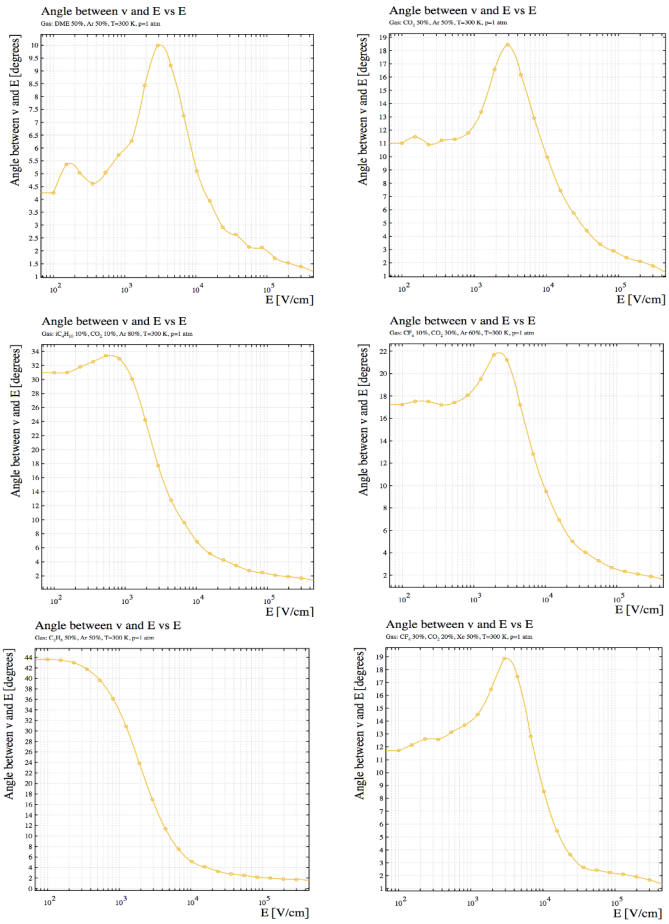

Figure 6.34: *Magboltz simulation of the Lorentz angle for the E×B component as a function of the electric field for various gas mixtures.*

The Townsend and attachment coefficients

The Townsend coefficient α, represents the number of ionizing collisions for an e^- per cm of path length in the direction of the applied electric field. One of the most desirable goals is high gain since the resolution improves with it. For this reason, we are looking for gas mixtures with high α, and preferably a low threshold for the avalanche at low field values. A gas mixture with large α (preferably at low electric fields due to the avalanches) can give a high gas gain. The attachment coefficient η is a measure of a drifting electron and its electron attachment. It is very important for both particle's position and its

identification. Losses of avalanche electrons due to attachment are important for the signal calculation and therefore we need a gas mixture with low attachment coefficient. The following plots show the Townsend (orange) and attachment (green) coefficients as a function of the electric field for a variety of gas mixtures (dissociation coefficient not shown here).

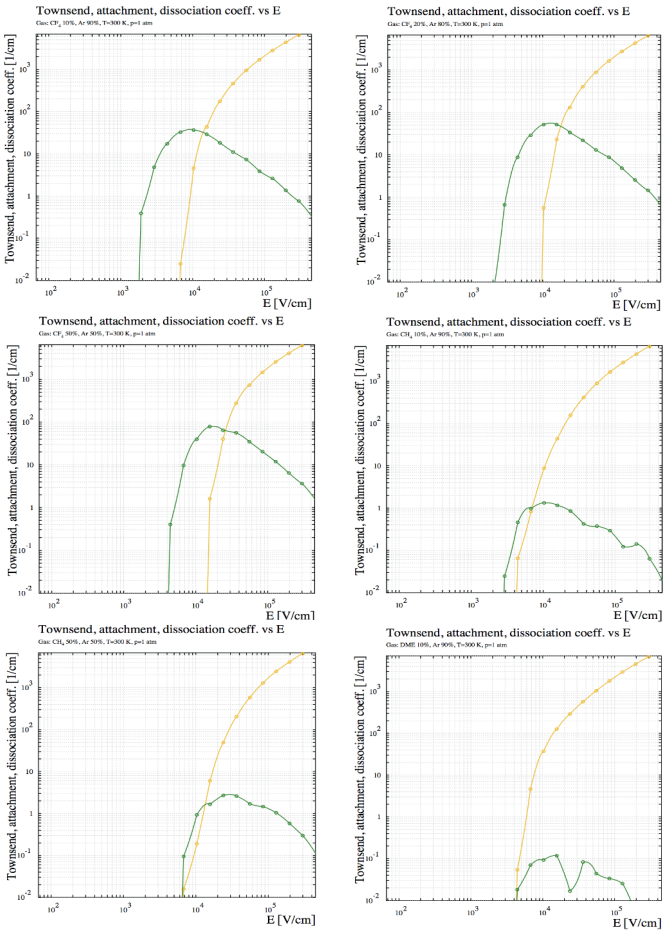

Figure 6.35: *Magboltz simulation of the Townsend and attachment coefficients as a function of the electric field for several gas mixtures. Townsend (orange) and attachment (green) coefficients.*

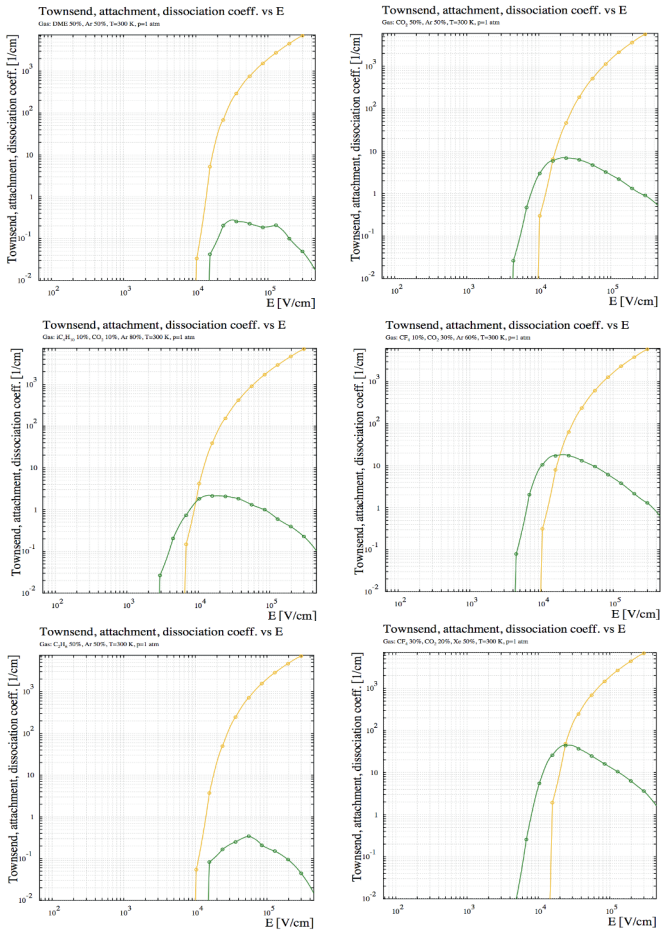

Figure 6.36: *Magboltz simulation of the Townsend and attachment coefficients as a function of the electric field for several gas mixtures. Townsend (orange) and attachment (green) coefficients.*

REFERENCES

[1] P. W. Higgs, *Broken symmetries, massless particles and gauge fields*, Physics Letters **12** (1964) 132-133.

[2] F. Englert and R. Brout, *Broken Symmetry and the Mass of Gauge Vector Mesons*, Physical Review Letters **13** (1964) 321-323.

[3] P. W. Higgs, *Broken Symmetries and the Masses of Gauge Bosons*, Physical Review Letters **13** (1964) 508-509.

[4] G. S. Guralnik, C. R. Hagen and T. W. B. Kibble, *Global Conservation Laws and Massless Particles*, Physical Review Letters **13** (1964) 585-587.

[5] P. W. Higgs, *Spontaneous Symmetry Breakdown without Massless Bosons*, Physical Review **145** (1966) 1156-1163.

[6] ATLAS Collaboration, *Observation of a new particle in the search for the Standard Model Higgs boson with the ATLAS detector at the LHC*, Phys.Lett. B **716** (2012) 1-29.

[7] CMS Collaboration, *Observation of a new boson at a mass of 125 GeV with the CMS experiment at the LHC*, Phys.Lett. B716 (2012) 30-61.

[8] R.D. Peccei, *The Strong CP Problem and Axions*, arXiv:0607268 (hep-ph) (2006).

[9] ATLAS, CMS Collaborations, *Measurements of the Higgs boson production and decay rates and constraints on its couplings from a combined ATLAS and CMS analysis of the LHC pp collision data at* $\sqrt{s} = 7$ *and 8 TeV*, arXiv:1606.02266 (hep-ex) (2016).

[10] ATLAS Collaboration, *Study of the spin and parity of the Higgs boson in diboson decays with the ATLAS detector*, arXiv:1506.05669 (hep-ex) (2015).

[11] D. d'Enterria et al., *High-precision* α_s *measurements from LHC to FCC-ee*, arXiv:1512.05194 (hep-ex) (2017).

[12] ATLAS Collaboration, *Search for squarks and gluinos in final states with jets and missing transverse momentum using 36* fb^{-1} *of* $\sqrt{s}$*=13 TeV pp collision data with the ATLAS detector*, arXiv:1712.02332 (hep-ex) (2017).

[13] https://atlas.web.cern.ch/Atlas/GROUPS/PHYSICS/CombinedSummaryPlots/SUSY/ATLAS_SUSY_Summary/ATLAS_SUSY_Summary.pdf.

[14] https://atlas.web.cern.ch/Atlas/GROUPS/PHYSICS/CombinedSummaryPlots/EXOTICS/ATLAS_Exotics_Summary/ATLAS_Exotics_Summary.pdf.

[15] Caroline Collard (on behalf of the CMS Collaboration), *Searches for third generation squarks with CMS*, arXiv:1709.00868 (hep-ex) (2017).

[16] ATLAS Collaboration, *Measurement of the W-boson mass in pp collisions at* $\sqrt{s}$*=7 TeV with the ATLAS detector*, arXiv:1701.07240 (hep-ex) (2015).

[17] ALICE Collaboration, *J/*ψ *suppression at forward rapidity in Pb-Pb collisions at* $\sqrt{s_{NN}}$ *= 5.02 TeV*, arXiv:1606.08197 (nucl-ex) (2016).

[18] LHCb collaboration, *Measurement of the* $B_s^0 \to \mu^+ \mu^-$ *branching fraction and search for* $B^0 \to \mu^+ \mu^-$ *decays at the LHCb experiment*, arXiv:1307.5024 (hep-ex) (2013).

[19] LHCb collaboration, *Observation of J/*ψp *resonances consistent with pentaquark states in* $\Lambda_b^0 \to J/\psi K^- p$ *decays*, arXiv:1507.03414 (hep-ex) (2013).

[20] http://public.web.cern.ch/public/en/research/AccelComplex-en.html.

[21] M. Titov, *International Linear Collider Reference Design Report Volume 2: PHYSICS AT THE ILC*, arXiv:0709.1893v1 (hep-ph) (2007).

[22] http://lhcb-public.web.cern.ch/lhcb-public/.

[23] LHCb collaboration, R. Aaij et al., *Amplitude analysis of* $B^+ \to J/\psi\phi\ K^+$ *decays*, arXiv:1606.07898v1 (hep-ex) (2016).

[24] https://home.cern/about/physics/.

[25] http://www.linearcollider.org.

[26] http://www.worldscientific.com/doi/suppl/10.1142/6647/suppl_file/6647_chap01.pdf.

[27] F. Sauli, *GEM: A new concept for electron amplification in gas detectors*, Nuclear Instruments and Methods A **386** (1997) 531.

[28] E. Rutherford, H. Geiger, *An electrical method of counting the number of Îś particles from radioactive substances*, Proceedings of the Royal Society (London), Series A **81** no.546 (1908) 141-161.

[29] http://www.talkmag.in/cms/news/science-tech/.

[30] G. Charpak, R. Bouclier, T. Bressani, J. Favier, and C. Zupancic, *The use of Multiwire Proportional Counters to select and localize charged particles*, Nuclear Instruments and Methods, **62** (1968) 262.

[31] D. R. Nygren and J. N. Marx, *The Time Projection Chamber*, Physics Today **31N10** (1978) 46.

[32] V. V. Parkhomchuck, N. Pestov Yu, N. V. Petrovykh, *A spark counter with large area*, Nuclear Instruments and Methods, **93** (1971) 269-270.

[33] R. Santonico, R. Cardarelli, *Development of resistive plate counters*, Nuclear Instruments and Methods, **187** (1981) 377-380.

[34] A. Sharma, *Properties of some gas mixtures used in tracking detectors*, http://geant4.cern.ch/support/ReleaseNotes4.9.4.html.

[35] P. Fonte, V. Peskov, *On the physics and technology of gaseous particle detectors*, arXiv:0909.2681 (physics.ins-det) (2009).

[36] M. Fransen, *Gridpix: TPC development on the right track. The development and characterisation of a TPC with a CMOS pixel chip read out*, Ph.D. Thesis, University of Amsterdam (2012).

[37] M.A. Chefdeville, newblock *Development of Micromegas-like gaseous detectors using a pixel readout chip as collecting anode*, Ph.D. Thesis, University of Amsterdam (2009).

[38] http://pdg.lbl.gov.

[39] F. Zappon, *It is about time. Design and test of a per-pixel high-resolution TDC*, Ph.D. Thesis, University of Amsterdam (2015).

[40] W.W.M. Allison, C.B. Brooks, J.N. Bunch, R.W. Pleming, and R.K. Yamamoto, *Review of particle physics, Passage of particles through matter*, Chapter 27, (2010), 285-299.

[41] S.S. Sahoo, P. Bhattacharya, S. Biswas, and B. Mohanty, *A numerical study on gaseous detectors for high energy physics*, Nucl. Physics [60] (2015).

[42] http://www-flc.desy.de/tpc/basicsgem.php.

[43] A. Sharma, *Muon tracking and triggering with gaseous detectors and some applications*, Nuclear Instruments and Methods in Physics Reasearch Section A **666** (2012) 98-129.

[44] http://geant4.cern.ch/support/ReleaseNotes4.9.3.html.

[45] http://geant4.cern.ch/support/ReleaseNotes4.9.4.html.

[46] Particle Data Group, *The ionisation loss of relativistic charged particles in thin gas samples and its use for particle identification II. Experimental results*, Nuclear Instruments and Methods **133** (1976) 325-334.

[47] P. Langevin, *On the Theory of Brownian Motion*, C. R. Acad. Sci. (Paris) **146** (1908) 530.

[48] D.S. Lemons, A. Gythiel, *On the Theory of Brownian Motion*, Am. J. Phys. **65 no 11** (1997) 1079.

[49] N. Colonna, The n_TOF Collaboration, *Neutron cross-section measurements at the n_TOF facility at CERN*, Nuclear Instruments and Methods in Physics Research Section B **213** (2004) 49-54.

[50] F. Sauli, *Principles of Operation of Multiwire Proportional and Drift Chambers*, FERBEL, T.: EXPERIMENTAL TECHNIQUES IN HIGH ENERGY PHYSICS*, 79-188 AND CERN GENEVA - CERN 77-09 (77,REC.JUL.) 92p.

[51] M. Titov, *New Developments and Future Perspectives of Gaseous Detectors*, arXiv:0706.3516v1 (physics.ins-det) (2007).

[52] E.N. Koffeman, *Gossip: Gaseous pixels*, Nuclear Instruments and Methods **582** (2007) 858-860.

[53] http://geant4.web.cern.ch/geant4/reports/gallery/electromagnetic/edep/summary.html.

[54] http://vlado.fmf.uni-lj.si/texceh/kako/tex2pdf/ex/maria-1.pdf.

[55] http://www.cbooth.staff.shef.ac.uk/phy6040det/eloss2.pdf.

[56] J.E. Moyal, *Theory of ionization fluctuations*, Phil. Mag. **46** (1955) 263.

[57] L. Landau, The n_TOF Collaboration, *On the energy loss of fast particles by ionization*, J. Phys. (USSR) **8** (1994) 201-205.

[58] I. Lehraus, R. Matthewson, W. Tejessy, and M. Aderholz, *Performance of a large scale multilayer ionization detector and its use for measurements of the relativistic rise in the momentum range of* $20-110$ *GeV/c*, Nuclear Instruments and Methods **153** (1978) 347-355.

[59] M. Capeans *Radiation Hardness of Gaseous Detectors. Gaseous Detectors*, Fourth MC-PAD Network Training Event (2011) 325-334.

[60] L. Urban, *A multiple scattering model in Geant4*, *Preprint* CERN-OPEN-2006-077.

[61] http://pdg.lbl.gov/2005/reviews/passagerpp.pdf.

[62] Laszlo Urban, *Private communication.*

[63] J. Sempau, J. M. Fernandez-Varea, E. Acosta, and F. Salvat, *Experimental benchmarks of the Monte Carlo code PENELOPE*, Nuclear Instruments and Methods in Physics Research B **207** (2003) 107-123.

[64] J. Apostolakis, S. Giani, L. Urban, M. Maire, A. V. Bagulya, and V. M. Grichine, *An implementation of ionisation energy loss in very thin absorbers for the GEANT4 simulation package*, Nuclear Instruments and Methods in Physics Research A **453** (2000) 597-605.

[65] I. B. Smirnov, *Modeling of ionization produced by fast charged particles in gases*, Nuclear Instruments and Methods in Physics Research A **554** (2005) 474-493.

[66] The Geant4 collaboration, *Physics Reference Manual*, (2010).

[67] P. V. Vavilov, *Ionisation losses of high energy heavy particles*, Soviet Physics JETP **5** (1958) 749-751.

[68] A. Schälicke, A. Bagulya, O. Dale, F. Dupertuis, V. Ivanchenko, and O. Kadri, A. Lechner, M. Maire, M. Tsagri, and L. Urban, *Geant4 electromagnetic physics for the LHC and other HEP applications*, Journal of Physics: Conference Series **331** (2011) Series 032029.

[69] Y. Giomataris, Ph. Rebourgeard, J. P. Robert, and G. Charpak, *MICROMEGAS: a high-granularity position-sensitive gaseous detector for high particle-flux enviroments*, Nuclear Instruments and Methods in Physics Research A **376** (1996) 29-35.

[70] http://en.wikipedia.org/wiki/MicroMegas_detector.

[71] http://na48.web.cern.ch/NA48/Welcome.html.

[72] G. Charpak, J. Derre, Y. Giomataris, and Ph. Rebourgeard, *Micromegas, a multipurpose gaseous detector*, Nuclear Instruments and Methods in Physics Research A **478** (2002) 26-36.

[73] P. Abbon, *et al.*, *Micromegas for Axion Search and Prospects*, Journal of Physics: Conference Series, **65** (2007).

[74] E. Ferrer Ribas, *et al.*, *A new Micromegas line for the CAST experiment*, Contribution to the 2007 Vienna Instrumentation conference.

[75] J. Chadwick, *The Existence of a Neutron*, Proceedings of the Royal Society A **136** (1932) 692-708.

[76] K. Amako, *et al.*, Proceedings of CHEP94, San Francisco, CA, USA, LBL-35822 CONF-940492 (1993).

[77] D. Green, *AT THE LEADING EDGE, The ATLAS and CMS LHC Experiments*, World Scientific Publishing Co. Pte. Ltd., 2010.

[78] http://hep.tsinghua.edu.cn/~yangzw/CourseDataAna/Geant4UserDocuments/4.9.5/G4.9.5_PhysicsReferenceManual.pdf.

[79] B. Andersson, G. Gustafson, and B. Nielsson-Almqvist, *A model for low-pT hadronic reactions with generalizations to hadron-nucleus and nucleus-nucleus collisions*, Nuclear Physics B **281** (1987) 289.

[80] A. Heikkinen, *Bertini intra-nuclear cascade implementation in Geant4*, Computing in High Energy and Nuclear Physics (2003).

[81] http://geant4.cern.ch/support/proc_mod_catalog/models/hadronic/BinaryCascade.html.

[82] P. V. Degtyarenko, M. V. Kossov, and H. P. Wellisch, *Chiral invariant phase space event generator, I. Nucleon-antinucleon annihilation at rest*, The European Physical Journal A **8** (2000) 217-222.

[83] http://www.oecd-nea.org/janis/.

[84] https://www.nndc.bnl.gov/csewg/.

[85] https://www.oecd-nea.org/nea/mcdb.html.

[86] wwwndc.jaea.go.jp/jendl/jendl.html.

[87] David Brown, *Private communication.*

[88] M. B. Chadwick, *et al.*, *ENDF/B-VII.0: Next Generation Evaluated Nuclear Data Library for Nuclear Science and Technology*, Nuclear Data Sheets **107** (2006) 2931-3060.

[89] V. McLane and Members of the Cross Section Evaluation Working Group, *ENDF-201, ENDF/B-VI summary documentation supplement 1, ENDF/HE-VI summary documentation*, (1996).

[90] NEA, OECD, *The JEF-2.2 Nuclear Dara Library*, (2000).

[91] NEA, OECD, *The JEFF-3.0 Nuclear Dara Library*, (2005).

[92] J. Ch. Sublet, A. J. Koning, R. A. Forrest and J. Kopecky, *The JEFF-3.0/A Neutron Activation File-New Features, Validation, and Usage*, Proceedings of the international conference on nuclear data for science and technology **769** (2005) 203.

[93] NEA, OECD, *The JEFF-3.1 Nuclear Dara Library*, (2006).

[94] K. Shibata, *et al.*, *Japanese Evaluated Nuclear Data Library Version 3 Revision-3: JENDL-3.3*, Journal of Nuclear Science and Technology **39** (2002) 1125-1136.

[95] M. B. Chadwick, P. Obložinský, M. Herman, *et al.*, *ENDF/B-VII.0: Next Generation Evaluated Nuclear Data Library for Nuclear Science and Technology*, Nuclear Data Sheets **107** (2006) 2931-3060.

[96] A. Howard, G. Folger, J. M. Quesada, and V. Ivanchenko, *Validation of neutrons in Geant4 using TARC data - production, interaction and transportation*, Nuclear Science Symposium Conference Record, NSS '08. IEEE (2008) 2885-2889.

[97] http://geant4.web.cern.ch/geant4/UserDocumentation/UsersGuides/PhysicsReferenceManual/BackupVersions/V9.4/fo/PhysicsReferenceManual.pdf.

[98] http://geant4.cern.ch/G4UsersDocuments/UsersGuides/ForApplicationDeveloper/print/applDeveloperMerged.html.

[99] http://www.fluka.org/content/manuals/FM.pdf.

[100] http://mpgd.web.cern.ch/mpgd/documents/RD51%20proposal.pdf.

[101] W. W. M. Allison, C. B. Brooks, J. N. Bunch, R. W. Pleming, R. K. Yamamoto, *The ionization loss of relativistic charged particles in thin gas samples and its use for particle identification*, Nuclear Instruments and Methods **133** (1976) 325-334.

[102] M. Chefdeville, *et al.*, *An electron-multiplying Micromegas grid made in silicon wafer post-processing technology*, Nuclear Instruments and Methods **566** (2006) 490-494.

[103] http://mc-pad.web.cern.ch/mc-pad/DutchReport_Tsagri.pdf.

[104] http://fas.org/sgp/othergov/doe/lanl/lib-www/la-pubs/00326407.pdf.

[105] http://nuclearpowertraining.tpub.com/h1019v1/css/Radiative-Capture-70.htm.

[106] http://geant4.cern.ch/support/ReleaseNotes4.9.5.html.

[107] http://mathematicsandcomputation.cowhosting.net/MonteCarlo05/FullPapers/usr-ghad-6-paper.pdf.

[108] https://geant4.web.cern.ch/geant4/support/proc_mod_catalog/models/hadronic/BinaryCascade.html.

[109] J. Jakubek, *Detection of single electrons by means of a Micromegas-covered MediPix2 pixel CMOS readout circuit.*, Nuclear Instruments and Methods in Physics Research Section A **540** (2005) 295-304.

[110] Y. Giomataris, Ph. Rebourgeard, J. P. Robert, and G. Charpak, *MICROMEGAS: a high-granularity position-sensitive gaseous detector for high particle-flux enviroments*, Nuclear Instruments and Methods in Physics Research A **376** (1996) 29-35.

[111] M. Chefdeville, P. Colas, Y. Giomataris, H. van der Graaf, E. H. M. Heijne, S. van der Putten, C. Salm, J. Schmitz, S. Smits, J. Timmermans, and J. L. Visschers, *An electron-multiplying "Micromegas" grid made in silicon wafer post-processing technology*, Nuclear Instruments and Methods in Physics Research A **556** (2006) 490-494.

[112] F. Hartjes, *A diffraction limited nitrogen laser for detector calibration in high energy physics.*

[113] X. Llopart, *Timepix, a pixel readout chip for arrival time measurements in a TPC*, Presentation slides at FEE2006 Perugia (2006).

[114] X. Llopart, R. Ballabriga, M. Campbell, L. Tlustos W. Wong, *Principles of Operation of Multiwire Proportional and Drift Chambers*, Nuclear Instruments and Methods in Physics Research A **581** (2007) 485-494.

[115] H. van der Graaf, *New developments in gaseous tracking and imaging detectors.*, Nuclear Instruments and Methods in Physics Research A **607** (2009) 78-80.

[116] http://aladdin.utef.cvut.cz/ofat/others/Pixelman/index.html.

[117] X. Llopart et al., *Medipix2: a 64k Pixel Readout Chip With 55um Square Elements Working in Single Photon Counting Mode.*, IEEE Trans. Nucl. Science **49** (2002).

[118] X. Llopart Cudie, C. Frojdh and M. Campbell, *Desing and Characterization of 64k Pixel Chips Working in Single Photon Processing Mode.*, Ph.D. Thesis, Mid Sweden Univ., Sundsvall (2007). Presented on 25 May 2007.

[119] T. Holy, S. Pospisil, J. Uher, Z. Vykydal, J. Jakubek, and A. Cejnarova, *Pixel detectors for imaging with heavy charged particles.*, Nuclear Instruments and Methods in Physics Research Section A **591** (2008) 155-158.

[120] Y. Bilevzch et al., *The performance of GridPix detectors.*, https://www.deepdyve.com/lp/institute-of-electrical-and-electronics-engineers/the-performance-of-gridpix-detectors-PQaziEg0vw

[121] K. Akiba, K. Artuso, M. Badman, et al., *Charged particle tracking with the Timepix ASIC.*, Nuclear Instruments and Methods in Physics Research Section A **661** (2012) 31-49.

[122] J. Jakubek et al., *Precise energy calibration of pixel detector working in time-over threshold mode.*, Nuclear Instruments and Methods Section A **633** (2011) S262-S266.

[123] https://twiki.cern.ch/twiki/bin/viewauth/CAE/AnsysService

SUMMARY

By analyzing and simulating the collisions at the Large Hadron Collider (LHC) particle physicists are trying to verify, understand and expand the Standard Model of particle physics. The LHC and future experiments will require excellent detector performance as well as accurate Monte Carlo simulation tools. Throughout this work we analyzed both detector and Monte Carlo tools' performance and we provide suggestions on how to improve both. We have focused on typical gases used in gas detectors in HEP experiments, and in particular in LHC experiments. The number of candidate gas mixtures and gas concentrations that one can create and test can be large. However, properties such as inflammability, cost, aging, neutron capture and toxicity restrict the use of many gas mixtures. The results of this study were used for the choice of the ingredients in a gas mixture for the Gossip detector (studied in Chapter 5). None of the gas mixtures presented in this work stands out as an exclusive candidate for use in the Gossip detector. Among the various reasons for this are the required operational stability to avoid sparks, the high drift velocity and the low diffusion. Nevertheless, an Argon/CO_2 mixture satisfies most of these prerequisites. Moreover, argon-based mixtures provide more accurate particle identification and better spatial resolution compared to the other gas mixtures becoming thus a good candidate for Gossip.

We have investigated the ionization energy loss of minimum ionizing particles in thin gas layers simulated by the Geant4 code. We provided a detailed validation by examining dependence on the electron incident energy, the material of the detector, the thickness of the material, the various physics processes and the fluctuation model included in the Geant4 code. We have identified some unexpected behavior that could be traced to the fluctuation model implemented by the Geant4 code and can be considered as an inaccuracy of Geant4. It is worth noticing here that this correction to the fluctuation model may have a significant impact for simulations also in LHC experiments including their high energy showers, since the corrected Geant4 release might imply improvements which could be relevant in certain cases. The Geant4 fluctuation model which reproduces the ionization energy loss for charged particles in thin layers was improved in order to become

properly applicable also to very thin layers or low density materials. This revised model is also less dependent on step limitations, e.g. range cut-offs for the production of secondary particles. The updated fluctuation model is recommended for detector simulations, especially for thin targets or thin surface gas detectors where the minimum energy deposition is of interest. Further precise measurements of the ionization energy loss of MIPs (Landau distribution) in thin gaseous detectors are recommended.

Furthermore, this work includes a study of the neutron simulation in the Geant4 code. We have reviewed and compared the behavior of neutron cross-sections in Geant4 for key chamber gases with measured neutron cross-sections including older and recent data sets. This work, help the Geant4 group to update the nuclear data in the tool improving its performance and reliability. Keeping in mind the many disciplines which use Geant4, with a plethora of applications, an update was necessary. Given the availability of new and more accurate data, we suggested the update of Geant4 with improved evaluated neutron data from a newer evaluated data library for most of the chemical constituents.

The Micromegas detector

The electron transmission from the Micromegas μ-mesh layer all the way to the cathode includes also the charge amplification occurring during this last step of the initially produced ionization charges in the conversion volume. In these measurements the electrons were produced near the μ-mesh by photo-ionization, using a UV-light source. Applying a few combinations of voltages to the three different layers of the Micromegas detector, i.e. the cathode, the μ-mesh and the anode, we could measure the transmission of electrons with few eV kinetic energy. The so derived experimental values of the electron transmission have been compared with the simulated values obtained with the Ansys and Garfield++ codes. The agreement between simulation and measurement is satisfactory. This is certainly an experimental validation of the simulation codes used throughout this work. In addition, these measurements provide more insight in the actual processes occurring during this last step of signal creation in a Micromegas detector. This very last amplification of the initial ionization occurs in a region whose configuration distinguishes Micromegas from all the other detectors used in particle physics.

Gossip detector

The Gossip detector has been designed to operate with a small drift gap ($\sim$1 mm). We have predicted the performance of the Gossip design and made suggestions in order to improve it. The simulation work is validated with a set of laser measurements. The Gossip performance is a result of many parameters such as the pixel size, the drift gap, the avalanche gap, the gas mixture, the gas gain, the drift field and the signal shaping time. Our results show that the gas gain depends on the gap size and tends to be high for the lowest avalanche gap size. Future studies accompanying this Ph.D. thesis include studies for other gas mixtures, different avalanche gap sizes and InGrid hole diameters.

SAMENVATTING

Door het analyseren en simuleren van botsingen in de Large Hadron Collider (LHC), proberen deeltjesfysici het Standaard Model van de deeltjesfysica te doorgronden, te verifiëren en uit te breiden. De LHC en toekomstige experimenten hebben precieze detectoren en accurate Monte Carlo simulatie-tools hard nodig. In dit onderzoek beschouwen we zowel de prestaties van de detector als van de Monte Carlo tools en bieden we suggesties hoe beide te verbeteren. We hebben ons gericht op typische gassen gebruikt in gasdetectoren voor HEP experimenten, en in het bijzonder voor LHC experimenten. Het aantal kandidaat-gasmengsels en gasconcentraties dat men kan maken en testen kan behoorlijk groot zijn. Echter eigenschappen zoals ontvlambaarheid, kosten, veroudering, neutronenvangst en toxiciteit beperken de keuze van deze gasmengsels. De resultaten van deze studie werden gebruikt om de samenstelling van een geschikt gasmengsel voor de Gossip detector te bepalen. Geen van de gasmengsels zoals in dit onderzoek gepresenteerd springt er uit als perfecte toepassing voor de Gossip detector. Redenen hiervoor zijn de eisen met betrekking tot de operationele stabiliteit (vonken), de hoge drift snelheid en lage diffusie. Echter Argon/CO_2 mengsels voldoen in de meeste gevallen aan deze voorwaarden. Bovendien bieden mengsels gebaseerd op Argon een nauwkeurige identificatie van deeltjes en een betere positie resolutie in vergelijking tot de andere gasmengsels, en zijn derhalve een goede kandidaat voor Gossip.

We onderzochten minimaal ioniserende deeltjes in dunne gaslagen zoals gesimuleerd door de Geant4 code. We hebben details bestudeerd in de afhankelijkheid van energie van de elektronen, het materiaal van de detector, de materiaaldikte, verschillende natuurkundige processen en het fluctuatiemodel zoals opgenomen in de Geant4 code. De verschillende controles uitgevoerd tijdens dit onderzoek hebben onverwachte afwijking herleid tot het fluctuatie model zoals onderdeel van de Geant4 code. Opgemerkt wordt dat de correctie van het fluctuatiemodel significante impact kan hebben op LHC experimenten, inclusief de high energy showers. De gecorrigeerde Geant4 uitkomsten kunnen dan relevante verbeteringen bewerkstelligen. Het Geant4 fluctuatiemodel, dat de ionisatie van geladen deeltjes

in dunne gaslagen beschrijft, kon verbeterd worden zodat het goed toepasbaar is op zeer dunne lagen en materialen met lage dichtheid. Dit aangepaste model is ook minder afhankelijk van stapbegrenzingen, bijv. range cut-offs voor de productie van secondaire deeltjes. Het aangepaste model zou gebruikt moeten worden voor simulatie van detectoren, speciaal voor dunne doelen of dunne oppervlakte gasdetectoren waar een kleine energie opname van belang is.

Dit onderzoek bevat tevens een studie van de neutronensimulatie in de Geant4 code. We hebben het gedrag van neutron werkzame doorsnedes voor belangrijke gassen in Geant4 vergeleken met metingen, inclusief wat oudere en recente data sets. Dit onderzoek helpt Geant4 om de nucleaire data bij te werken, waardoor de prestaties en betrouwbaarheid verbeterd worden. Deze update is vereist, omdat vele disciplines Geant4 gebruiken, met een breed scala aan toepassingen. Nu nieuwe en nauwkeurigere gegevens beschikbaar zijn, wordt aanbevolen Geant4 aan te passen door verbeterde en geëvalueerde neutronen gegevens op te nemen van een nieuwere geëvalueerde data library voor de meeste chemische bestanddelen.

The Micromegas detector

De elektronentransmissie van de Micromegas μ-mesh laag helemaal naar de kathode, bevat ook de amplificatie van de lading zoals plaatsvindt tijdens deze laatste stap van de initieel geproduceerde ladingen in het conversie volume. Bij deze metingen werden de elektronen geproduceerd nabij de μ-mesh laag door middel van foto-ionisatie, gebruik makend van een UV-lichtbron. Door een aantal verschillende voltages aan te brengen op de drie lagen van de Micromegas detector, te weten op de kathode, de μ-mesh en de anode, konden we de transmissie meten van elektronen met weinig kinetische energie. De aldus verkregen experimentele waarden van de elektronentransmissie zijn vergeleken met de gesimuleerde waarden verkregen met Ansys en Garfield++ codes. De gemeten en gesimuleerde waarden komen voldoende overeen. Dit is zeker een experimentele validatie van de simulatie codes zoals in dit onderzoek gebruikt. Bovendien geven deze metingen meer inzicht in de werkelijke processen die optreden tijdens de laatste stap van het creëren van het signaal in een Micromegas detector. Deze laatste versterking van de initiële ladingen treedt op in een gebied waar de configuratie van de Micromegas zich onderscheidt van alle andere detectoren gebruikt in de deeltjesfysica.

Gossip detector

Een GridPix detector is een gasvormige detector die in staat is individuele primaire elektronen te detecteren. Het is een samenstelling van een Timepix pixel chip als actieve anode, bedekt met een dunne laag Silicium Rich Nitride (SiRN) als bescherming tegen ontladingen, een geïntegreerd amplificatie grid (InGrid) aangebracht boven op de chip door post processing technieken, een drift volume en tenslotte een kathode oppervlak. Het drift gebied bevindt zich dus tussen het grid en de kathode, terwijl de versterking plaatsvindt tussen de chip en het grid. De Gossip detector is ontworpen om te functioneren met een kleine drift afstand

(∼1 mm). We hebben de werking van het Gossip ontwerp voorspeld, en suggesties ter verbetering aangereikt. De simulaties zijn gevalideerd met een set laser metingen. Het werkpunt van de Gossip is een combinatie van vele parameters, zoals de pixelgrootte, de drift en grid afstand, het gasmengsel, het driftveld en tijd ont-wikkeld van het signaal. Onze resultaten tonen dat de versterking afhankelijk is van de afstand. Aanbevolen wordt dat toekomstige studies , aansluitend op dit proefschrift, zich richten op andere gasmengsels, verschillende geometrien en InGrid gat diameters.

ACKNOWLEDGEMENTS

It was a pleasure and honor doing my Ph.D. with the University of Amsterdam. First of all, I would like to thank my promotor Els Koffeman who came up during the first Marie-Curie kick-off meeting at CERN with the Ph.D. opportunity which opened the UvA's and Nikhef's doors to me. I would also like to thank my promotor Stan Bentvelsen for stepping in when needed. As co-promotor I was lucky to have Nigel Hessey, whose scientific guidance and English corrections were of high importance. A thank you also goes to my C3 supervisor Sijbrand de Jong who was there when needed.

This thesis is a group effort and I would like to thank all my Ph.D. committee and everyone at Nikhef who made this thesis possible. Thanks to all members of the RD group for being supportive. In particular, thank you Fred Hartjes for your laser setup. Thank you Martin van Beuzekom for all your help and tips during the last months. A thank you to CERN and Seamus Hegarty for the opportunity given during the Marie Curie Actions and the 7th Framework Programme's Initial Training Network. A big thanks goes also to the software group of Geant4 and in particular to John Apostolakis and Gunter Folger for their help with Geant4.

A thank you goes to all my friends who helped me through this journey one way or another. A special thank you to Andrew whose constant support was the best companion during my odyssey in Amsterdam. Finally, I want to dedicate this thesis to my parents Thanasis and Soula, as well as my brother Yannis. Without them this accomplishment would not have been made possible.